Spring 1-1-2011

Advanced Lithium Ion Battery Materials Prepared with Atomic Layer Deposition

Andrew S. Cavanagh
University of Colorado at Boulder, ascavanagh@gmail.com

Advanced Lithium Ion Battery Materials Prepared with Atomic Layer Deposition

by

Andrew S. Cavanagh

B.S., Fort Lewis College, 2003

M.S., University of Colorado, 2010

A thesis submitted to the

Faculty of the Graduate School of the

University of Colorado in partial fulfillment

of the requirements for the degree of

Doctor of Philosophy

Department of Physics

2011

This thesis entitled:
Advanced Lithium Ion Battery Materials Prepared with Atomic Layer Deposition
written by Andrew S. Cavanagh
has been approved for the Department of Physics

Prof. Steven M. George

Prof. Daniel S. Dessau

Date

The final copy of this thesis has been examined by the signatories, and we find that both the content and the form meet acceptable presentation standards of scholarly work in the above mentioned discipline.

Cavanagh, Andrew S. (Ph.D., Physics)

Advanced Lithium Ion Battery Materials Prepared with Atomic Layer Deposition

Thesis directed by Prof. Steven M. George

As the world consumes the dwindling supply of fossil fuels, an alternative to gasoline powered vehicles will become necessary. Lithium ion batteries (LIBs) are emerging as the dominant power source for portable electronics, and are seen as a promising energy source in the development of electric vehicles. Current LIB technology is not well suited for vehicles, increases in the energy density, power density and durability are needed before LIB are ready for widespread use in electric vehicles.

$LiCoO_2$ and graphite are the dominant cathode and anode active materials, respectively in LIBs. On the cathode side, instabilities in $LiCoO_2$ can lead to the deterioration of the LIB. Decomposition of electrolyte on the graphite anode surface to form a solid-electrolyte interphase (SEI) consumes lithium from the cathode resulting in a lower battery capacity. Instabilities in the in the SEI can result in catastrophic battery failure. Previous studies have employed metal oxides films, typically grown with wet chemical techniques, to stabilize $LiCoO_2$ and mitigate the formation of the SEI on graphite. The thicknesses of films grown with wet chemical techniques was typically ~50-1000 Å. In order to achieve higher power densities, the particle size of LIB active materials is being scaled down. As active materials get smaller the mass contribution of a protective film can become a significant fraction of the total mass.

Atomic layer deposition (ALD) has been used to grow ultra thin films of Al_2O_3 on $LiCoO_2$ and graphite. By altering the interaction between the active material and the battery electrolyte it was possible to improve the stability of both $LiCoO_2$ and graphite electrodes in LIBs. In the case of graphite, the Al_2O_3 film may be thought of as an artificial SEI.

During the initial charge-discharge cycle of a LIB, the electrolyte decomposes on the anode to form the SEI. The formation of the SEI is believed to prevent further decomposition of the

electrolyte on the anode surface. The SEI contains electrolyte decomposition products including Li_2CO_3, Li_2O, LiOH, LiF and R-OLi. In order to grow a truly artificial SEI on the graphite anode, *i.e.* grow a film that mimics the SEI that forms during charge-discharge cycling, new ALD chemistries for the growth of Li_2CO_3 and LiOH have been developed. The ALD of an artificial SEI layer may limit lithium loss and improve the capacity stability during charge-discharge cycles.

Dedication

To my family, past, present, and future. I would not be who I am today without you.

Acknowledgements

First I would like to acknowledge my PhD. thesis advisor Prof. Steven George, who has provided me with the opportunity, environment, and resources to be as creative as I could be in the laboratory. Prof. George has been an supportive mentor throughout my graduate career, thank you.

The George group has been a great team to work with, every member of the group has always been willing to take time to act as a sounding board for my ideas, help me solve a problem, help me diagnosis a problem or share their perspective. I acknowledge all of the George group members I have encountered during my graduate career. Jarod McCormick deserves a special thanks for being my graduate student mentor when I started in the lab. Arrelaine Dameron, Beau Burton, David Goldstein, Dragos Seghete, Jacob Bertrand, Layton Baker and Virginia Anderson have been an invaluable resource in helping me develop my ideas. Thanks to Byunghoon Yoon and Younghee Lee who helped with the work presented in Chapter 4. Thanks to Christopher Wilson who helped with the work presented in Chapter 7. Thank you to the remainder of the George group, Aziz Abdulagatov, Byoung Hoon Lee, Guillermo Acosta, Ming Xie, Rickard Wind, Robert Hall, Ryan Fitzpatrick, Shaibal Sarkar, Shih-Hui Jen, Xiaohua Du, Yijun Du and Zachary Sechrist. I have appreciated all of your help.

Much of the work presented in this thesis would not be possible without our collaborations with Se-hee Lee's research group in the Department of Mechanical Engineering at the University of Colorado and the National Renewable Energy Laboratory. Thanks to Yoon Seok Jung, Leah Riley, Anne Dillon and Sun-Ho Kang who helped with the work presented in Chapters 5 and 6. Thanks

to Isaac Scott, James Trevey and Chunmei Ban for their valuable discussions.

Thanks to Tom Giddings and Paul Rice for their help in using the TEM and SEM respectively.

Many of the instruments used in this research would not be as well designed or as well made had it not be for the staff at the CIRES machine shop. Thanks to Craig Joy, Don David, Ken Smith, Jim Kastengren, Dennis Steffey and Wayne Winkler.

None of this research would have been possible without the administrative support that it takes to keep a department running. Thanks to Lynn Sarkis, Nathan Campbell, Mark Stewart, Cheryl Graham, Violet Lehman, Becky Thirlaway, Jeanne Nijhowne and Cori Fagan-Edminster.

Contents

Chapter

Tables

Table

Figures

Figure

Chapter 1

Introduction

The world runs on nonrenewable fossil fuels [3]. Figure 1.1 show that 81.3% of the worlds total primary energy supply comes from oil, gas and coal [3]. Renewable energy sources such as geothermal, solar and wind power account for 0.7% of the worlds total primary energy supply. At the current production rates it has been estimated that the worlds supply of oil, gas and coal will be exhausted in 40, 62 and 224 years respectively [72]. As oil disappears it will be possible to shift non mobile users of oil, such as residential heating, to other established technologies. As of 2008, 61.4% of the oil produced was used for transportation [3]. Vehicles do not have an alternative established technology to replace oil.

Running the world on renewable energy sources has one major problem, energy storage. The problem of energy storage stems from two issues. The first issue is portability. In order to replace oil in vehicle applications, energy generated from renewable sources must be stored in such a way that it can safely and efficiently power a vehicle. The second issue is demand. Most renewable energy sources, such as wind power or solar, have their production rate fixed by nature. With wind power and solar, peak production does not necessarily correlate with peak demand. Rather, peak production correlates with windiest or sunniest times of the day. In order to synchronize peak power production from renewable energy sources with peak demand from the population being served an efficient and durable means of energy storage must be developed.

One proposed solution to the energy storage problem is to use a nations battery powered fleet of electric vehicles as a collective energy storage system [101]. When a vehicle is plugged

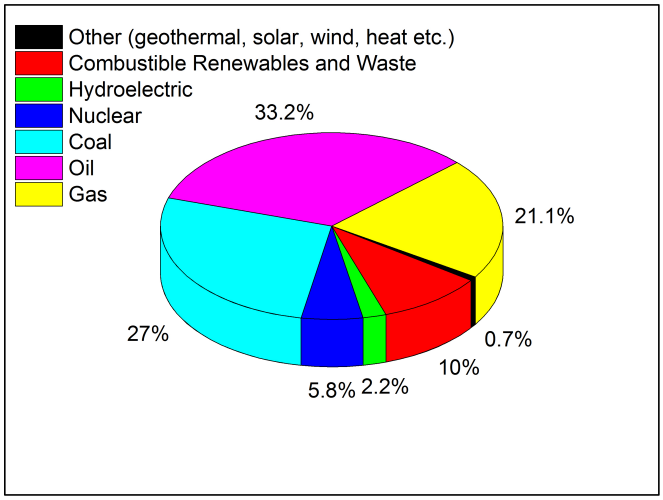

Figure 1.1: World total energy supply by fuel [3].

into the grid it can either be charging or supplying energy depending on consumer demand and the amount of power being generated by renewable energy sources [101]. For batteries to be commercially viable, both for grid storage and electric vehicles, they must have a high energy and power density and be safe and durable [101]. Currently, lithium ion batteries (LIBs) are the most established battery technology for electric vehicles [153, 30]. Due to the low specific energy density and long recharge times, electric vehicles based current LIB technology are limited to small, low daily mileage vehicles [195]. LIBs can be improved by coating the active material with thin films [129, 40]. Significant enhancements are needed to bring LIBs up to the target levels required for practical use and commercial viability.

1.1 Statement of Purpose

This dissertation is concerned with the modification of surfaces of LIB active materials to enhance the performance of the material in a battery cell. The surface modifications were made by growing thin films with atomic layer deposition (ALD). Chapter 2 is an overview of thin film deposition techniques. Chapter 3 is a review of the mechanism by which thin films can enhance a LIB. Chapters 5 and 6 demonstrate that thin films of Al_2O_3 grown with ALD can dramatically enhance the performance of cathode ($LiCoO_2$)[98] and anode (graphite)[99] materials. Chapter 4 details the development of new ALD chemistries specifically designed to mimic films that grow from the electrochemical decomposition of electrolytes in a LIB [36]. Chapter 7 details ALD on carbon nanotubes (CNTs) [35]. CNTs may serve as conductive scaffolding onto which a LIB active material may be grown with ALD in the future.

Chapter 2

Thin Films

Many technologies rely on thin films of various dimensions and roughnesses [170]. Thin films have a variety of applications and accordingly a variety of deposition techniques. Some common applications of thin films include: semiconductors and dielectrics for microelectronics and energy conversion devices, diffusion barriers for protection against corrosion and oxidation, catalysis, protective layers for lithium ion batteries, and various optical applications.

There are several techniques for depositing thin films. These techniques fall into two classes: chemical deposition and physical deposition [170]. Chemical deposition techniques include wet chemical methods like sol-gel and electroplating as well gas phase methods like chemical vapor deposition (CVD) and atomic layer deposition (ALD). Physical deposition methods employ a variety of techniques to vaporize a material and condense it onto a substrate. This is commonly referred to as physical vapor deposition (PVD).

The various methods to grow thin films produce varying degrees of conformality and step coverage. Step coverage is the ability of a film to grow at the same rate on the face of a step as on the top surface of the step. Figure 2.1(a) shows poor step coverage and Figure 2.1(b) shows good step coverage. Conformality requires good step coverage and that the film be uniform on all surfaces. Figure 2.1(c) shows poor conformality and Figure 2.1(d) shows a conformal film.

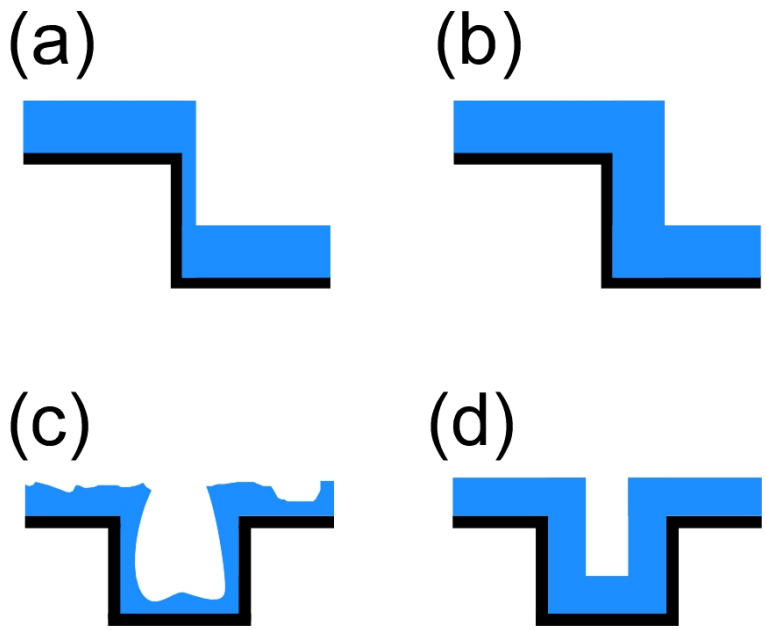

Figure 2.1: Varying degrees of conformality, (a) poor step coverage, (b) good step coverage, (c) poor conformality and (d) a conformal film. Adapted from [4].

2.1 Physical vapor deposition

PVD is a thin film deposition technique where physical rather them chemical methods are use to grow the film [170]. PVD includes a variety of methods to vaporize metals which are condensed on the substrate to grow a film. The vaporization methods include heating the metal with a filament, electron beam or laser, or employing a plasma to sputter a metal target. PVD can be employed in the presence of another gas phase precursors such as oxygen or nitrogen to grow metal oxides or nitride respectively.

PVD has limitations in its ability to uniformly deposit films on high aspect ratio structures or structures with complex morphologies. This lack of conformality is derived from the fact that PVD is typically a line-of-sight technique. This means that all of the surfaces of the substrate must be within the view of the metal source in order for a the vaporized metal to condense on the surface. If the substrate is not flat, three dimensional structure on the surface may act as masks thereby blocking the line-of-sight path to the metal source. In the case of high aspect ratio structures or porous material it may also be difficult to obtain a uniform film below the surface due to lack of line-of-sight.

2.2 Sol-gel techniques

Sol-gel techniques involve solution based chemistries to grow thin films of metal oxides [196]. During a sol-gel process a metal oxide network is formed by the progressive condensation of metal hydroxides [196]. Typically a metal alkoxide ($M(OR)_n$, M = Si, Ti, Zr, Al, Fe, B) in a solution (sol) of alcohol will first undergo hydrolysis to form $M(OH)_n$. The $M(OH)_n$ monomers then begin to polymerize via condensation reactions to form particles of the metal oxide [196]. Eventually a continuous network is formed and the solution thickens (gel) [196]. A sol-gel film can be applied to a flat substrate by dip coating or spin coating, or it may be applied to particles by mixing the particles in to the sol-gel solution [196].

After the sol-gel coating is applied, a heat treatment removes excess solvent and reaction

byproducts. There are large volume contractions that coincide with the removal of the solvents; these can lead to cracks in the sol-gel film. Depending on the morphology required, great care must be taken during the curing process to avoid cracks [196].

2.3 Chemical vapor deposition

CVD is gas phase method for depositing thin films [48]. In CVD one or more volatile precursors is exposed to a heated substrate surface where it may react with the substrate surface or thermally decompose onto the substrate surface to grow a film. The surface reaction or decomposition produces volatile reaction products that are pumped from the reaction chamber during growth. CVD is capable of growing films with nanometer thickness control[48].

The five classes of CVD reactions are thermal decomposition, reduction, oxidation, hydrolysis and synthesis [48]. Table 2.1 show several example CVD chemistries classified by the reaction type. Thermal decomposition is typically used to make a film consisting of one element. The reaction products in for thermal decomposition reaction do not usually attack the substrate. Reduction reactions are typically used to make a film consisting of one element. The products of the reduction reaction can etch the substrate or drive the reaction in reverse. Hydrogen is the most commonly used reducing agent. Hydrolysis and oxidation reactions are used to deposit metal oxide films. Synthesis reactions are used to grow binary compounds like carbides or borides [48].

CVD has the advantage of being able to grow relatively thick films quickly. CVD has the limitation that many chemistries must be done at high temperature (> 600 ℃). The high temperatures may be incompatible with some substrates. Reactions of CVD precursors in the gas phase can form particles that are then deposited on the surface leading to nonuniform film growth. Since the growth rate of films grown with CVD is proportional to the reactant flux, care must be taken to ensure that a uniform flux reaches every surface in order to grow a uniform film. Obtaining a uniform flux on complex morphologies can be difficult.

Table 2.1: Types of CVD reactions with example chemistries and reaction temperatures.

CVD Reaction Type	Example Reactions	Temperature (℃)
Thermal Decomposition	$SiH_4 \rightarrow Si + 2\ H_2$	600-1150
	$TiI4_4 \rightarrow Ti + 2\ I_2$	1200
Reduction	$SiCl_4 + 2\ H_2 \leftrightarrow Si + 4\ HCl$	900-1200
	$WF_6 + 3\ H_2 \leftrightarrow W + 6\ HF$	550-800
Oxidation	$SiH_4 + 2\ O_2 \rightarrow SiO_2 + 2\ H_2O$	350
	$Zn(C_2H_5)_2 + 4\ O_2 \rightarrow ZnO + 2\ CO\ 5\ H_2O$	250-500
Hydrolysis	$AlCl_3 + 3\ CO_2 + 3\ H_2 \rightarrow Al_2O_3 + 3\ CO + 6\ HCl$	800-1150
	$2\ Al(CH_3)_3 + 3\ H_2O \rightarrow Al_2O_3 + 6\ CH_4$	
Synthesis	$3\ TiCl_4 + 2\ BCl_3\ 5\ H_2 \rightarrow TiB_2 + 10\ HCl$	1100

2.4 Atomic layer deposition

Atomic layer deposition (ALD) is a gas phase technique for depositing thin films on solid surfaces [79, 125]. ALD relies on sequential, self-limiting, surface reactions. Once a gas phase precursor has reacted with a surface functional group, that surface functional group has been consumed. It does not matter if there is an excess of the gas phase precursor, the limiting reagent in the reaction are the substrate surface functional groups. Typical ALD chemistries employ a binary reaction sequence where the exposure to the first ALD precursor deposits one atomic layer of one component of the binary material being deposited and generates a new surface functionality. This is commonly refereed to as the A-step. Exposing the surface to a second ALD precursor deposits one atomic layer of the second binary component of the material being deposited and regenerates the original surface functionality of the substrate. This is commonly called the B step. Repeating the process ABAB. . . allows for digital thickness control determined by the growth rate per cycle and the number of AB cycles.

The invention of ALD is often dated with a 1974 patent by a Finnish group led by Suntola [182]. The first ALD system studied by the Finnish team was ZnS using Zn and S as reactants. Russian researchers led by Aleskovskii had in fact been studying ALD since the 1960. The first

published account of ALD by the Russian team came in 1974 [5]. Since its inception, the field of ALD has grown rapidly. Figure 2.2 show the number of publications regarding ALD as a function of time.

Figure 2.3 shows a schematic of the most general ALD process. A solid substrate with one surface functionality is exposed to reactant A. This results in the complete consumption of the functional groups on the solid substrate and the generation of a gaseous reaction byproduct. After a sufficient exposure time the excess A reactant and the reactions byproducts are evacuated from the reaction chamber. The new surface functionality is then exposed to reactant B. This results in the complete consumption of the functional groups on the solid substrate left from the exposure to reactant A and the generation of a gaseous reaction byproduct. After a sufficient exposure time the excess B reactant and the reactions byproducts are evacuated from the reaction chamber. Exposure to reactant B has completed one ALD cycle and returned the surface to its original functionality. The A step and the B step of a binary ALD reaction are often referred to as half reactions.

A key characteristic of any ALD process is that the chemistry is self-limiting. The self-limiting nature of ALD is a crucial component for coating porous and high aspect ratio samples. This allows for a uniform film even when the conduction path varies from an exposed surface to a deep trench or otherwise tortuous path. A point at the bottom of a high aspect ratio trench will receive a lower flux of precursor molecules than at the surface of the substrate. Because ALD employs self-limiting chemistries, precursor molecules adsorb and desorb from reacted sites near the top of a high aspect ratio trench as they proceed toward the bottom. This allows for conformal coatings over the full surface of the substrate. To ensure uniform, conformal films, ALD precursors that do not react with themselves must be employed. This allows for an overexposure of any individual precursor without loss of thickness control. Also, great care must be taken to separate the exposure of reactant A and reactant B. Typically this separation is done in time. In this case one reactant is exposed to the substrate surface, excess reactant and reaction byproducts are then removed from the reaction chamber and then at some later time the second reactant is exposed to the substrate surface. Recent advancements in atmospheric ALD separate ALD precursors spatially [128]. In the

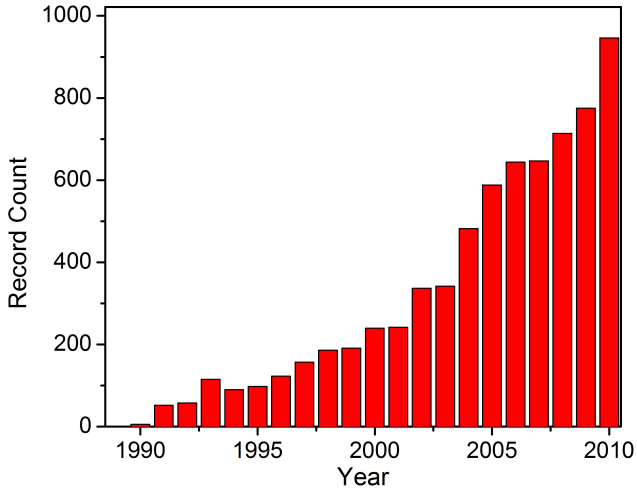

Figure 2.2: The number of publications regarding ALD as a function of the year.

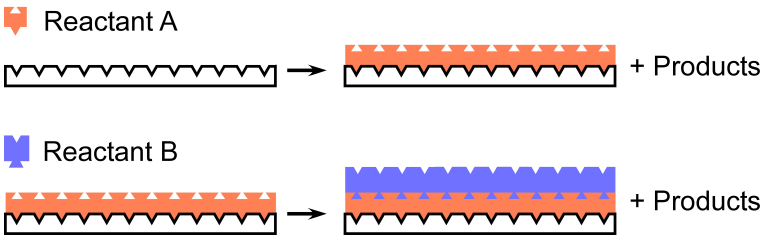

Figure 2.3: Schematic of the most general ALD process

case of atmospheric ALD the ALD precursors are in separate regions and the substrate surface is passed through the distinct regions. The number of ALD cycles completed with atmospheric ALD is determined by the number of A and B regions and by the number of times the sample surface is oscillated beneath the regions.

ALD reactions are temperature dependent [181]. An ideal ALD process only takes place within a specific temperature window. Figure 2.4 illustrates how the growth rate of an ALD chemistry varies with temperature. If the reactor temperature is too low reactants may condense on the substrate leading to a higher growth rate. Conversely, at low temperatures reactant molecules may not have enough thermal energy to drive the reaction to completion. In this case the growth rate will be lower. At temperatures above the ALD window elevated growth rates may be observed if the reactants decompose. This elevated growth rate is similar to unimolecular chemical vapor deposition. Conversely, at higher temperature the ALD precursors may not be stable on the surface leading to a reduced growth rate.

ALD relies on saturation of available surface functionalities. If a film grown by ALD does not go to completion the density of available surface sites will diminish. To ensure the surface reactions run to completion ALD chemistries are typically very exothermic. For example, the chemical reactions to grow Al_2O_3, ZnO and TiO_2 and their reaction enthalpies are [1]:

$$2\,Al(CH_3)_3 + 3\,H_2O \rightarrow Al_2O_3 + 6\,CH_4, \quad \Delta H = -1574.6\,kJ, \tag{2.1}$$

$$Zn(C_2H_5)_2 + H_2O \rightarrow ZnO + 2\,C_2H_6, \quad \Delta H = -292.9\,kJ, \tag{2.2}$$

$$TiCl_4 + 2\,H_2O \rightarrow TiO_2 + 4\,HCl, \quad \Delta H = -67.4\,kJ. \tag{2.3}$$

Equation 2.1 is a highly exothermic reaction. In many ways the trimethylaluminum (TMA)/H_2O chemistry is an is an ideal ALD process [79, 156]. The growth of Al_2O_3 is a feature in Chapters 5-7 and will be reviewed briefly here. The sequential, self-limiting reaction sequence during Al_2O_3 ALD is [58, 84, 149]:

A $$AlOH^* + Al(CH_3)_3 \rightarrow AlO - Al(CH_3)_2^* + CH_4 \tag{2.4}$$

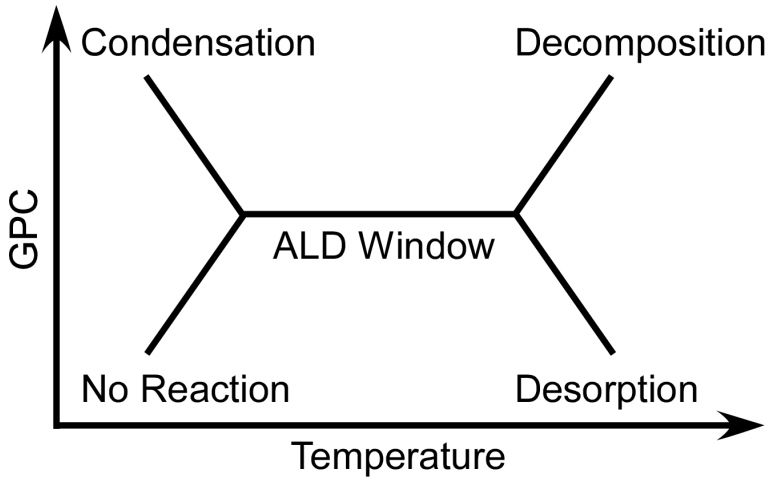

Figure 2.4: Growth per cycle (GPC) as a function of temperature. Adapted from [180].

B $$AlCH_3^* + H_2O \rightarrow Al - OH^* + CH_4 \quad (2.5)$$

where the asterisks denote surface species. Figure 2.5 shows a schematic of the TMA/H_2O reaction to grow Al_2O_3 with ALD. In frame 1 TMA is dosed into the ALD reaction chamber and reacts with the hydroxyl terminated surface to produce CH_4. In frame 2 CH_4 and excess TMA are purged from the reactor. Frames 1 and 2 constitute the A step in the TMA/H_2O ALD reaction. In frame 3 H_2O is dosed into the ALD reaction chamber and reacts with the methyl terminated surface to produce CH_4. In frame 4 CH_4 and excess H_2O are purged from the reactor. Frames 3 and 4 constitute the B step in the TMA/H_2O ALD reaction.

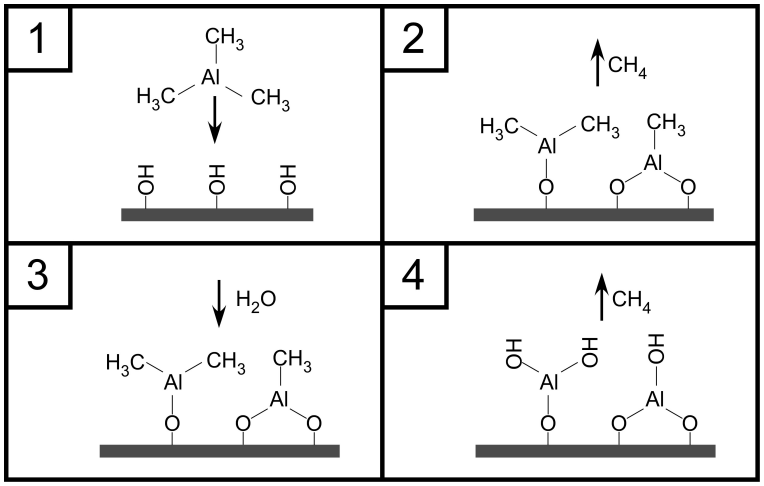

Figure 2.5: Schematic of the TMA/H_2O reaction to grow Al_2O_3 with ALD.

Chapter 3

Thin Films for Lithium Ion Batteries

Since their commercialization in the 1990s lithium ion batteries (LIBs) have been an effective energy storage medium for portable electronics [185, 203, 209]. LIBs have been proposed as a power source for hybrid electric vehicles [34, 179, 178]. Limitations in LIBs such as short lifetimes, low durability, high cost and poor low temperature performance have hindered commercial success in electric vehicles [40].

It has been widely documented in the literature that additions to the LIB active materials can improve the LIB performance. Additions refers to materials that are not intended to store Li but serve to enhance the performance of the materials that do store Li (active materials). These additional materials can take many forms. A few examples include thin films grown on the active material surface that may or may not be conformal; nanoparticles grown on the active material surface that may be uniform and dense enough to be referred to as a film or may be sparsely distributed on the active material surface; or simply mixing in the additional material i.e. not attempting to grow the material on the active material surface. The mechanisms by which these additional materials enhance LIBs is varied. In this chapter a review of the proposed mechanisms for enhancement of LIBs by the addition non-active material substances will be presented..

3.1 Mechanisms for thin films to enhance LIBs

In order to improve the performance of LIBs a variety of surface coating materials have been used to alter the LIB active material interface. The coating materials previously investigated

include metal oxides [45, 39], metal phosphates [8, 20], metal fluorides [176, 175], metal carbonates [221]and carbon [24, 38, 224, 33]. The proposed mechanisms for the enhanced performance of coated active materials include: acting as a sacrificial scavenger for HF; enhancing electron conduction at the active material surface; changing the active material surface chemistry; acting as a physical barrier between the active material and the electrolyte.

3.1.1 Thin films for scavenging HF

The primary salt in a LIB electrolyte is Lithium hexafluorophosphate ($LiPF_6$). In the presence of H_2O, $LiPF_6$ reacts to form HF according to the following reactions [100]:

$$LiPF_6 \leftrightarrow LiF + PF_5 \tag{3.1}$$

$$PF_5 + H_2O \rightarrow POF_3 + 2HF. \tag{3.2}$$

The resultant HF can then act to dissolve transition metals in the cathode active material [88, 186, 229]. The dissolution of these transition metals results in structural changes in the cathode material and the degradation the LIB's capacity [146]. It has been reported that metal oxide particle can be employed to sacrificially react with the HF to form stable insoluble compounds [133]. The metal oxide can be applied in several forms: as a discontinuous thin film [148], as particles mixed in with the active material, as a pretreatment to the electrolyte prior to cell fabrication [133] or as a thin conformal thin film [98]. Examples of of Al_2O_3 and ZrO_2 reacting with HF and the reaction enthalpy are given in equations 3.3 and 3.4.

$$Al_2O_3 + 6HF \rightarrow 2AlF_3 + 3H_2O, \quad \Delta H = -583.8\,\mathrm{kJ} \tag{3.3}$$

$$ZrO_2 + 4HF \rightarrow ZrF_4 + 2H_2O, \quad \Delta H = -303.5\,\mathrm{kJ} \tag{3.4}$$

AlF_3, ZrF_4 and other metal fluorides are typically insoluble in nonaqueous electrolytes. In the case of thin films of protective metal oxides, as opposed to particles, the subsequent metal fluoride film may act as a protective barrier.

3.1.2 Thin films for enhanced electron conduction

Carbon films have been used to enhance the performance of several phosphate materials, for example $LiFePO_4$ [24, 38]. Typically phosphate materials exhibit low electron conductivity [158, 7]. As such the growth of a conductive carbon film improves the conductivity of the composite material and the overall cathode performance accordingly. There are two proposed mechanisms for the increase in the conductivity. A thin film of a highly conductive carbon material will have a large surface area for interaction with the active material surface. By having a large surface area at the interface between the poorly conducting active material and the highly conductive carbon film the charge transfer ar the interface may be improved. Alternatively, a conductive carbon film on the cathode surface may increase the interparticle and particle-current collector conductivity. Both of these mechanisms may play a role in the observed enhanced performance of metal phosphate electrodes.

Carbon films are typically deposited on metal phosphate active material by the thermal decomposition of a carbon source such as a hydrocarbon, acetate or carbohydrate. The deposition is typically carried out while the active material is in particle form. Deposition temperatures range from 500-800 ℃. However, higher temperature carbon depositions ($>$ 700 ℃) exhibit an increased electronic conductivity as compared with lower temperature depositions ($<$ 600 ℃) [223]. The increased conductivity for the higher temperature depositions is attributed to the carbon film being more graphitic in nature [223].

It has also been demonstrated that the deposition of an insulating material, such as Al_2O_3, followed by annealing can lead to the migration of Al atoms into the active material. Oh *et al.* argue that $LiCoO_2$ coated with a film of Al_2O_3 via gas suspension spray techniques and then annealed at 500 ℃ forms a Li-Al-Co-O on the first 15 nm of the $LiCoO_2$ [148]. Measurements of the composite $LiCoO_2/Al_2O_3$ displayed an order of magnitude drop in the volume resistivity as compared to the bare $LiCoO_2$. This result is surprising because $LiCoO_2$ is a better conductor then Al_2O_3. It is postulated that this drop in the resistivity contributed to the improved electrochemical

performance of the $LiCoO_2$ coated with Al_2O_3 as compared to the bare $LiCoO_2$.

3.1.3 Thin films as protective barriers

Thin films on the surface of the battery active material may serve as a physical barrier to separate the active material from the electrolyte. The presence of a barrier means that the surface of the active material cannot react with the electrolyte. Possible reactions include the reduction of the delithiated metal oxide by the electrolyte or the evolution of O_2 gas [12]. These reactions occur at or near the surface of the active material particles. For a surface mediated reaction a chemically and electrochemically inert barrier can prevent the two reactants from coming into contact. For reactions within the active material a chemically and electrochemically inert barrier will slow the transport of reactants into the active material.

3.1.3.1 Al_2O_3

Several metal oxides have been employed on a variety of active materials. Al_2O_3 has been deposited on $LiCoO_2$ using sol-gel methods [46] and gas suspension spray techniques [148]. Al_2O_3 has a good Li^+ ion conductivity and is chemically and electrochemically stable in LIBs [129]. These qualities make it a good candidate for a physical protection barrier in LIBs. It has been demonstrated that Al_2O_3 films on $LiCoO_2$ can greatly improve the rate capability, capacity retention with cycling and thermal stability [148, 120].

Films deposited with gas suspension spray techniques did not produce conformal films. On $LiCoO_2$ particles with an average size of 7.7 μm a range of film Al_2O_3 thicknesses deposited with gas suspension spray techniques has been explored [148]. It was determined that films accounting 0.2 weight % of the composite $LiCoO_2/Al_2O_3$ material displayed the best performance [148]. This weight % corresponds to a surface coverage of 13.7%. At a surface coverage of 13.7 % this film is not close to conformal [148]. However, it has been demonstrated that an Al_2O_3 film can still act as a protective barrier to prevent Co dissolution [148]. In one experiment bare $LiCoO_2$ and $LiCoO_2$ coated with 0.2 weight % of Al_2O_3 were immersed in a solution 1 M $LiPF_6$ in ethylene carbonate

: dimethyl carbonate : ethylmethyl carbonate (1:1:1) for 1 week [148]. The dissolved Co^{4+} in the solution was measured with atomic adsorption spectroscopy and it was determined that the bare $LiCoO_2$ had lost 2.3 times more Co^{4+} [148].

3.1.3.2 $AlPO_4$

$AlPO_4$ films have be deposited on $LiCoO_2$ particles. The films were grown by mixing $LiCoO_2$ particles into a slurry of $AlPO_4$ nanoparticles, drying the particles in an oven and then heat annealing the particles at elevated temperatures [43]. The thickness of the $AlPO_4$ film was controlled by changing the concentration of the $AlPO_4$ in the slurry [42, 122].

It is believed that $AlPO_4$ films can function in several ways to protect the $LiCoO_2$ active material. $AlPO_4$ films serve as a physical protection barrier to prevent reactions between $LiCoO_2$ and the electrolyte. Cho observed that the thickness of the $AlPO_4$ films inversely correlated with the amount of electrolyte that exothermically reacted with the $LiCoO_2$ [42]. Beyond 4.2 V $LiCoO_2$ begins to undergo rapid side reactions with the electrolyte [146]. In an overcharge experiment designed to test the safety aspects of overcharging $LiCoO_2$ to 12 V, Cho observed a plateau at 5 V. This plateau was consistent with electrolyte oxidation and reactions between the electrolyte and the $LiCoO_2$ [42]. For $LiCoO_2$ that had been coated with 50, 200 and 1000 $\mathring{A}$ of $AlPO_4$, the duration of the 5 V plateau was successively reduced by thicker films [42]. This implies that thicker films are better able to act as a physical barrier between the electrolyte and the $LiCoO_2$.

3.1.3.3 Carbon

Thermal vapor deposition has been employed to coat protective carbon films onto natural graphite NG to prevent interactions between the NG and a propylene carbonate (PC) electrolyte [218, 217, 198]. Increasing the thickness of the protective carbon film increased the battery performance. For example, Yoshio *et al.* observed that NG coated with an 8.6 weight % protective carbon coating had a coulombic efficiency on the first charge-discharge of 75.8% [218]. The coulombic efficiency was increased to 92.5% by essentially doubling the weight % of the protective carbon

coating to 17.6% [218]. These two experiments used an electrolyte that was only 20% PC (PC:DMC, 1:4 by volume) [218]. If the concentration of the PC in the electrolyte was increased the battery performance suffered. The first cycle coulombic efficiency for a 17.6 weight % protective carbon film in an electrolyte that was 33% PC (PC:DMC, 1:2 by volume) was only 71.0% [218]. This is a dramatic reduction in the first cycle coulombic efficiency, 92.5% $\rightarrow$ 71.0%, with only a 13% increase in the concentration of the PC in the electrolyte, 20% $\rightarrow$ 33% [218]. Furthermore, the weight % of protective carbon film used in this study, and others, are a significant portion of the mass of the active material [218, 217, 198, 197, 119].

3.1.3.4 MgO

MgO has been deposited on $LiCoO_2$ using a $Mg(OH)_2$ solution followed by a heat treatment [199], pulsed laser deposition [93]and sol-gel methods [144, 227]. MgO acts as a barrier between the $LiCoO_2$ and the electrolyte thereby preventing the dissolution of Co^{4+} ions [131]. By preventing Co^{4+} dissolution the structure of the $LiCoO_2$ is maintained and the cell performance is enhanced [131]. It also been noted that Mg^{2+} may migrate into the $LiCoO_2$ during annealing or during charge-discharge cycles [227]. The addition of the Mg^{2+} may help stabilize the delithiated CoO_2 [227].

After 40 charge-discharge cycles $LiCoO_2$ coated with 1 mol% of MgO by sol-gel methods had a capacity of 120 mAh/g while bare $LiCoO_2$ had a capacity of 13 mAh/g [227]. For films that were thicker, 2 and 3.8 mol% the charge-discharge performance was drastically worse. This decline in performance was attributed to the low Li^+ conductivity of MgO.

3.1.3.5 TiO_2

TiO_2 coated $LiNi_{0.8}Co_{0.2}O_2$ has been produced by the hydroxylation of tetra-n-butyl titanate on the $LiNi_{0.8}Co_{0.2}O_2$ surface under ambient conditions. The coated material then underwent a heat treatment at 400 ℃. Under these conditions a TiO_2 film of 50 nm was produced [225]. In electrochemical studies it was demonstrated that TiO_2 coated $LiNi_{0.8}Co_{0.2}O_2$ had improved

capacity retention. This was attributed to suppressed decomposition of the electrolyte on the TiO_2 as compared to the $LiNi_{0.8}Co_{0.2}O_2$ surface [226, 132].

3.1.4 Enhanced Surface Chemistry with Thin Films

The role of the surface chemistry of cathode active materials and their interaction with the electrolyte plays a significant role on the electrochemical performance of the active material [40]. The correlation between electrochemical performance of cathode active materials and the effect of the active material surface chemistry are not well characterized in the LIB literature [40]. Much of the LIB literature involves active materials that were recently synthesized and stored under ideal conditions. Many of the techniques used to coat LIB active materials involve a heat treatment. In contrast to fresh active materials or active materials that have been subject to a coating technique that involved a heat treatment, it has been observed that $LiCoO_2$ that is exposed to H_2O displays a large loss in specific capacity [37]. The loss in capacity could be recovered in part by either by heat treating the $LiCoO_2$ at 550 ℃ or by grinding the $LiCoO_2$ into a fine powder [37]. Grinding the $LiCoO_2$ powder exposes fresh $LiCoO_2$ surfaces, this implies that the the loss of capacity upon H_2O exposure is mediated by the surface of the $LiCoO_2$.

Chapter 4

Atomic Layer Deposition of LiOH and Li_2CO_3 Using Lithium t-butoxide as the Lithium Source

4.1 Abstract

Atomic layer deposition (ALD) was utilized to grow LiOH and Li_2CO_3 films using lithium tert-butoxide, H_2O and CO_2. Film growth was monitored with a quartz crystal microbalance between 100-295 ℃. At 225 ℃ LiOH ALD had a growth rate of 7.6 ng·cm^{-2}·cycle^{-1} before displaying evidence for hygroscopic behavior. At 225 ℃ Li_2CO_3 ALD had a growth rate of 10.4 ng·cm^{-2}·cycle^{-1}. H_2O production during the conversion of LiOH to Li_2CO_3 by exposure to CO_2 was monitored with quadrupole mass spectrometry. The film identities were confirmed using Fourier transform infrared and X-ray photoelectron spectroscopies. Lithium-containing films are present in the solid-electrolyte interphase (SEI) on graphite anodes of Li-ion batteries. The ALD of an artificial SEI layer may limit lithium loss and improve the capacity stability during charge-discharge cycles.

4.2 Introduction

Lithium ion batteries (LIBs) are the dominant power source for portable electronics, laptops, mobil phones etc. [11]. However, in order to realize LIBs in large-format technologies, such as power grid storage and electric vehicles, significant progress must be achieved in making them safer [81, 2]. The safety, shelf life and power capability of a LIB are determined in large part by the solid-electrolyte interphase (SEI) on the anode [142]. The SEI is formed by the reductive decomposition

of the electrolyte on the anode surface during the first few charge-discharge cycles [17, 92, 22].

The safety issues that arise for LIBs in large-format technologies are brought on by the requirement the LIBs be capable of fast charging and the elevated temperatures that coincide with fast charging. For example, in an electric vehicle the battery must be able to charge at the rate at which power is generated by regenerative breaking. If the LIB can dissipate the heat generated by fast charging the cell temperature will not rise dramatically. If the LIB cannot dissipate heat fast enough then a threshold under which the SEI can start to undergo a rapid exothermic decomposition may be crossed [173, 159]. The destruction of the SEI provides for direct contact between the lithiated anode and the electrolyte leading to more exothermic reactions. The further rise in temperature from the exothermic reactions will accelerate more chemical reactions in a process known as thermal runaway [173, 21]. Pressure generated during these reactions can cause mechanical failures resulting in the rupture of cell casing [21]. Most LIB employ flammable electrolytes. Upon the rupture of the cell casing, heat and flammable electrolytes can lead to fire and explosion [21]. A stable SEI is critical to the safety of LIBs [142].

Graphite is a common anode material in LIBs [73, 185]. With its high reversible capacity (372 mA h g^{-1}, assuming a stoichiometry of LiC_2), low cost, moderate volume change, and low and flat voltage range, natural graphite (NG) is a promising anode material [217, 77, 165]. The SEI layer restricts lithium diffusion and electron conductivity to the graphite electrode [151, 214]. Lithium bound in the SEI layer is no longer free to participate in charge transfer and as such lowers the battery capacity [151, 214]. The composition of the SEI layer includes various lithium compounds such as Li_2CO_3, Li_2O, LiOH, LiF and R-OLi [151, 60]. The deposition of an artificial SEI layer on the graphite anode may be useful to prevent lithium loss and limit capacity reduction during charge-discharge cycling [105].

In this paper, two possible artificial SEI materials, LiOH and Li_2CO_3, are grown with atomic layer deposition (ALD) techniques using lithium tert-butoxide (LTB), H_2O and CO_2 as the reactants. ALD is a thin film deposition technique based on sequential, self-limiting surface reactions [78, 161]. ALD can deposit atomic layer controlled and conformal films on very high aspect sub-

strates [64]. In addition, ALD can be employed to deposit films on particles and on porous substrates [70]. ALD could be used to deposit artificial SEI layers either on graphite particles used to make the anode or on the porous anode formed from graphite particles.

4.3 Experimental

4.3.1 Chemicals and Materials

Lithium tert-butoxide ($LiOC(CH_3)_3$, LTB)with a purity of 98+% was obtained from Strem Chemicals (Newburyport, MA). HPLC (high performance liquid chromatography) grade H_2O was obtained from Honeywell International Inc. (Morristown, NJ). Ultra high purity N_2 and bone dry CO_2 were obtained by Matheson Trigas (Newark, CA). Trimethylaluminum ($Al(CH_3)_3$, TMA) with a purity of 97% was obtained from Sigma-Aldrich (Saint Louis, MO).

In order to remove dissolved gases the H_2O underwent 5 cycles of freeze-pump-thaw. All other precursors were used without further purification. The LTB was transferred into a stainless steel dosing vessel in a glove box under an Ar environment (Vacuum Atmosphere's Inc., Amesbury, MA). The H_2O and O_2 concentrations in the glove box were typically under 0.1 and 0.5 ppm respectively.

For *ex situ* analysis, LiOH and Li_2CO_3 were deposited on $\sim 1 \times 1$ inch Si wafers with a thin native oxide. The Si wafers were obtained from Silicon Valley Semiconductors, Inc. (Santa Clara, CA). The Si were cleaned with deionized water, acetone and isopropyl alcohol prior to film deposition. LiOH and Li_2CO_3 were also grown on KBr slides obtained from International Crystal Laboratories (Garfield, NJ). The KBr slides were used without further cleaning.

4.3.2 Deposition Parameters

The LiOH and Li_2CO_3 films were grown in a viscous flow ALD reactor that is described elsewhere [62]. A schematic of the reactor is shown in Figure 4.1. The reactor was operated at a pressure of $\sim$1 Torr with a total nitrogen carrier gas flow of 170 sccm. Nitrogen flow was

controlled with a mass flow controller (MKS Instrument, Andover, MA). The reactor was heated with two ceramic heaters (Watlow Electric Manufacturing Co., St. Louis, MO). The temperature was monitored with an external thermocouple and was controlled via PID loop with a temperature controller (Eurotherm U.S.A., Ashburn, VA). The pressure was measured using a Baratron capacitance manometer (MKS Instrument, Andover, MA). The precursors were introduced in the ALD chamber through a series pneumatic and needle valves. To prevent precursor condensation, the dosing line from each precursor vessel to the reactor was heated with a gradient of increasing temperature toward the reactor.

Unless otherwise noted, the following dosing conditions were used. The LTB source was held at 165 ℃ and the reactor was maintained at 225 ℃. The LTB dose was 3 s with a partial pressure of 35 mTorr. The H_2O dose was 1 s with a partial pressure of 250 mTorr. The CO_2 dose was 1 s with a partial pressure of 500 mTorr. The purge times after the reactant exposures were 60 s. LiOH and Li_2CO_3 films were grown on a fresh Al_2O_3 film.

4.3.3 Dosing Low Vapor Pressure Precursors

H_2O and CO_2 have excellent vapor pressures and can simply be dosed onto a stream of N_2 gas that entrains the precursor and carries it into the ALD reactor. This dosing scheme has been described in detail elsewhere [62]. When the vapor pressure of a precursor is low relative to the ALD reactor pressure it is difficult to dose the precursor onto a stream of N_2 gas. This was the case for the LTB. In order to dose low vapor pressure precursors the N_2 gas flowing into the ALD reactor was diverted over the headspace of the low vapor pressure precursor. This enables the entrainment of the low vapor pressure precursor by the N_2 gas. This dosing arrangement is depicted in Figure 4.2. A metered flow of N_2 gas was sent through a needle valve such that when the pneumatic valves bith in and out of the precursor vessel were opened, the change in conductance resulted in a only a small amount of N_2 gas being diverted over the head space of the precursor.

The custom dosing vessel was comprised of two 2.75” Conflat flanges. The lid flange was fitted with two 0.25” welded stainless steel lines that had VCR fitting on the ends of the tubes.

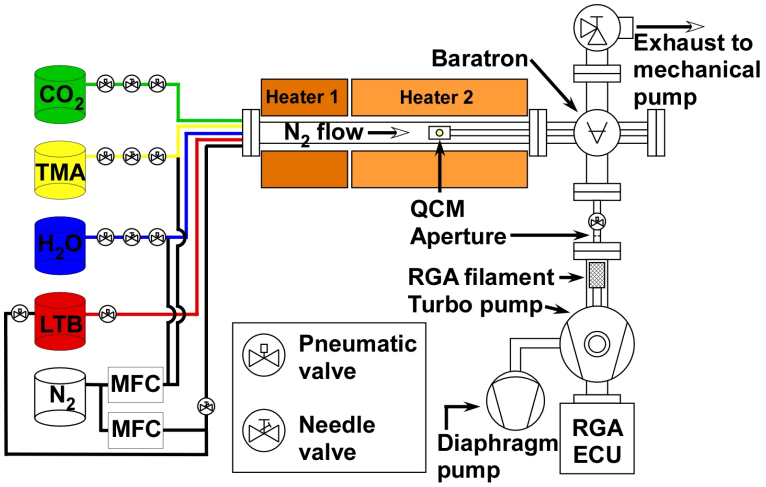

Figure 4.1: Schematic of viscous flow ALD reactor with a quart crystal microbalance and a quadrupole mass spectrometer.

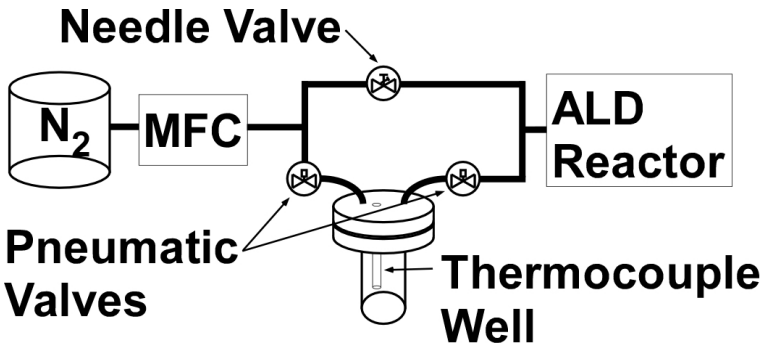

Figure 4.2: Schematic representation of bubbler used for dosing low vapor pressure precursors.

These comprised the inlet and outlet ports of the vessel. The lid also had a vacuum sealed stainless finger into which a thermocouple could be placed to monitor the precursor temperature. The vessel was a Conflat nipple that had been welded shut at a height of 2".

In a typical commercial dosing vessel of this type the inlet port does not stop at the bottom surface of the lid. Instead it continues down below the level of the precursor. This allows the entraining gas to actually bubble through a liquid precursor. In an ALD process this is not ideal because the bubbling process may entrain small droplets of liquid precursor which can result in undesirable dosing conditions. In the case of solid precursors a bubbling may entrain particles of the precursor which can also result in undesirable dosing conditions.

The pneumatic valves used to dose the precursor have open/close times on the order of 1 s. In order to ensure that the precursor only flowed forward toward the ALD reactor and not backwards into the N_2 gas line care was taken in the order in which the valves were opened. At the start of a dose the outlet (precursor to ALD reactor) pneumatic valve was opened 500 ms before the inlet (N_2 gas to precursor) pneumatic valve. At the end of a dose the inlet pneumatic valve was closed 500 ms before the outlet pneumatic valve.

4.3.4 Quartz Crystal Microbalance Monitoring

The reaction was monitored *in situ* with a quartz crystal microbalance (QCM). A detailed description on using QCM to monitor *in situ* ALD reactions is given elsewhere [62]. A Maxtek, Inc. BSH-150 (now owned by Inficon, East Syracuse, NY) sensor head was modified such that the cooling line could be used to flow N_2 gas over the back side of the QCM crystal. This gas flow prevented film growth from taking place on the back side of the crystal and minimized the pressure difference across the crystal. The N_2 gas flow was $\sim$20 sccm. This resulted in a pressure increase in the reactor of $\sim$100 mTorr. AT-cut quartz crystals with a polished gold surface and a frequency of 6 MHz were obtained from the Colorado Crystal Corp (Loveland, CO). The QCM crystals were sealed into the BSH-150 sensor head with a conductive epoxy obtained from Epoxy Technology, Inc. (Billerica, MA). During growth, the QCM was positioned horizontally and facing downward

in the middle of the ALD reactor.

Film growth was monitored with a Maxtek TM-400 (now owned by Inficon, East Syracuse, NY). QCM performance and health was monitored by the growth of Al_2O_3 with TMA and H_2O. The QCM crystal was replaced when the behavior of the Al_2O_3 growth deviated from acceptable values [208]. In between every experiment where LiOH or Li_2CO_3 was grown, 200 cycles of Al_2O_3 were grown on the QCM sensor. This allowed for verification of the sensor health and ensured that every LiOH and Li_2CO_3 started on an identical surface. The observed Al_2O_3 ALD growth rates were also used to calibrate the mass gains observed during LiOH and Li_2CO_3 growth.

4.3.5 Quadrupole Mass Spectrometry

Quadrupole mass spectrometry (QMS) was performed on the vapor phase species in the ALD reactor. Measurements were performed with a Stanford Research Systems RGA 200 (Sunnyvale, CA). The gases were sampled via an aperture shown in Figure 4.1. The aperture separated two distinct pressure regions, the ALD reactor ($\sim$1 Torr) and the QMS region ($\sim 1 \times 10^{-7}$ Torr). In order to maintain these pressures with an open conductance between the two regions, the QMS region was differentially pumped with a Varian V70LP turbo molecular pump (Palo Alto, CA). The aperture radius(r) was determined by Equation 4.1, where S is the pumping speed of the turbo molecular pump, P_{QMS} and T_{QMS} are the pressure and temperature in the QMS region, P_{ALD} and T_{ALD} are the pressure and temperature in the ALD reactor, m is the mass of the molecule being conducted and k is the Boltzmann constant.

$$r = 2\sqrt{\frac{S\,P_{\mathrm{QMS}}}{\pi\,P_{\mathrm{ALD}}\,T_{\mathrm{QMS}}}}\left(\frac{m\,T_{\mathrm{ALD}}}{3\,k}\right)^{1/4} \tag{4.1}$$

From Equation 4.1 it was determined that an aperture with a radius of 25 μm was appropriate. A dual thoriated-iridium (ThO_2/Ir) filament was used for electron emission in the mass spectrometer. The ionization energy was 70 eV. A Faraday cup was used as the detector. Data was collected as a function of time for mass to charge ratios (m/z) of 18.

4.3.6 Fourier transform infrared spectroscopy

Fourier transform infrared spectroscopy (FTIR) was used to determine the film identity. LiOH and Li_2CO_3 ALD films were grown on KBr slides (International Crystal Laboratories) and characterized *ex situ* with a Nicolet Avatar 360 FTIR (Thermo Fisher Scientific Inc.). Excess H_2O and CO_2 was purged with nitrogen for at least 20 minutes prior to background collection in order to minimize signal contamination. The spectrometer collected 100 scans and then took the average. Data was collected between 4000 and 400 cm^{-1} at a resolution of 4 cm^{-1}.

Due to the instability of LiOH in air, LiOH films were also grown in an ALD reactor equipped with *in situ* FTIR analysis that has been described elsewhere [216]. The *in-situ* FTIR studies were performed with a Nicolet Nexus 870 FTIR spectrometer equipped with a liquid-N_2 cooled mercury-cadmium-telluride infrared detector. Spectra were collected with a mirror speed of 1.8 cm s^{-1}, and averaged over 100 scans. The resolution of the spectrometer was cm^{-1}. The IR transparent windows were KBr disks supplied by International Crystal Laboratories. The *ex situ* IR beam path between the reactor and the KBr window was purged with H_2O and CO_2-free air delivered from a purge gas generator.

4.3.7 X-ray Photoelectron Spectroscopy

The LiOH and Li_2CO_3 films were also characterized *ex situ* with X-ray photoelectron spectroscopy (XPS). Measurements were performed with a Perkin-Elmer 5600 XPS using a monochromatic Al Kα source (1486.6 eV). The base pressure in the vacuum chamber during XPS analysis was 3×10^{-10} Torr. A constant analyzer energy mode was employed at a pass energy of 58.7 eV with a step size of 0.25 eV. All spectra were calibrated to the adventitious carbon peak at 285 eV. An electron beam neutralizer was employed at 17.8 mA. Data was collected with Auger Scan (RBD Instruments, Inc., Bend, OR). XPS data was analyzed in CASA XPS (Casa Software Ltd, UK).

4.4 Results and Discussion

4.4.1 LiOH ALD

LiOH film growth was monitored on the QCM. The overall binary reaction is $LiOC(CH_3)_3 + H_2O \rightarrow LiOH + HOC(CH_3)_3$. The AB binary reaction sequence during LiOH ALD is proposed to be:

A $$LiOH^* + LiOC(CH_3)_3 \rightarrow LiOH - LiOC(CH_3)_3^* \quad (4.2)$$

B $$LiOH - LiOC(CH_3)_3^* + H_2O \rightarrow LiOH - LiOH^* + HOC(CH_3)_3 \quad (4.3)$$

where an asterisk is used to denote surface species. LiOH-$LiOC(CH_3)_3$* is postulated to be a molecularly adsorbed species that reacts with H_2O to form LiOH.

The first 3 cycles during LiOH ALD on a fresh Al_2O_3 surface are shown in Figure 4.3. During the first 10 ALD cycles, the mass gain during the LTB exposure was Δm_A = 18.9 ng·cm^{-2}·cycle^{-1} and the mass loss during the H_2O exposure was Δm_B = -11.7 ng · cm^{-2} · cycle^{-1}. The $\Delta m_A/\Delta m_B$ ratio was -1.62. This ratio is close to the predicted ratio of -1.43 based on Equations 4.2 and 4.3. The growth rate during first 10 cycles of LiOH was 7.6 ng·cm^{-2}·cycle^{-1}. Assuming a LiOH bulk density of 1.45 g·cm^{-3} [202], the mass gain of 7.6 ng·cm^{-2}·cycle^{-1} is equivalent to a LiOH ALD growth rate of 0.5 Å/cycle^{-1}.

LTB has a molecular mass of 80.06 AMU. A mass gain of 30.1 ng·cm^{-2} corresponds to 1.4 × 10^{14} LTB molecules cm^{-2}. Al_2O_3 grown with ALD has a density of 3.0 g·cm^{-3} [84]. This equates to an Al_2O_3 density ($\rho_{Al_2O_3}$) of 1.8 × 10^{22} Al_2O_3 units cm^{-3}. An estimate of the density of hydroxyl groups on the Al_2O_3 after a H_2O dose is given by $(\rho_{Al_2O_3})^{2/3}/2$. The estimated value of the density of hydroxyl groups is 3.4 × 10^{14} hydroxyl groups cm^{-2}. This value is in close agreement with the density of LTB molecules on the surface. This may indicate that the adsorbed monolayer of LTB may be interacting with hydroxyl groups on the Al_2O_3.

After the first 10 LiOH ALD cycles, the mass changes evolve and display a much different behavior. Figure 4.4 shows the QCM results during cycles 198-200. LiOH is hygroscopic and can

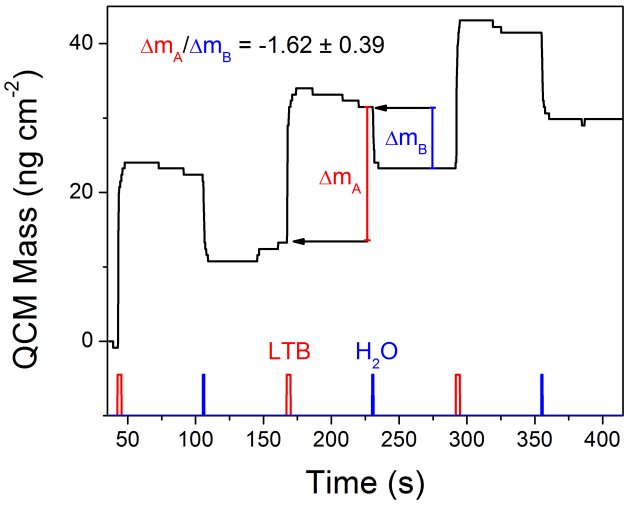

Figure 4.3: Mass gain during LiOH ALD using LTB and H_2O at 225 ℃ for cycles 1-3.

easily adsorb H_2O and form a hydrate [204]. The hygroscopicity is reversible and H_2O can desorb from the LiOH-hydrate during the purge times [204]. This H_2O desorption leads to the mass decays observed after both the LTB and H_2O exposures in Figure 4.4. To confirm the presence a LiOH-hydrate, films grown using 200 AB cycles were subjected to an extended N_2 purge at 225 ℃. The LiOH film lost ∼32% of its mass in 2 hours before reaching a stable value, this is shown in Figure 4.5. This mass loss is attributed to H_2O desorption from the LiOH-hydrate. A mass loss of 32% means that the LiOH film was initially 74% hydrated, *i.e.* 76% LiOH·H_2O and 24% H_2O.

The presence of H_2O in the ALD reactor during an LTB dose may have increased the growth rate of the LiOH by the process of chemical vapor deposition. For LiOH to be grown in true ALD fashion all excess water must be completely purged from the reactor after the H_2O dose. The time scale for this should be short at high temperatures with thin LiOH films, as was observed for the initial several cycles shown in Figure 4.3. After the appearance of the LiOH·H_2O, starting around 10 LiOH ALD, H_2O purge time in excess of 1000 s were still insufficient at completely dehydrating the LiOH·H_2O.

4.4.2 Li_2CO_3 ALD

LiOH is highly reactive with CO_2 to form Li_2CO_3 and H_2O [204]. The reaction enthalpy for this reaction is -134.3 kJ [1]. The reaction is so efficient that LiOH is used as a CO_2 scrubber by NASA in the shuttle spacecraft [94].

Li_2CO_3 ALD is based on a ternary ABC reaction sequence that utilizes the LTB and H_2O reactions given in Equations 4.2 and 4.3. In addition, a third reaction is added where LiOH can react with CO_2 to form Li_2CO_3 according to [204]:

C
$$\mathrm{LiOH} - \mathrm{LiOH}^* + \mathrm{CO_2} \rightarrow \mathrm{Li_2CO_3^*} + \mathrm{H_2O}, \tag{4.4}$$

where an asterisk is used to denote surface species. The reaction in Eqn. 4.4 relies on the presence of H_2O and has been shown to involve LiOH·H_2O (lithium hydroxide hydrate) according to [204]:

C1
$$2\mathrm{LiOH} + 2\mathrm{H_2O} \leftrightarrow 2\mathrm{LiOH} \cdot \mathrm{H_2O}, \tag{4.5}$$

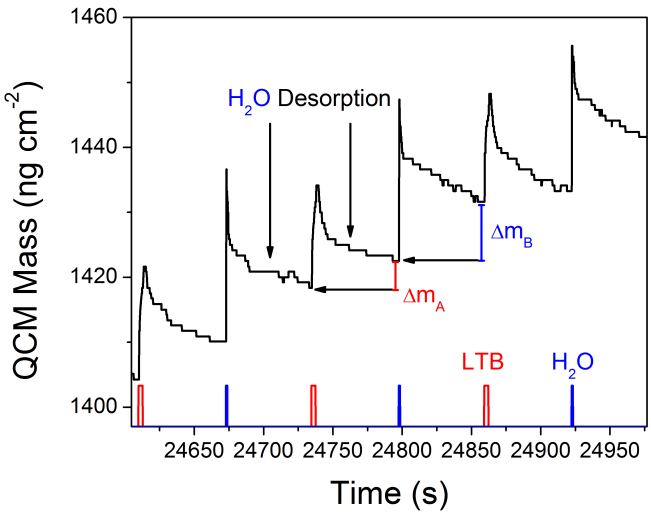

Figure 4.4: Mass gain during LiOH ALD using LTB and H_2O at 225 ℃ for cycles 198-200.

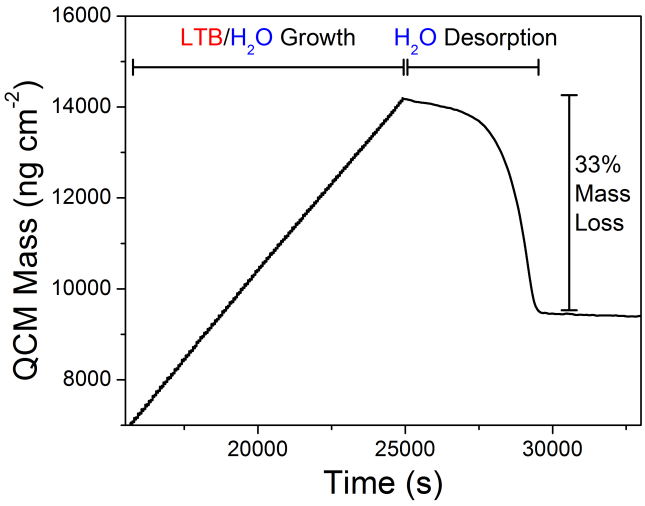

Figure 4.5: Mass gain during LiOH ALD using LTB and H_2O at 225 ℃ followed by mass loss as the LiOH film was dehydrated.

C2 $$2\mathrm{LiOH} \cdot \mathrm{H_2O} + \mathrm{CO_2} \rightarrow \mathrm{Li_2CO_3} + 3\mathrm{H_2O}. \quad (4.6)$$

Although H_2O is required to initiate the reaction, H_2O products sustain the reaction.

4.4.2.1 Converting LiOH to Li_2CO_3 with CO_2 Exposures

After depositing 8873.1 ng·cm^{-2} of dehydrated LiOH onto the QCM sensor, the sensor was exposed to repeated doses of CO_2. Figure 4.6 shows that with each CO_2 dose there is a mass gain on the QCM as the LiOH is converted to Li_2CO_3. After ∼31 CO_2 doses the mass on the QCM leveled off indicating that the conversion reaction had run to completion. The stoichiometric prediction for 100% conversion of LiOH to Li_2CO_3 is also shown in Figure 4.6. The actual mass change on the QCM is close to the stoichiometric prediction. It is possible that the initial mass of LiOH was overestimated due to some degree of hydration of the LiOH; this may account for the difference between the stoichiometric prediction and the final QCM mass.

Equation 4.4 indicates that the conversion of LiOH to Li_2CO_3 should produce H_2O as a reaction byproduct. Figure 4.7 shows the partial pressure of the mass fragment associated with H_2O ($m/z = 18$), as monitored with QMS. The production of H_2O correlated with the CO_2 doses and the mass increases on the QCM. As the mass increases on the QCM tapered off with subsequent CO_2 doses so did the signal for $m/z = 18$ mass fragment. The $m/z = 18$ mass fragment did not go to zero after the QCM mass increases leveled off. This may be due to an artifact from the CO_2 that appears at $m/z = 18$.

4.4.2.2 Li_2CO_3 ALD as an ABC Process

The first 3 cycles during Li_2CO_3 ALD on a fresh Al_2O_3 surface are shown in Figure 4.8. During the first 10 ALD cycles, the mass gain during the LTB exposure was $\Delta m_A = 19.8$ ng·cm^{-2}·cycle^{-1}, the mass loss during the H_2O exposure was Δm_B = -14.2 ng · cm^{-2} · cycle^{-1} and the mass gain during the CO_2 exposure was $\Delta m_C = 4.9$ ng · cm^{-2} · cycle^{-1}. The $\Delta m_A/\Delta m_B$ ratio was -1.39. This ratio is close to the predicted ratio of -1.43 based on Equations 4.2 and 4.3. The initial growth

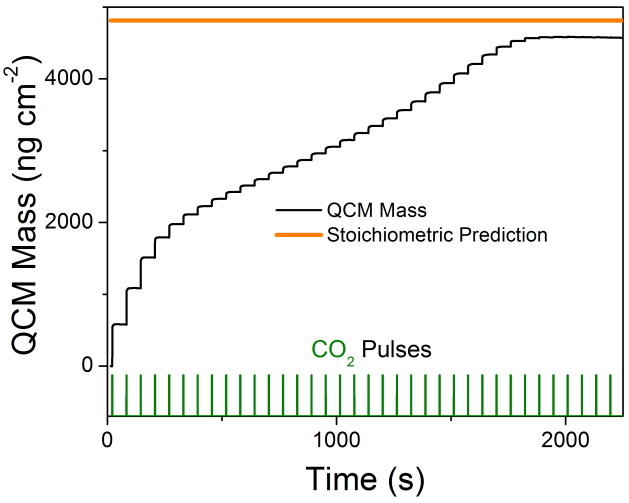

Figure 4.6: Mass increases on the QCM as LiOH is converted to Li_2CO_3 with doses of CO_2. The stoichiometric prediction for 100% conversion of LiOH to Li_2CO_3 is shown in orange.

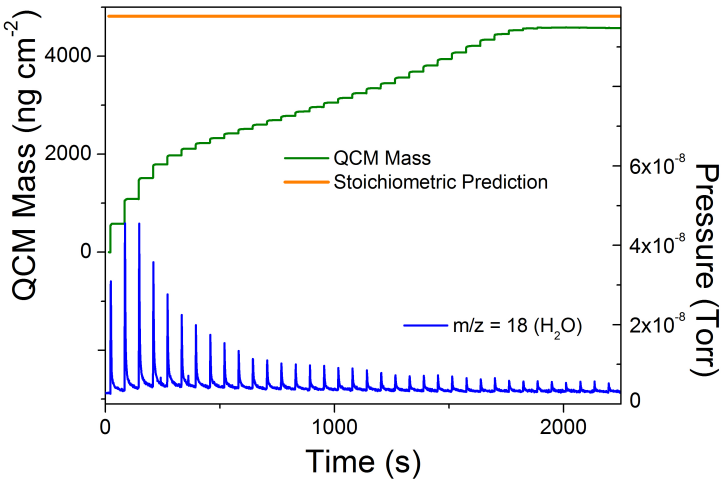

Figure 4.7: Mass increases on the QCM as LiOH is converted to Li_2CO_3 with doses of CO_2. The stoichiometric prediction for 100% conversion of LiOH to Li_2CO_3 is shown in orange. The partial pressure of H_2O ($m/z = 18$) from QMS correspond to the CO_2 doses and mass increase on the QCM.

rate during the first 10 cycles of Li_2CO_3 ALD was 13.4 ng·cm^{-2}·cycle^{-1}.

After ~10-15 cycles of Li_2CO_3 ALD on a fresh Al_2O_3 surface the growth rate decreased slightly to 10.4 ng·cm^{-2}·cycle^{-1} and was stable.

Figure 4.9 shows the QCM results during cycles 198-200 for the growth of Li_2CO_3 with ALD. The mass gain during the LTB exposure was Δm_A = 25.7 ngcm^{-2}cycle^{-1}, the mass loss during the H_2O exposure was Δm_B = -19.3 ngcm^{-2}cycle^{-1}, and the mass gain during the CO_2 exposure was Δm_C = 3.4 ngcm^{-2}cycle^{-1}. Compared with the nucleation regime, the magnitude of the mass gain per cycle of the LTB and the H_2O increased and the magnitude of the mass gain per cycle of the CO_2 decreased. The differences in the magnitudes of the mass gains and losses began to evolve after ~10-15 cycles of Li_2CO_3 ALD on a fresh Al_2O_3 surface. This difference was attributed to nucleation on the Al_2O_3. After ~10-15 cycles the growth rate decreased slightly to 10.4 ng·cm^{-2}·cycle^{-1} and was stable. Assuming a Li_2CO_3 bulk density of 2.11 g·cm^{-3} [202], the mass gain of 10.4 ng·cm^{-2}·cycle^{-1} is equivalent to a Li_2CO_3 ALD growth rate of 0.5 Å/cycle^{-1}.

Throughout the 200 cycles of Li_2CO_3 ALD the ratios of the mass gains, $\Delta m_A/\Delta m_B$, $\Delta m_C/\Delta m_A$ and $\Delta m_C/\Delta m_B$, stayed relatively constant. Figure 4.10 shows the mass ratios versus the number of ALD cycles. The mass ratios are $\Delta m_A/\Delta m_B$ = -1.47, $\Delta m_C/\Delta m_A$ = 0.14 and $\Delta m_C/\Delta m_B$ = -0.20. In comparison, the mass ratios calculated from Equations 4.2-4.4 are $\Delta m_A/\Delta m_B$ = -1.43, $\Delta m_C/\Delta m_A$ = 0.16 and $\Delta m_C/\Delta m_B$ = -0.23. These predicted ratios are given by the solid lines in Fig. 4.10. The agreement between the predicted mass ratios and the measured mass ratios is excellent and supports the reaction mechanism proposed in Equations. 4.2-4.4.

The mass gain per cycle (MGPC) as a function of the ALD reactor temperature for growth of Li_2CO_3 is shown in Figure 4.11. Below 130 ℃ the growth rate rapidly increased due to condensation of the LTB precursor on the QCM sensor. Above 250 ℃ the growth rate decreased. This decrease in growth rate was attributed to the inability to form an adsorbed monolayer of LTB on the surface of the QCM sensor. At 295 ℃ the growth rate rose, which may be due to the decomposition of the LTB precursor. Between 130-250℃ the growth rate was relatively stable, this temperature range is the ALD window. The average growth rate in the ALD window 9.2 ng·cm^{-2}·cycle^{-1} with a

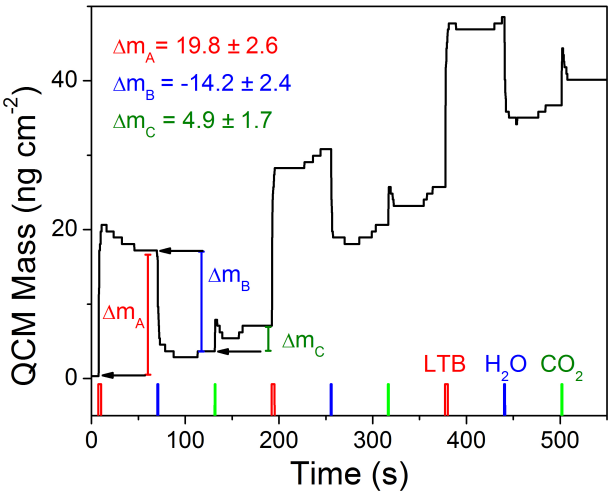

Figure 4.8: Mass gain during Li_2CO_3 ALD using LTB H_2O and CO_2 at 225 ℃ for cycles 1-3.

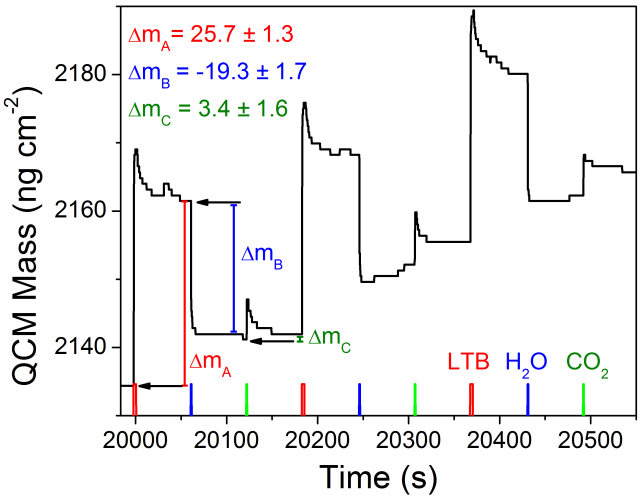

Figure 4.9: Mass gain during Li_2CO_3 ALD using LTB H_2O and CO_2 at 225 ℃ for cycles 198-200.

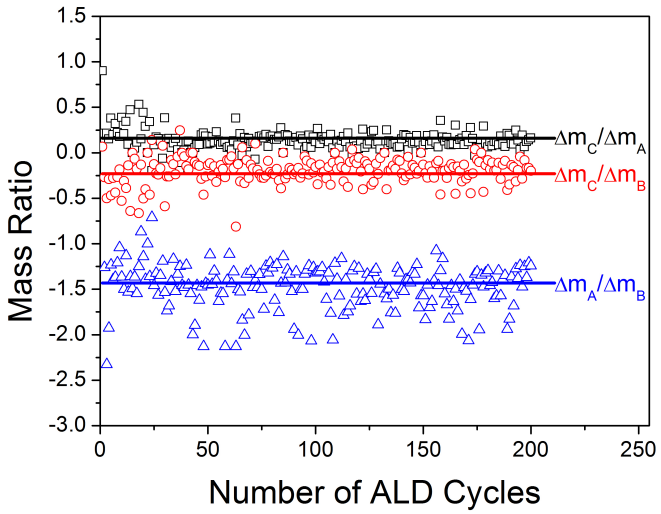

Figure 4.10: Mass ratios of the mass changes during the LTB (A), H_2O (B) and CO_2 (C) exposures versus the number of ALD cycles. The solid lines indicate the predicted values expected from Eqns. 4.2-4.4.

standard deviation of 0.6 ng·cm^{-2}·cycle^{-1}. Assuming that ALD Li_2CO_3 has the density of bulk Li_2CO_3, this growth rate equates to 0.44 Å·cycle^{-1} with a standard deviation of 0.03 Å·cycle^{-1}.

Figure 4.12 shows the MGPC of Li_2CO_3 ALD as a function of reactor temperature during nucleation on a fresh Al_2O_3 surface. The nucleation regime was defined as the first 10 ALD cycles. The data is somewhat irregular and is peaked at 205 ℃. The clear trends for condensation, desorption, and decomposition that were observe in the growth regime (Figure 4.11) beyond ∼10-15 ALD cycles were not apparent in the nucleation regime. It should be noted that overall the MGPC was higher in the nucleation regime than in the growth regime; this result is consistent with Figures 4.8 and 4.9.

Figure 4.13 shows the MGPC recorded by the *in situ* QCM as a function of the LTB exposure time for the nucleation regime (1st 10 ALD cycles) and the growth regime at 225 ℃. After a ∼2 s dose of LTB the the QCM sensor surface was saturated both in the nucleation regime and in the growth regime. Ignoring any pressure transients from the change in the conduction path as the N_2 was shifted from flowing directly into the ALD reactor to flowing into the ALD reactor and across the LTB bubbler headspace in parallel, a dose time of 2 s is equivalent to 70 mTorr·s.

4.4.3 Fourier Transform Infrared Spectroscopy

LiOH and Li_2CO_3 ALD films were also grown on KBr slides and characterized using *ex situ* FTIR. Removal of the LiOH film from the reactor resulted in the conversion of LiOH to Li_2CO_3 by ambient CO_2. Figure 4.14 shows an *ex situ* FTIR spectrum of Li_2CO_3. It did not matter whether LiOH or Li_2CO_3 ALD was grown on the KBr slide, Li_2CO_3 was observed after both LiOH and Li_2CO_3 ALD. The main absorption bands of Li_2CO_3 were observed at 1475 cm^{-1} and 1429 cm^{-1} for antisymmetric C-O stretching vibrations, 1088 cm^{-1} for symmetric C-O stretching vibrations, and 870 cm^{-1} for out of plane deformation modes [29]. All of these features are from the carbonate $CO_3{}^{2-}$ ion. For comparison, Figure 4.14 also shows a reference spectrum of Li_2CO_3 from the NIST Chemistry WebBook [174].

Figure 4.15 shows an *in situ* FTIR spectrum approximately 30 hours after 100 cycles of LiOH

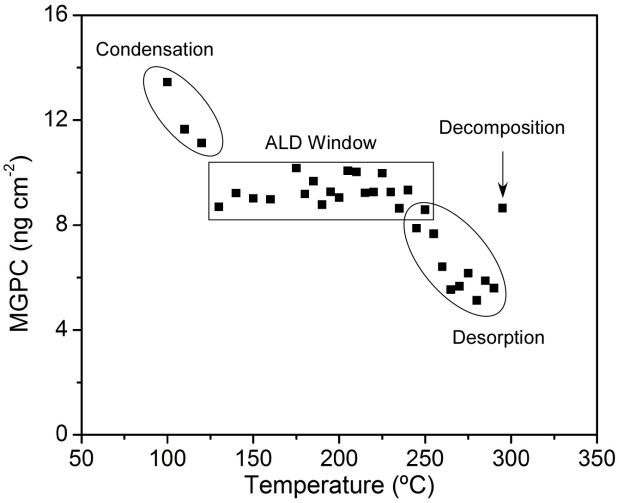

Figure 4.11: Mass gain per cycle (MGPC) of Li_2CO_3 in the growth regime.

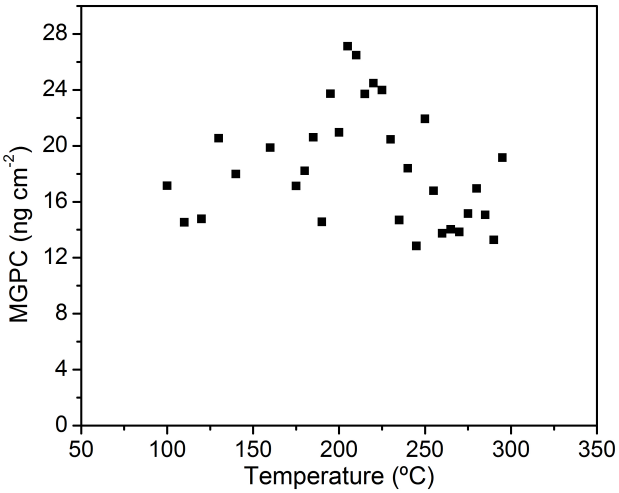

Figure 4.12: Mass gain per cycle (MGPC) of Li_2CO_3 ALD as a function of reactor temperature during nucleation on a fresh Al_2O_3 surface.

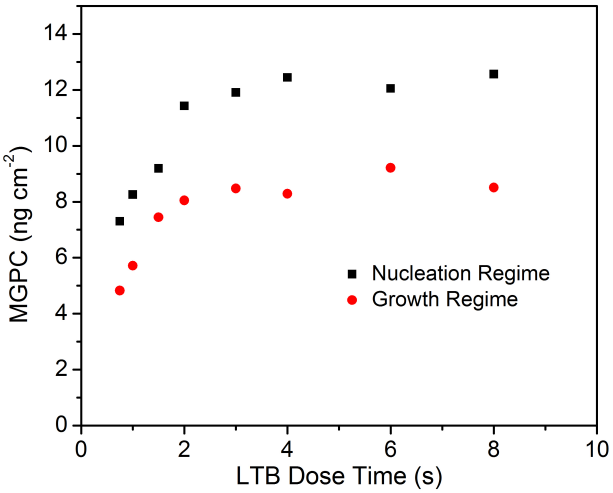

Figure 4.13: Mass gain per cycle (MGPC) as a function of the LTB exposure time for the nucleation regime (1st 10 ALD cycles) and the growth regime.

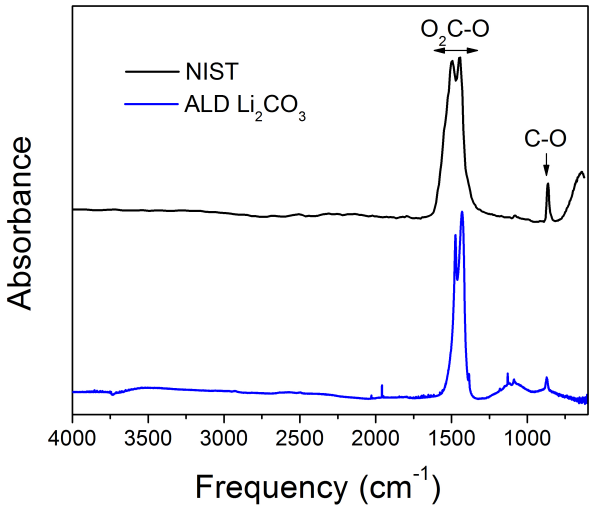

Figure 4.14: *Ex situ* FTIR spectrum of Li_2CO_3. For comparison a reference FTIR spectrum of Li_2CO_3 from NIST is also shown.

ALD on ZrO2 nanoparticles at 225 ℃. After deposition, the LiOH ALD film was maintained in the ALD reactor under vacuum. A sharp absorption peak was observed at 3672 cm^{-1} that is consistent with hydroxyl stretching vibrations from unhydrated LiOH [171, 97]. The O-H stretching vibration from H_2O in $LiOHH_2O$ is not observed at 3570-3574 cm^{-1} [171, 97]. The absence of this hydrate feature supports the identification of this film as LiOH.

There is also a broad absorbance feature from O-H stretching vibrations at 3720-3220 cm^{-1} in Figure 4.15. This absorbance could be caused by some hydrogen-bonded LiOH hydroxyls or some H_2O in the LiOH film [171, 97]. This absorbance feature also increased with subsequent H_2O exposure and decreased with purging time after H_2O exposure. However, the O-H stretching vibration from H_2O in $LiOHH_2O$ was never observed at 3570-3574 cm^{-1} after H_2O exposures to the LiOH ALD film.

The strong absorbances at 1496 and 1450 cm^{-1} in Figure 4.15 are assigned to antisymmetric C-O stretching vibrations from some Li_2CO_3 in the LiOH film [171, 29]. This feature is explained by the facile reaction of LiOH with background CO_2 in the ALD reactor [204, 171]. In addition, absorbance from C-H stretching vibrations at 3000-2817 cm^{-1} and C-O stretching vibrations at 1200 cm^{-1} indicates that some unreacted tert-butoxide groups remain in the film.

4.4.4 X-ray Photoelectron Spectroscopy

Figure 4.16 shows *ex situ* XPS spectra of the Li 1s, C 1s and O 1s peaks from LiOH and Li_2CO_3 films before and after Ar ion sputtering. For the LiOH film, conversion to Li_2CO_3 occurred upon exposure to CO_2 in air. The adventitious C 1s peak at 285.0 eV was removed with 1 minute of Ar ion sputtering. The Li 1s peak at 55.2 eV, the C 1s peak at 289.5 eV and the O 1s peak at 531.6 eV were attributed to the formation of Li_2CO_3 [50, 51]. The stoichiometry of sputtered LiOH and Li_2CO_3 films is summarized in Table 4.4.4. The uncertainty of these atomic percentages is <2%. In comparison, stoichiometric Li_2CO_3 has a composition of 33.3% lithium, 16.7% carbon and 50.0% oxygen. This excellent agreement argues that the Li_2CO_3 ALD film is close to stoichiometric Li_2CO_3. The slightly higher levels of carbon and decreased levels of oxygen in the Li_2CO_3 ALD

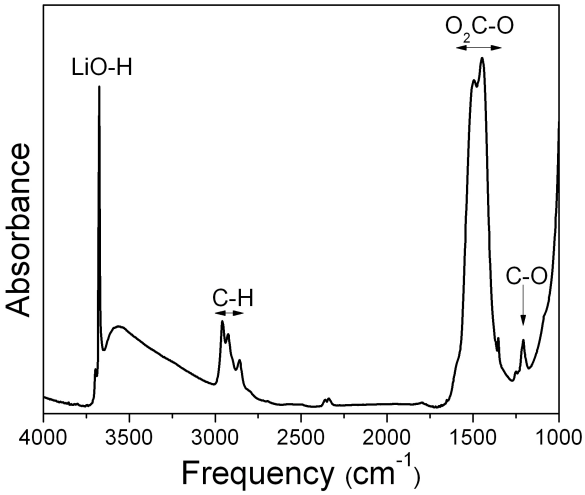

Figure 4.15: *In situ* FTIR spectrum of a LiOH ALD film grown using 100 cycles of LTB and H_2O at 225 C. The absorbance from O2C-O stretching vibrations indicates the presence of some Li_2CO_3 from reaction with CO_2.

films may result from some unreacted tert-butoxide groups.

Table 4.1: Atomic percentage of Li, C and O in Li_2CO_3. For comparison, the atomic percentage of stoichiometric Li_2CO_3 are also presented.

	Stoichiometric Li_2CO_3	Air Exposed ALD LiOH	ALD Li_2CO_3
Li	33.3%	30.7%	32.7%
C	16.7%	20.1%	19.0%
O	50.0%	49.3%	48.3

4.5 Conclusions

ALD techniques have been demonstrated for depositing LiOH and Li_2CO_3 using LTB, H_2O and CO_2 reactants. The QCM results illustrate the initial growth of LiOH with sequential LTB and H_2O exposures and reveal the very hygroscopic nature of LiOH. The reaction of LiOH with CO_2 is facile as observed by QCM and FTIR investigations. Li_2CO_3 ALD growth was also accomplished using sequential LTB, H_2O and CO_2 exposures. The identity of the Li_2CO_3 films was confirmed by FTIR and XPS investigations. LiOH and Li_2CO_3 ALD films may serve as artificial SEI layers to enhance the performance of graphite anodes in LIBs.

4.6 Acknowledgements

This study was supported by the DARPA Center on Nanoscale Science and Technology for Integrated Micro/Nano-Electromechanical Transducers (iMINT) funded by DARPA/MEMS S and T Fundamentals Program (HR0011-06-1-0048). Additional funding was contributed by the National Science Foundation (CHE-0715552). Some of the equipment used in this research was provided by the Air Force Office of Scientific Research.

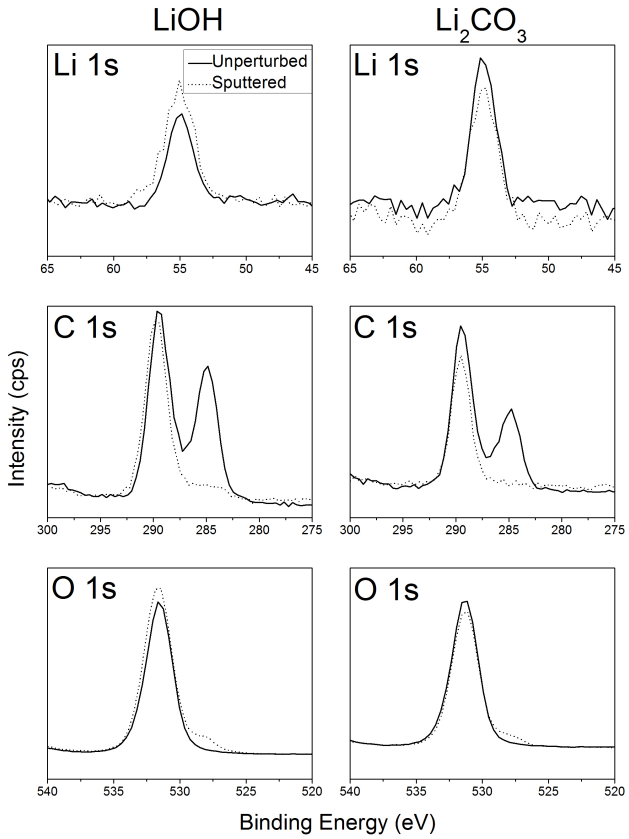

Figure 4.16: *Ex situ* XPS spectra of the of LiOH and Li_2CO_3.

Chapter 5

Enhanced Stability of $LiCoO_2$ Cathodes with thin films of Al_2O_3 Grown with Atomic Layer Deposition

5.1 Abstract

It has been widely demonstrated in the literature that metal oxide films grown with wet chemical techniques enhance the performance of LIBs. Films grown with wet chemical techniques typically have thicknesses with the range 50-1000 Å. Here we demonstrate that ultrathin films grown with atomic layer deposition (ALD) enhanced the capacity retention of $LiCoO_2$ in lithium-ion battery (LIB) half cells. Depending on the number of ALD cycles, the Al_2O_3 films grown on $LiCoO_2$ particles in this study had thickness in the range of 3-22 Å. Al_2O_3 coated $LiCoO_2$ particles had a capacity retention of 89% after 120 charge-discharge cycles, with respect to the third charge-discharge cycle, in the range of 3.3-4.5 V (versus Li/Li^+). Bare $LiCoO_2$ exhibited a capacity retention of only 45%. In addition to coating $LiCoO_2$ particles, Al_2O_3 ALD was coated on composite electrodes consisting of $LiCoO_2$ particles, acetylene black and poly(vinylidene fluoride). The improvements from the ultrathin Al_2O_3 films may stem from a variety of mechanisms including: minimizing the interactions between the $LiCoO_2$ and the electrolyte thereby reducing reactions between the two, Al_2O_3 may act as a sacrificial scrubber for HF, or the film may block the dissolution of Co ions. In addition to Al_2O_3, films of ZnO ALD on $LiCoO_2$ were also characterized. ZnO did enhance the performance of the $LiCoO_2$.

5.2 Introduction

The traditional means for producing energy, such as coal or hydroelectric, can be tuned to meet the power demand of the population being served. In contrast, most renewable energy sources, such as wind power or photovoltaics, have their production rate fixed by nature. With wind power and photovoltaics, peak production does not necessarily correlate with peak demand. Rather, peak production correlates with windiest or sunniest times of the day. In order to synchronize peak power production from renewable energy sources with peak demand from the population being served, an efficient and durable means of energy storage must be developed. Lithium ion batteries (LIBs) have emerged as a vital energy storage technology for portable electronics [185, 203, 209]. The high energy densities that make LIBs suitable for portable electronics may allow for the practical use of LIBs for power storage for the electric grid, hybrid electric vehicles or all-electric vehicles. In order to implement LIBs in vehicles or the power grid the durability of the LIBs must be dramatically improved.

Most LIBs employ $LiCoO_2$ as the cathode active material. $LiCoO_2$ has practical limitations that limit the voltage range over which it may be cycled. At voltages higher than ~4.2 V (versus Li/Li^+), Co can be dissolved from $LiCoO_2$, $LiCoO_2$ can react with the electrolyte and structural changes may occur in the $LiCoO_2$ [146]. These changes are detrimental to the $LiCoO_2$ and result in a decreased capacity of the LIB [146]. It has been demonstrated in the literature that these problems can be mitigated by coating the $LiCoO_2$ powders with metal oxides: Al_2O_3 [46, 45, 120], ZrO_2 [131, 106], ZnO [177], SiO_2 [13] and TiO_2 [132, 225]; metal fluorides: AlF_3 [228]; and metal phosphates: $AlPO_4$ [42, 122]. These films were typically deposited with wet chemical techniques such as the sol-gel method, followed by a heat treatment [44, 129, 47, 176, 45]. The typical thickness of these coatings is ~50-1000 Å [44, 129].

Atomic layer deposition (ALD) is a thin film growth technique where gas phase precursors react with the surface of the substrate [79, 161]. Because ALD uses sequential, self limiting surface reaction it is possible to grow conformal films on high aspect ratio structures with digital thickness

control [79, 161]. The precise control of film thickness, morphology and stoichiometry offered by ALD makes it an excellent choice for coating LIB active materials. Films grown by ALD have been employed in a variety of industries [103, 111, 138, 147, 152]; however, ALD has not been widely used to modify the surfaces of active materials for LIBs [172].

In this study ALD, rather then wet chemical techniques, ALD was used to grow metal oxide films on $LiCoO_2$. ALD does not use the large amount of solvents required for wet-chemical techniques and ALD allows for precise control of the amount of precursor used. In these two regards ALD can be seen as more environmentally benign than wet chemical techniques.

In this study, Al_2O_3 and ZnO films grown with ALD on $LiCoO_2$ are characterized. Films were grown both on the $LiCoO_2$ powders prior to electrode assembly and on assembled electrodes consisting of $LiCoO_2$, acetylene black (conductive additive) and poly(vinylidene fluoride) (polymer binder). The presence and conformality of the Al_2O_3 and ZnO were measured with X-ray photoelectron spectroscopy. The electrochemical performance for the coated, particle and electrodes, and bare $LiCoO_2$ was measured by cycling against Li metal. The effect of the thickness of the Al_2O_3 film on the electrochemical performance was evaluated.

5.3 Experimental

5.3.1 ALD on $LiCoO_2$ powders

The $LiCoO_2$ used in these experiments was obtained from LICO Technology (Tao-Yuan Hsien, Taiwan). The $LiCoO_2$ particle size (D_{50}) was 7-10 μm, as reported by the manufacturer. The manufactures grade for the $LiCoO_2$ was L106. For the Al_2O_3 ALD and ZnO ALD, $(Al(CH_3)_3$ (TMA, trimethylaluminum) (97%) and $Zn(C_2H_5)_2$ (DEZ, diethylzinc) were obtained from Sigma-Aldrich (St. Louis, MO). HPLC grade H_2O was also from Sigma-Aldrich and was further purified by 5 cycles of freeze-pump-thaw.

ALD on particles is possible using either fluid bed reactors [201, 200] or rotary reactors [139, 140]. A schematic of the rotary reactor used in this work is shown in Figure 5.1. In order

to perform ALD on powders, the powders were placed in a porous stainless steel cylinder (A). The porous stainless steel cylinder was placed in the chamber onto a magnetically coupled axel via an O-ring sealed door (B). A motor rotated the axel and porous stainless steel via a magnetically coupled rotary feed through (Transfer Engineering and Manufacturing, Inc., Fremont, CA)(C). This served to agitate the $LiCoO_2$ during the ALD process. A dual range, 0-10 and 0-100 Torr, Baratron capacitance manometer (MKS Instrument, Andover, MA)(D) was used to measure the pressure in the reaction chamber. Each reactant entered the reaction chamber through a series of pneumatic (E) and needle (F) valves that were attached to 0.25" welded ports on a custom 6.0" to 2.75" Conflat zero length reducer. In order to evacuate the chamber a gate (G) was opened to connect the reactor to an corrosion resistant dual-stage rotary vane pump (Alcatel Vacuum Technology, Annecy, France) (H). A ceramic heater (Watlow Electric Manufacturing Co., St. Louis, MO) (J) on the rotary reactor was employed to heat the reactor. The temperature was monitored with a thermocouple and was controlled via PID loop with a temperature controller (Eurotherm U.S.A., Ashburn, VA).

During the ALD process on particles the porous metal cylinder was rotated in the rotary reactor at ∼150 rpm. Given the diameter of the rotating porous cylinder, this rotational frequency is consistent with a centripetal force of ∼0.5g. Reasonable results were obtained using rotational frequencies from 140-180 rpm. Rotational frequencies <140 rpm led to less agitation and agglomeration during ALD.

Al_2O_3 ALD was performed on gram quantities of $LiCoO_2$ in the rotary reactor. The Al_2O_3 ALD surface chemistry employs $Al(CH_3)_3$ (trimethylaluminum, TMA) and H_2O as the reactants. The sequential, self-limiting reaction sequence during Al_2O_3 ALD is [58, 84, 149]:

A
$$AlOH^* + Al(CH_3)_3 \rightarrow AlO - Al(CH_3)_2^* + CH_4 \tag{5.1}$$

B
$$AlCH_3^* + H_2O \rightarrow Al - OH^* + CH_4 \tag{5.2}$$

where the asterisks denote surface species. The Al_2O_3 ALD reaction sequence was: (1) TMA dose to set pressure; (2) TMA reaction time; (3) evacuation of reaction products and excess TMA; (4)

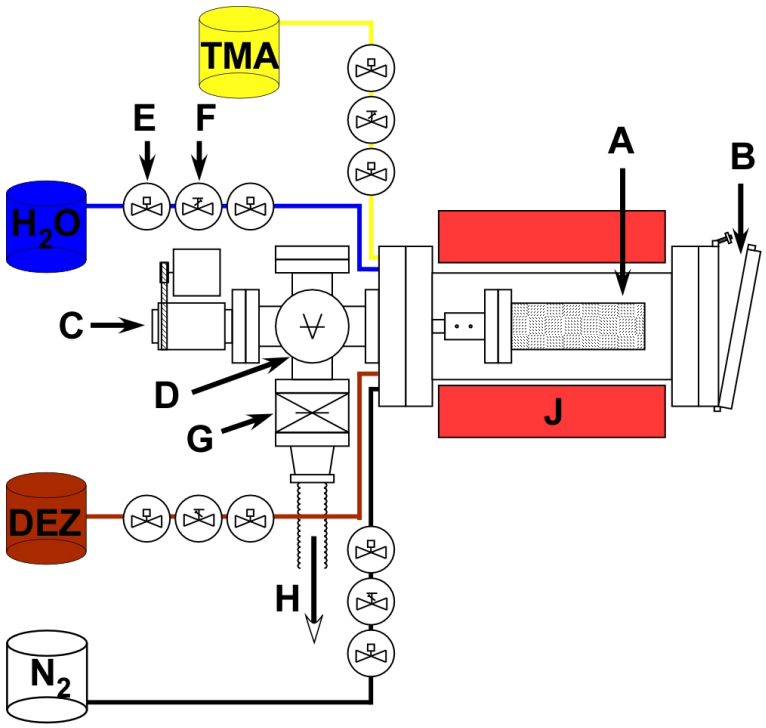

Figure 5.1: Schematic of rotary reactor used to coat gram quantities of $LiCoO_2$ powders.

N_2 dose; (5) N_2 static time; (6) evacuation of N_2 and any entrained gases; (7) H_2O dose to pressure, (8) H_2O reaction time; (9) evacuation of reaction products and excess H_2O; (10) dose N_2; (11) N_2 static time; and (12) evacuation of N_2 and any entrained gases. This sequence constituted one AB cycle of Al_2O_3 ALD. This reaction was carried out at 180 ℃.

The typical growth rate for Al_2O_3 ALD is 1.1-1.2 Å per ALD cycle [84, 149]. During the water dose a hydroxyl terminated surface is generated. The hydroxyl terminated surface will interact with excess H_2O in the reactor via hydrogen bonding. Due to the large surface area of the $LiCoO_2$ powders and the large surface area of the porous stainless steel cylinder, H_2O may not be completely purged from the reactor during the evacuation step of the H_2O dose. The presence of H_2O in the reactor during the TMA half reaction may lead increased growth per cycle. This behavior is similar to chemical vapor deposition [83, 139].

ZnO was also grown on $LiCoO_2$ powders with ALD. The sequential, self-limiting reaction sequence during ZnO ALD is [140, 211]:

A
$$ZnOH^* + Zn(CH_2CH_3)_2 \rightarrow ZnO - ZnCH_2CH_3^* + CH_3CH_3 \tag{5.3}$$

B
$$ZnCH_2CH_3^* + H_2O \rightarrow ZnOH^* + CH_3CH_3 \tag{5.4}$$

where the asterisks denote surface species. The ZnO ALD reaction sequence was: (1) DEZ dose to set pressure; (2) DEZ reaction time; (3) evacuation of reaction products and excess DEZ; (4) N_2 dose; (5) N_2 static time; (6) evacuation of N_2 and any entrained gases; (7) H_2O dose to pressure, (8) H_2O reaction time; (9) evacuation of reaction products and excess H_2O; (10) dose N_2; (11) N_2 static time; and (12) evacuation of N_2 and any entrained gases. This sequence constituted one AB cycle of ZnO ALD. This reaction was carried out at 180 ℃. The reported growth rate for ZnO ALD is 2.0 Å per ALD cycle [61]. In a similar fashion to the Al_2O_3 ALD chemistry, the presence of H_2O in the reactor during the DEZ half reaction may lead increased growth per cycle.

5.3.2 Materials Characterization

5.3.2.1 X-ray Photoelectron Spectroscopy

Characterization with X-ray photoelectron spectroscopy (XPS) was performed using a PHI 5600 X-ray photoelectron spectrometer with a monochromatic Al Kα source (1486.6 eV). The base pressure in the XPS analysis chamber was 3×10^{-10} Torr. XPS spectra were collected using the constant analyzer energy mode with a pass energy between 58.7-93.9 eV. The step size was varied between 0.25-0.4 eV. All spectra were calibrated to the adventitious carbon peak at 285 eV. An electron beam neutralizer was employed at 17.8 mA. Data was collected with Auger Scan (RBD Enterprises, Inc., Bend, OR). XPS data was analyzed in CASA XPS (Casa Software Ltd, UK). By monitoring the attenuation of the Co $2p_{3/2}$ peak with respect to the Al 2s peak as a function of the number of cycles of Al_2O_3 ALD it was possible to calculate the thickness of the Al_2O_3 film. Equation 5.5 shows the model used for calculating the thickness of an over layer oxide film with XPS [91, 53]. This model was derived for calculating the thickness of films on flat substrates [91, 53].

$$t = -\lambda \cos(\theta) \ln\left(1 + \frac{I_f/S_f}{I_s/S_s}\right) \tag{5.5}$$

The thickness of the over layer film (t) is measured as a function of the attenuation length for a photoelectron from the underlying substrate in the over layer film (λ), the angle of emission (θ), the peak area of the film (I_f) and substrate (I_s) and the relative sensitivity factors for the film (S_f) and substrate (S_s). Effective attenuation lengths were obtained from the NIST Electron-Effective-Attenuation-Length Database [154].

Powder samples for XPS were prepared by spreading $\sim$0.5 mm of the powder onto Ag foil and then pressing the powder into the malleable Ag film. Composite electrodes were also examined with XPS. For XPS on composite electrodes that had not undergone any charge-discharge cycles, the electrodes were examined as is. For electrodes that underwent charge-discharge cycling in a battery cell, the electrodes were rinsed with dimethyl carbonate to remove excess electrolyte prior to XPS analysis.

5.3.2.2 Electrical Conductivity

The electrical conductivity was measured by pressing a cylindrical pellet into a custom plastic mold equipped with four electrical contacts arranged in a cross around the cap of the cylinder. The measurement was carried out while the pellet inside the plastic mold was pressed to a pressure of 120 MPa. A current in the range of 0.5-5 μA was sourced between two adjacent electrical contacts and the potential was measured across the two remaining electrical contacts. The resistance was obtained from the slope of a five point voltage vs. current curve. The geometric factor was extracted by measuring the samples with different configuration. This technique for determining resistivity was pioneered by van der Pauw [193].

5.3.3 Electrochemical Characterization

In addition to $LiCoO_2$ the battery electrode consisted of a conductive additive, acetylene black (AB) and a polymer binder poly(vinylidine fluoride)(PVDF). AB and PVDF were obtained from Alfa Aesar (Ward Hill, MA). N-methyl pyrrolidinone from Sigma-Aldrich (St. Louis, MO) was used as the solvent to prepare the electrode material. The electrolyte, 1.0 M $LiPF_6$ dissolved in a solution of ethylene carbonate (EC):dimethylcarbonate (DMC) (1:1 by volume), was obtained from Novolyte (Cleveland, OH).

A slurry of $LiCoO_2$, AB and PVDF was prepared using N-methyl pyrrolidinone as the solvent. The weight ratio of electrode components was 83.0:7.5:9.5 ($LiCoO_2$:AB:PVDF). Cathodes were fabricated by spreading the slurry onto Al foil and evaporating the solvent. Lithium metal from Alfa Aesar (Ward Hill, MA) was employed as the counter electrode. The electrode diameters were 0.5". A polypropylene (PP)/polyethylene (PE) /polypropylene tri-layer film (Celgard, LLC, Charlotte, NC) was used as a separator between the Li metal and the cathode. The separator was porous with a thickness of $\sim$20 μm. Cells were fabricated using 2032-type coin cell in a glove box under an Ar environment (Vacuum Atmosphere's Inc., Amesbury, MA). The H_2O and O_2 concentrations in the glove box were typically under 0.1 and 0.5 ppm respectively.

Constant current charge-discharge cycling was performed in the range of 3.3-4.5 V versus Li/Li^+ using a galvanostat (Arbin Instrument, College Station, TX). The current density during the first two charge-discharge cycles was 0.1 C-rate (14 mA g^{-1}). For subsequent cycles the current density was 1 C-rate (140 mA g^{-1}).

Electrochemical impedance spectroscopy (EIS) was performed using a 1280C Solartron instrument (Solartron Analytical, Hampshire, United Kingdom). Spectra were collected at an amplitude of 5 V over the range of 20 kHz-5 mHz. Prior to EIS measurements, the cells were charged to 4.5 V at a current density of 0.1 C-rate. The cells were then rested for 6 hours in order to allow them to stabilize. EIS was recorded at the open circuit voltage of the cells. EIS measurements were modeled via an equivalent circuit with ZView software (version 3.2c, Scribner Associates, Southern Pines, NC).

5.4 Results and Discussion

5.4.1 Al_2O_3 ALD on $LiCoO_2$ Powders

Figure 5.2 shows X-ray photoelectron spectra for bare $LiCoO_2$ and for $LiCoO_2$ coated with 2,4,6,8 and 10 cycles of Al_2O_3 by ALD. The atomic fraction of Al and Co as a function of the number ALD cycles, as observed with XPS, is shown in Figure 5.3. The behavior depicted in Figure 5.3 is indicative of Frank-van der Merwe type growth (layer-by-layer) [10]. The rapid attenuation of the Co signal by the increased number of cycles of ALD Al_2O_3 indicates that the film is conformal. Using Equation 5.5 and the data in Figure 5.3 the growth rate was determined to be 2.2 Å per ALD cycle. This is depicted in Figure 5.4 where the atomic fraction of Al and Co are shown as a function of the Al_2O_3 film thickness. The solid lines are the fits from Equation 5.5. The growth rate for the Al_2O_3 ALD was larger than what is typically reported in the literature [84, 149]. This increased growth rate was attributed to the incomplete purging of H_2O during the Al_2O_3 ALD [139, 140].

The resistance of the bare and Al_2O_3 ALD coated $LiCoO_2$ powders was measured using the

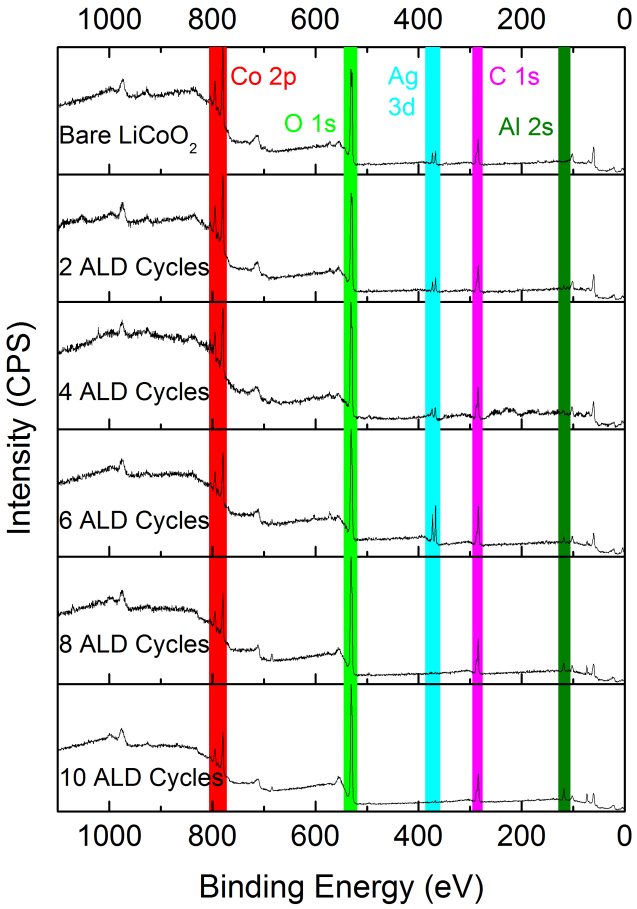

Figure 5.2: XPS spectra of bare and Al_2O_3 ALD coated $LiCoO_2$

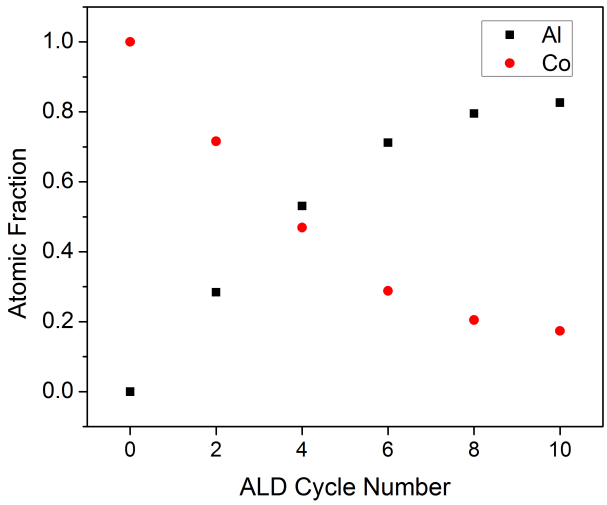

Figure 5.3: Atomic fraction of Al and Co for bare Al_2O_3 coated $LiCoO_2$ powders as a function of the number of cycles of ALD Al_2O_3.

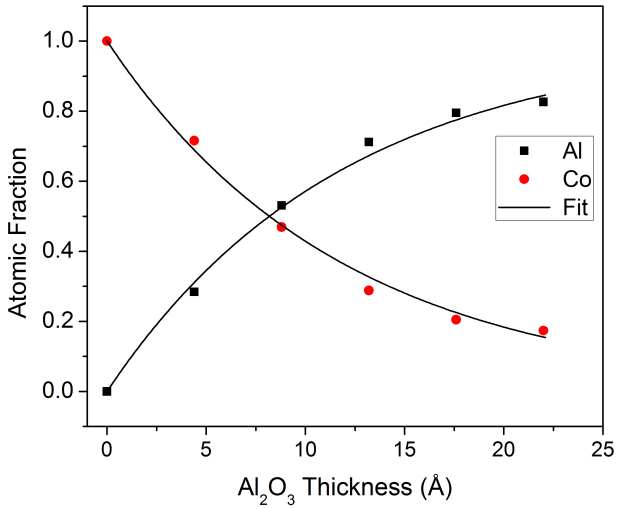

Figure 5.4: Atomic fraction of Al and Co for bare and Al_2O_3 coated $LiCoO_2$ powders as a function of the thickness of the ALD Al_2O_3 film. The solid lines are the fits from Equation 5.5.

van der Pauw method [193]. Figure 5.5 show the conductivity of the $LiCoO_2$ as a function of the number of cycles of Al_2O_3 ALD. Bare $LiCoO_2$ powder has a conductivity of 2×10^{-4} S cm^{-1}. The electronic conductivity was successively reduced by subsequent cycles of Al_2O_3 ALD. After 10 cycles ($\sim$ 22 Å) of Al_2O_3 ALD the electronic conductivity was 9.9×10^{-6} S cm^{-1}. The large increase in the resistance was attributed to the conformality of Al_2O_3 film and the numerous particle-to-particle contact resistances.

The specific discharge capacity as function of the number of Al_2O_3 ALD cycles for the third charge-discharge cycle is shown in Figure 5.6. The current density was 1 C-rate (140 mA g^{-1}). The capacity is unaffected for films as thick as 4 cycles of Al_2O_3 ALD ($\sim$8.8 Å). Beyond 4 cycles of Al_2O_3 ALD the capacity is dramatically reduced. By the tenth cycle of Al_2O_3 ALD the capacity for the third charge discharge cycle is only $\sim$20 mA g^{-1}. As the number of cycles Al_2O_3 ALD was increased the potential at which current began to flow during charging also increased. Similarly, during discharge, the potential dropped rapidly for $LiCoO_2$ with thicker Al_2O_3 ALD films. These overpotentials are attributed to the insulating nature of Al_2O_3 [83]. Figure 5.7 show the voltage profiles for the second and third charge-discharge cycle. Figure 5.7 (a) and (b) shows the second charge-discharge cycle at 0.1 C-rate. The overpotential is increased further when the current density was increased to 1 C-rate (Figure 5.7 (c) and (d)).

Discharge capacity as function of the number of charge-discharge cycles is shown in Figure 5.8. During the first two cycles the current density was 0.1 C-rate. After the first two cycles the current density was raised to 1 C-rate. The initial discharge capacity of the bare $LiCoO_2$ is similar to that of the $LiCoO_2$ with 2 cycles of Al_2O_3 ALD. For the $LiCoO_2$ with 6 cycles of Al_2O_3 ALD the initial discharge capacity was dramatically reduced when the current density is increased to 1 C-rate. For the $LiCoO_2$ with 10 cycles of Al_2O_3 ALD the initial discharge capacity it dramatically reduced even at 0.1 C-rate. The dramatic loss in capacity for the $LiCoO_2$ with 6 and 10 cycles of Al_2O_3 ALD was attributed to losses in the composite materials ability to conduct electrons and Li ions through the thicker Al_2O_3 films.

As compared with the bare $LiCoO_2$, the $LiCoO_2$ with 2 cycles of Al_2O_3 ALD was able retain

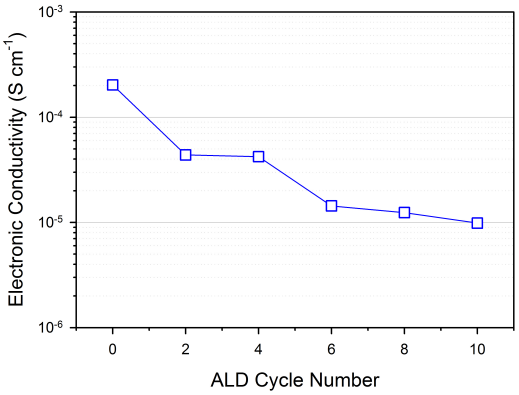

Figure 5.5: Electronic conductivity of bare and Al_2O_3 ALD coated $LiCoO_2$ powders.

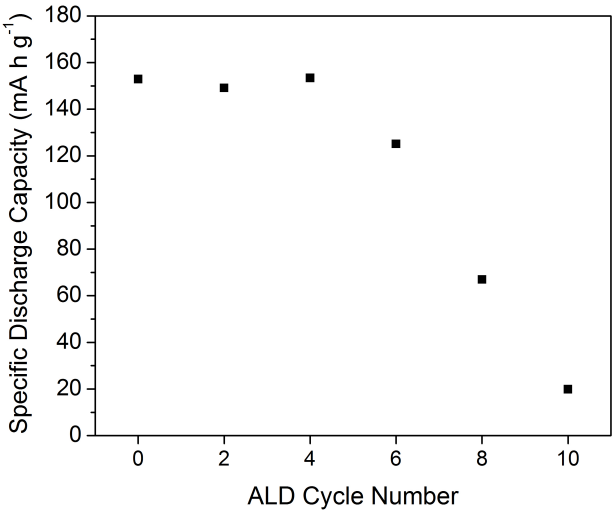

Figure 5.6: Specific discharge capacity as a function of the number of cycles of Al_2O_3 ALD.

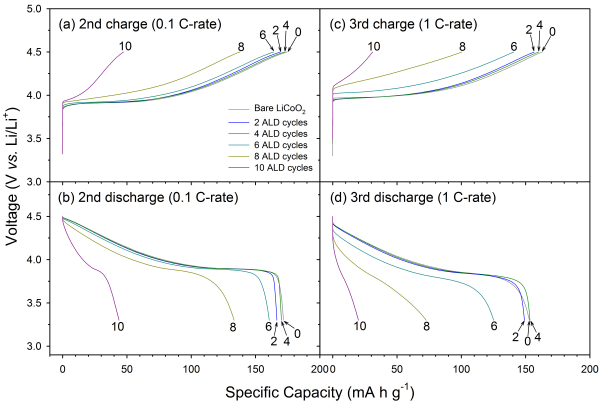

Figure 5.7: Voltage profiles for the second and third charge-discharge cycles for bare and Al_2O_3 ALD coated $LiCoO_2$ powders.

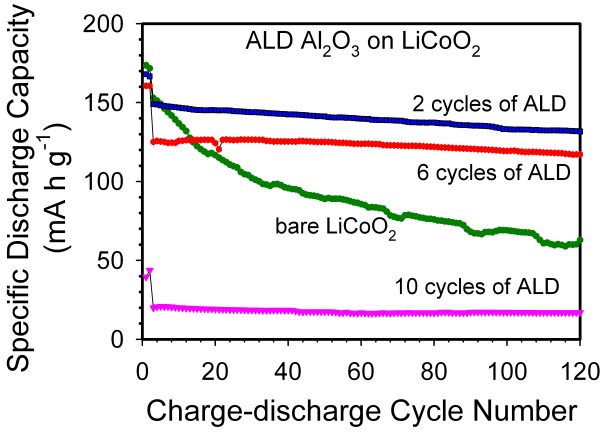

Figure 5.8: Discharge capacity as a function the number of charge-discharge cycles for bare $LiCoO_2$ and $LiCoO_2$ with 2,6 and 10 cycles of Al_2O_3 ALD.

its capacity with charge-discharge cycling. After 120 charge discharge cycles, the $LiCoO_2$ with 2 cycles of Al_2O_3 ALD had retained 89% of its initial capacity, with respect to the third charge-discharge cycle. In contrast, the bare $LiCoO_2$ had retained only 45% of its original capacity. The $LiCoO_2$ with 10 cycles of Al_2O_3 ALD showed excellent stability with charge-discharge cycling. However, since the material had lost most of it capacity due to the thicker ALD film the overall performance is not a practical improvement.

The voltage profiles for bare $LiCoO_2$ and $LiCoO_2$ with 2 cycles of Al_2O_3 ALD at the 3rd, 10th and 50th charge-discharge cycle are shown in Figure 5.9. For the bare $LiCoO_2$, as the number of charge-discharge cycles increased, the potential at which current began to flow during charging also increased. Similarly, during discharge, the more the cell had been charge-discharge cycled the greater the potential drop. These overpotentials may be attributed to the decomposition of the electrolyte on the $LiCoO_2$ or an electrochemical reaction between the $LiCoO_2$ and the electrolyte. From the voltage profile it is also evident that the capacity of the bare $LiCoO_2$ fades with the increasing number of charge-discharge cycles. In contrast to this behavior, the $LiCoO_2$ with 2 cycles of Al_2O_3 ALD appears relatively stable with respect both the development of an overpotential and capacity retention.

Figure 5.10 show the Nyquist plots, obtained from electrochemical impedance spectroscopy (EIS), of bare $LiCoO_2$ and $LiCoO_2$ with 2 cycles of Al_2O_3 ALD. A spectrum is shown for the bare and coated material at the 1st, 10th, 30th and 50 charge-discharge cycle. Z' (Ω g) is the is the magnitude of the real component of the impedance and Z" (Ω g) is the magnitude of the imaginary component of the impedance.

The Nyquist plots for the bare $LiCoO_2$ show the typical behavior for bare $LiCoO_2$ and consist of two semicircles in the high frequency regime followed by a 45 $^\circ$ line in the low frequency regime [127, 102, 166]. The higher frequency semicircle was attributed to the formation of a solid electrolyte interphase due to the decomposition of the electrolyte on the $LiCoO_2$ surface [127, 102, 166]. The lower frequency semicircle was attributed to the reactions at the $LiCoO_2$/electrolyte interface [127, 102, 166]. The 45 $^\circ$ line in the low frequency region is related to the diffusion of Li ion through

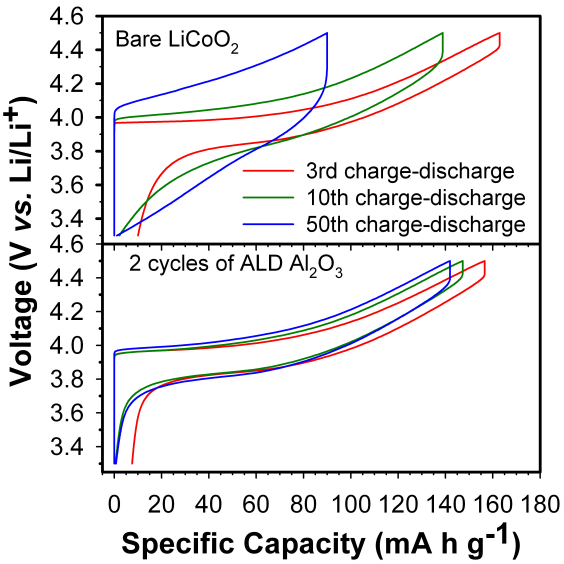

Figure 5.9: Voltage profiles for bare $LiCoO_2$ and $LiCoO_2$ coated with 2 cycles of Al_2O_3 ALD at the 3rd, 10th and 50th charge-discharge cycle.

the $LiCoO_2$ [102, 166]. Though the various features of the EIS spectra have been identified in the literature by modeling EIS data with equivalent circuits, it is important to note that equivalent circuits are a simple model for a far more complex structure. The key feature of Figure 5.10 is the evolution on the impedance as the LIB cell is cycled. For the bare $LiCoO_2$ the impedance increases with the number of charge-discharge cycles. The increase occurs for both for the real and imaginary components indicating increases in capacitance and resistance.

The Nyquist plots for the $LiCoO_2$ coated with 2 cycle of Al_2O_3 ALD are also shown in Figure 5.10. There are not two distinct semicircles in the high frequency region as was the case for the bare $LiCoO_2$. Instead there was one asymmetric semicircle. The 45° line in the low frequency region is initially similar to the bare $LiCoO_2$. The EIS spectra from the $LiCoO_2$ coated with 2 cycles of Al_2O_3 ALD do not evolve much with charge-discharge cycles. There is little indication of increases in either the real or imaginary component of the impedance. This electrode is exceptionally stable.

Nyquist plots can be model by determining an equivalent electrical circuit to account for all the elements in the LIB [136, 15, 126, 219]. For example, the circuit can contain capacitors to account for double layer capacitance at the active material surface or capacitance from films formed on the surface during chargee-discharge cycling. Resistors in the equivalent circuit may account for the resistance of the electrolyte, interparticle or particle-current-collector resistances, or resistance from films formed on the active material surface during chargee-discharge cycling. Wardberg impedance elements in the circuit may account for Li^+ diffusion. A LIB half cell is a complex structure with many evolving interfaces, accordingly it is conceivable to make ever increasingly complex equivalent circuits in order to achieve an accurate model of the LIB system. In this work a relatively simple circuit was used to model the Nyquist plots shown in Figure 5.10.

The Nyquist plots shown in figure 5.10 were modeled using the equivalent circuit shown in Figure 5.11 [145, 135, 14] with the ZView software package. R_{el} is the resistance of the electrolyte, R_f and C_f are the proposed resistance and capacitance of the film formed on the $LiCoO_2$ from the decomposition of the electrolyte during charge-discharge cycling, R_{ct} is the charge transfer resistance, C_{dl} is the double layer capacitance and constant phase element combined into a singe

element for ease of use in the ZView software, W is the Wardburg term for the diffusion of Li^+ in the bulk $LiCoO_2$. The impedance of C_{dl} and W take the forms shown in Equations 5.6 and 5.7 respectively [14].

$$Z_{C_{dl}} = \frac{1}{T(i\omega)^P} \tag{5.6}$$

$$Z_W = R\frac{\tanh{(it\omega)^p}}{(it\omega)^p} \tag{5.7}$$

C_{dl} has two fitting parameters, T and P. If P is 1 then C_{dl} is a capacitor with a capacitance of T. An inhomogeneous sample surface can cause P to deviate from 1 [135, 14], hence the need for constant phase element to model the rough surface of a LIB electrode. The Wardberg element also has to fitting parameters, t and p. The parameter t is proportional to the L^2/D where L is the depth into the $LiCoO_2$ particle and D is the effective diffusion coefficient of the Li^+ in the bulk $LiCoO_2$ particle [14]. Since the ALD coating should not effect the bulk properties of the $LiCoO_2$ the parameters W-t and W-p were fixed at 1 and 0.5 respectively as suggested by the Zview software. The modeled values of R_{el}, R_f, C_f, R_{ct}, C_{dl}-T and C_{dl}-P for bare and ALD coated $LiCoO_2$ are shown in Tables 5.1 and 5.2 respectively. The most apparent change with charge-discharge cycling is the increase in the R_{ct} from 81.4 Ω at the 1^{st} charge-discharge cycle to 1511 Ω at the 50^{th} charge-discharge cycle. For comparison, at the 1^{st} charge-discharge the ALD coated $LiCoO_2$ had a R_{ct} of 71.92 Ω and a R_{ct} of 138.6 Ω at the 50^{th} charge-discharge cycle. According to the model equivalent circuit shown in Figure 5.11 large increase in the R_{ct} is the cause of the overall increase in the impedance for the bare $LiCoO_2$.

Figures 5.8, 5.9 and 5.10 clearly illustrate that Al_2O_3 films on $LiCoO_2$ enhance the charge-discharge stability of the $LiCoO_2$. This phenomenon is not surprising as it has been documented in the literature that Al_2O_3 films can enhance $LiCoO_2$. Al_2O_3 may act as scavenger for HF. HF can be produced by reactions between trace amounts of contaminant H_2O and $LiPF_6$. The resultant HF can then act to dissolve Co from $LiCoO_2$ [88, 186, 229]. The dissolution of Co results in structural changes in the $LiCoO_2$ and degradation the LIBs capacity [146]. It has been reported that Al_2O_3 particles can be employed to sacrificially react with the HF to form stable insoluble

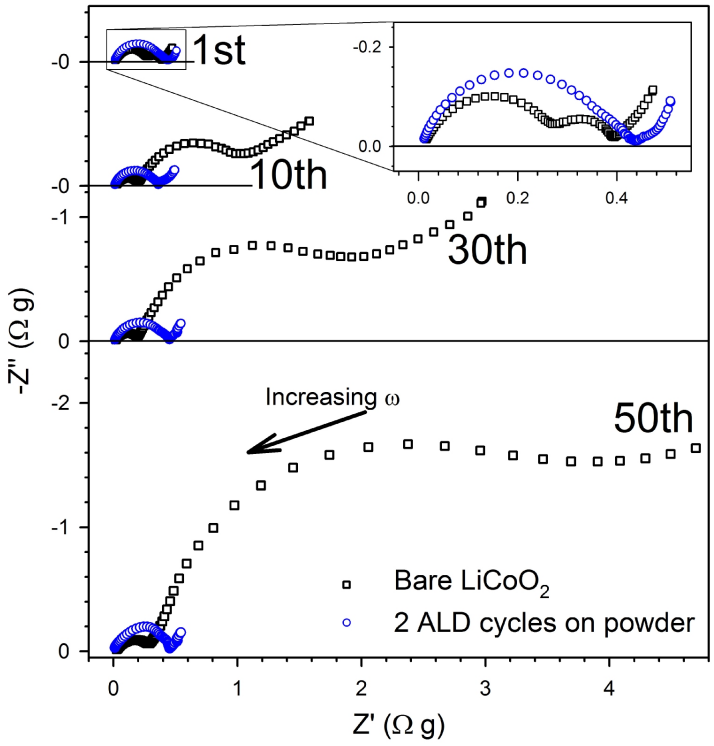

Figure 5.10: Impedance spectra for bare $LiCoO_2$ and $LiCoO_2$ coated with 2 cycle of Al_2O_3 ALD. The spectra were collected at the 1st, 10th, 30th and 50th charge-discharge cycle.

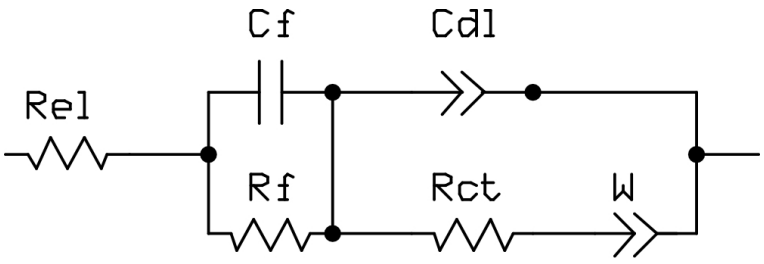

Figure 5.11: Equivalent circuit used to model EIS measurements.

Table 5.1: Modeled values of the parameter in the equivalent circuit shown in Figure 5.11 for the bare $LiCoO_2$ data shown in Figure 5.10.

Charge-discharge cycle number	R_{el} (Ω)	R_f (Ω)	C_f (F)	R_{ct} (Ω)	C_{dl}-T (F)	C_{dl}-P
1	3.01	40.21	5.36×10^{-6}	81.4	1.68×10^{-3}	0.39
10	8.59	38.79	3.26×10^{-6}	324.4	2.06×10^{-3}	0.66
30	6.73	41.00	3.96×10^{-6}	679.7	1.86×10^{-3}	0.73
50	10.01	60.02	3.91×10^{-6}	1511	1.70×10^{-3}	0.75

Table 5.2: Modeled values of the parameters in the equivalent circuit shown in Figure 5.11 for the ALD coated $LiCoO_2$ data shown in Figure 5.10.

Charge-discharge cycle number	R_{el} (Ω)	R_f (Ω)	C_f (F)	R_{ct} (Ω)	C_{dl}-T (F)	C_{dl}-P
1	0.56	52.73	5.22×10^{-6}	71.92	2.34×10^{-3}	0.59
10	1.27	43.72	7.17×10^{-6}	62.73	3.22×10^{-4}	0.57
30	0.93	31.94	1.33×10^{-5}	96.31	1.09×10^{-4}	0.66
50	0.75	63.46	1.32×10^{-5}	138.60	4.22×10^{-4}	0.44

compounds [133]. The Al_2O_3 film may suppress electrochemical reactions between the $LiCoO_2$ and the electrolyte by acting as a physical protection barrier [129, 76]. This protection barrier may prevent the dissolution of Co by the electrolyte [148]. It may also be possible that the Al_2O_3 is less reactive with the electrolyte then the $LiCoO_2$ surface. Al_2O_3 films on $LiCoO_2$ have also demonstrated enhanced electrical conductivity leading to superior battery performance [148].

Figure 5.12 shows XPS spectra of $LiCoO_2$ coated with 4 cycle of Al_2O_3 ALD, (a) before and (b) after 10 charge-discharge cycles. The region from 250-0 eV has been magnified 10×. As expected Al, C, Co, F and O are observed. P was observed in the electrode that had undergone charge-discharge cycling, Figure 5.12 (b). The presence of P is due to insufficient removal of excess $LiPF_6$, from the electrolyte, prior to XPS.

Prior to charge-discharge cycling the binding energy of the Al 2s peak was observed at 118.7 eV with a full width at half-maximum (fwhm) of 2.2 eV. After 10 charge-discharge cycles the Al 2s peak was broader, the fwhm was 2.8 eV, and shifted to a slightly higher binding energy, 119.2 eV. Literature values for the Al 2s binding energy in Al_2O_3, range from 116.25 eV [191] to 119.2 eV [27]. The Al 2s peak for AlF_3 has been observed at a binding energy of 121.0 eV [141]. The shift in the binding energy and the broadening of the fwhm for Al 2s peak after 10 charge-discharge cycles are indicative of the formation of AlF_3.

The Co $2p_{3/2}$ peak prior to charge-discharge cycling had a binding energy of 779.8 eV and a fwhm of 2.4. Literature values for the binding energy of the Co $2p_{3/2}$ peak in $LiCoO_2$ are similar, 780.1 eV [134]. After charge discharge cycling the Co $2p_{3/2}$ the binding energy remained similar at 279.7 eV. The fwhm had broadened to 2.9 eV and a high binding energy shoulded had begun to develop. The broadening at higher binding energy may be indicative of the presence of cobalt oxides [183].

5.4.1.1 Annealing Al_2O_3 Coated $LiCoO_2$

Thicker Al_2O_3 films reduce the electronic conductivity. It should be expected that thicker Al_2O_3 films should also reduce Li ion conductivity. It has been reported in the literature that

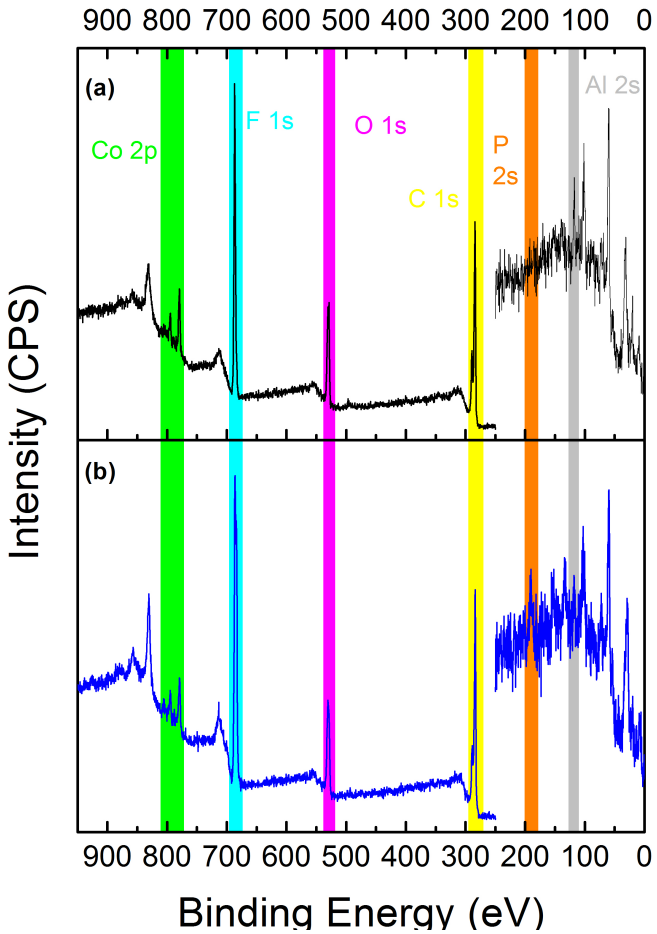

Figure 5.12: XPS spectra of $LiCoO_2$ coated with 4 cycle of Al_2O_3 ALD, (a) before and (b) after 10 charge-discharge cycles. The region from 250-0 eV has been magnified 10×.

Al_2O_3 films on $LiCoO_2$ results in an alloying of the Al_2O_3 and the $LiCoO_2$ to form $LiCo_{1-x}Al_xO_2$ on the surface of the $LiCoO_2$ [107, 108]. The $LiCo_{1-x}Al_xO_2$ is said to result in faster Li ion diffusion[107, 108]. It has also been demonstrated in the literature that Al_2O_3 films on $LiCoO_2$, followed by annealing, can lead to the migration of Al atoms into the $LiCoO_2$ resulting in an increased electronic conductivity of the composite material [148]. Considering that Al_2O_3 is an insulator and that any film should impede Li ion conduction it is surprising that thick (∼100-1000 Å) Al_2O_3 films result increased electron and Li ion conductivity [107, 108, 148].

For the wet chemical techniques used to produce Al_2O_3 films on $LiCoO_2$ annealing was part of the synthesis [107, 108, 148]. The annealing process can produce an alloy at the Al_2O_3-$LiCoO_2$ interface resulting in the production of $LiCo_{1-x}Al_xO_2$ [45, 115]. Conversely, it has been observed that sol-gel films of Al_2O_3 and SiO_2 on $LiCoO_2$ do show enhanced capacity retention when compared to untreated $LiCoO_2$ [39]. However, in this study the same effect was achieved with only the post sol-gel heat treatment and no Al_2O_3 or SiO_2 film.

For comparison, $LiCoO_2$ that had been coated with 20 cycles of Al_2O_3 ALD was subjected to an anneal at 450 ℃ for 10 hours in air. The unannealed $LiCoO_2$ had a discharge capacity of 8 mA h g^{-1} at 1 C-rate. Annealing the coated powder increased the discharge capacity to 15 mA h g^{-1}. While an improvement was observed for the annealed composite material, it was not close to the performance of bare $LiCoO_2$ at ∼160 mA h g^{-1}. In comparison to the much thicker Al_2O_3 films on $LiCoO_2$ that have already been studied [107, 108, 148], films grown with ALD are much more conformal. The inability for annealing to significantly improve the performance of the Al_2O_3 coated $LiCoO_2$ was attributed to the superior conformality of ALD. It is possible that for films grown with wet chemical techniques conduction pathways were maintained because the films were nonuniform and nonconformal.

5.4.2 ZnO ALD on $LiCoO_2$ Powders

Stoichiometric ZnO is an n-type semiconductor with carrier densities of $\sim 10^{16}$ cm^{-3} and resistivities of 0.1-1 Ω cm [96]. ZnO grown with ALD at elevated temperatures can have oxygen

deficiencies leading to lower resistivities[96]. The resistivity of ZnO grown with ALD has been reported as low as 8×10^{-3} Ω cm [63]. Similar enhancements to those of Al_2O_3 have been demonstrated for other metal oxide systems [39], including ZnO [67]. The enhancements are often independent of the metal oxide [39]. The HF scrubbing or physical protective properties of ZnO should be similar to Al_2O_3 [39]. However, the decreased resistivity of ZnO, with respect to Al_2O_3 ($\sim 10^{16}$ Ω cm [63]), makes it an interesting candidate to compare with Al_2O_3.

For comparison, 4 cycles of ZnO were deposited on $LiCoO_2$ with ALD. Figure 5.13 shows the charge-discharge voltage profiles at the 3rd, 10th and 50 charge-discharge cycle. This behavior is similar to the behavior of the bare $LiCoO_2$ shown in Figure 5.9. By the 10th charge-discharge cycle the electrode is showing a reduced capacity, the onset of current flow during charge is at a higher potential and the voltage drop during discharge is larger in comparison to the 3rd charge-discharge cycle. These problems are worse by the 50th charge-discharge cycle.

Figure 5.14 shows the discharge capacity as a function the number of charge-discharge cycles for $LiCoO_2$ with 4 cycles of ZnO ALD. For comparison the data shown in Figure 5.8 for bare $LiCoO_2$ and $LiCoO_2$ with 2 cycles of Al_2O_3 ALD has been added. The $LiCoO_2$ with 4 cycles of ZnO ALD shows similar stability to bare $LiCoO_2$, there is a dramatic loss in the capacity as the number of charge-discharge cycles is increased.

Figure 5.15 shows XPS spectra of $LiCoO_2$ coated with 4 cycle of ZnO ALD, (a) before and (b) after 10 charge-discharge cycles. As expected C, Co, F, O and Zn are observed. Prior to charge-discharge cycling the Zn 2p peak at a binding energy of $\sim$1021.6 eV is a dominant feature in Figure 5.15(a). After charge-discharge cycling the Zn 2p is practically gone. From the absence of the Zn 2p peak in Figure 5.15(b) it appears that under the conditions in the LIB during charge-discharge cycling that ZnO is not stable.

In order to quantify the relative stability of ZnO and Al_2O_3 high resolutions XPS scans were performed on the Zn 2p, Al 2s and Co 2p peaks, these are shown in Figure 5.16. Black lines show the peak before the 10 charge-discharge cycles, blue lines show the peak after the 10 charge-discharge cycles. It was assumed that Co dissolution was minimal during the 10 charge-discharge

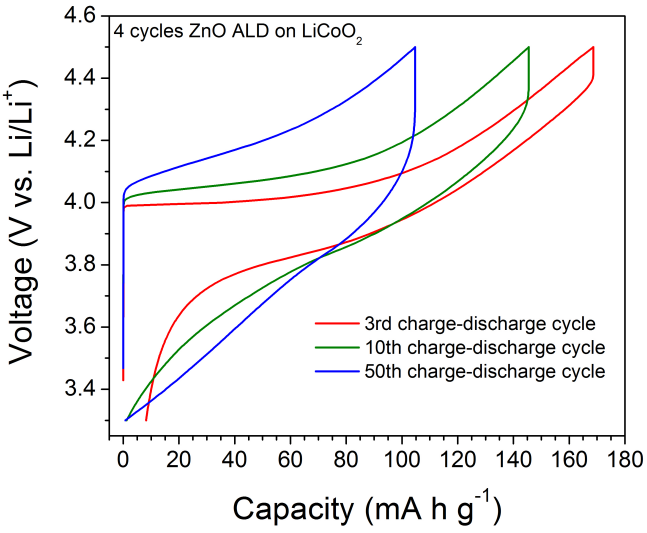

Figure 5.13: Voltage profiles for $LiCoO_2$ coated with 4 cycles of ZnO ALD at the 3rd, 10th and 50th charge-discharge cycle.

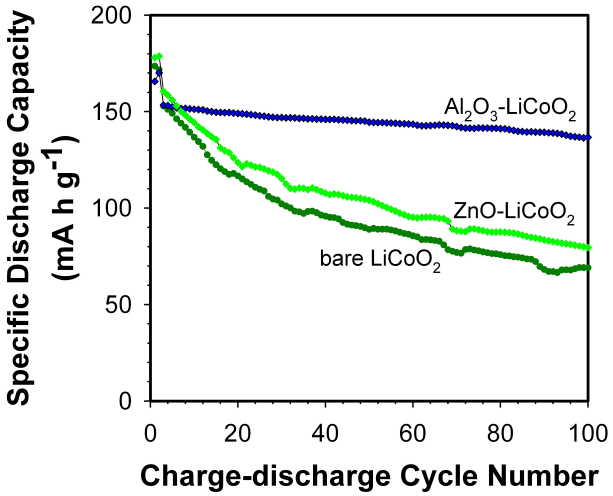

Figure 5.14: Discharge capacity as a function the number of charge-discharge cycles for bare $LiCoO_2$, $LiCoO_2$ with 2 cycles of Al_2O_3 ALD and $LiCoO_2$ with 4 cycles of ZnO ALD.

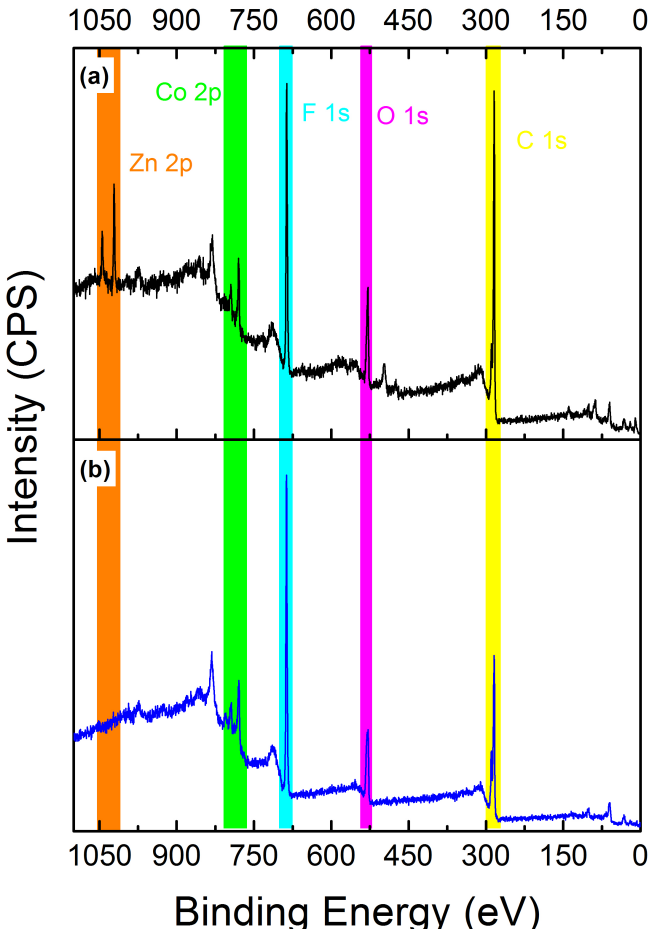

Figure 5.15: XPS spectra of bare $LiCoO_2$ and $LiCoO_2$ coated with 4 cycle of ZnO ALD, (a) before and (b) after 10 charge-discharge cycles.

cycles. For the $LiCoO_2$ coated with 4 cycle of Al_2O_3, the Co 2p peak intensities were normalized (Figure 5.16(a)) and the Al 2s peaks were scaled accordingly (Figure 5.16(b)). Similarly, for the $LiCoO_2$ coated with 4 cycle of ZnO, the Co 2p peak intensities were normalized (Figure 5.16(c)) and the Zn 2p peaks were scaled accordingly (Figure 5.16(d)).

From Figure 5.16(b) it appears that the intensities of the Al 2s peak are independent of whether the electrode was cycled. In contrast, Figure 5.16(d) illustrates that the amount of ZnO on the electrode is dramatically reduced with just 10 charge-discharge cycles. To examine this further the atomic fractions of the metal with respect to Co (M/(M + Co), where M = Al or Zn), were calculated from the XPS peak areas. The results are summarized in Table 5.3. Before charge-discharge cycling the atomic fraction of Al with respect to Co is 0.55, after cycling it is 0.53. While some Al_2O_3 may be converted to AlF_3 or a solid solution of $LiAl_xCo_{1-x}O_2$, overall Al is stable in the electrochemical cell. In contrast, prior to charge-discharge cycling, the atomic fraction of Zn with respect to Co was 0.49. After just 10 charge-discharge cycles the atomic fraction was 0.01. The ZnO and any Zn containing products from electrochemical reactions in the LIB are not stable and do not remain on the $LiCoO_2$ surface. It is possible that the Zn diffuses far enough into the $LiCoO_2$ to produce a diminished XPS signal or that the Zn is dissolved away in the electrolyte.

Table 5.3: The atomic fraction of Al and Zn, calculated from XPS, with respect to Co before and after 10 charge-discharge cycles.

Atomic Fraction	Before Cycling	After Cycling
Al	0.55	0.53
Zn	0.49	0.01

5.4.3 ALD Films on Composite Electrodes

ALD has been grown on a variety of porous substrates including aerogels [26], photonic crystals [109] and high aspect ratio trench structures [64]. A composite LIB electrode consisting of an assembly of particles held together with a polymer binder can be consider a porous substrate.

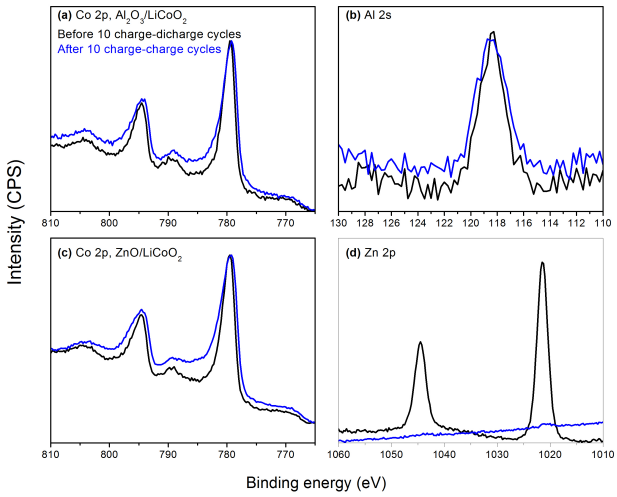

Figure 5.16: High resolution XPS spectra of $LiCoO_2$ coated with 4 cycle of Al_2O_3 ALD (a) the Co 2p peak before (black line) and after (blue line) 10 charge-discharge cycles and (b) the Al 2s peak before (black line) and after (blue line) 10 charge-discharge cycles. High resolution XPS spectra of $LiCoO_2$ coated with 4 cycle of ZnO ALD (c) the Co 2p peak before (black line) and after (blue line) 10 charge-discharge cycles and (d) the Zn 2p peak before (black line) and after (blue line) 10 charge-discharge cycles.

Given sufficient time the ALD precursors will be able to diffuse through the tortuous paths in between the particles and uniformly coat the $LiCoO_2$. Furthermore, where the $LiCoO_2$ surface is inaccessible due to PVDF coating, it may be possible for the ALD precursors to diffuse through the PVDF film and reach the $LiCoO_2$ surface [207]. The key differences between coating the particles prior to electrode assembly and coating the assembled electrode are: 1) coating not only the $LiCoO_2$ but also possibly coating the AB and the PVDF that are present in the assembled electrode; 2) the contact points at particle-particle, particle-current collector and particle-AB contacts will not be coated. Issue 2 may offer to improve the electrode electrical conductivity.

Figure 5.17 shows the discharge capacity as a function of the number of charge-discharge cycles for electrodes fabricated from bare $LiCoO_2$. One electrode was subsequently coated with 2 cycles of Al_2O_3 ALD prior to cycling. Coating the composite electrode, as compared with leaving it bare, showed a dramatic improvement in the discharge capacity retention. For the coated electrode the capacity retention after 120 charge-discharge cycles was 78%, with respect to the third charge discharge cycle. This is not as good of an improvement when compared with the $LiCoO_2$ that was coated with 2 cycles of Al_2O_3 ALD prior electrode assembly, Figure 5.8. The positive result as compared with the bare electrode is a strong indicator that the Al_2O_3 ALD was able to grow on the $LiCoO_2$ in the fabricated electrode.

Figure 5.18 shows the charge-discharge voltage profile for bare $LiCoO_2$, $LiCoO_2$ that was coated with 20 cycles of Al_2O_3 ALD prior to electrode fabrication (powder coated), and a $LiCoO_2$ electrode that was coated with 20 cycles of Al_2O_3 ALD (electrode coated). Figure 5.8 show that 10 cycles of Al_2O_3 ALD on $LiCoO_2$ powder is too thick and has s detrimental effect on the electrode performance. In this experiment 20 cycles of Al_2O_3 ALD was used to amplify the effect of coating the powder versus the electrode. For the Al_2O_3 ALD coated $LiCoO_2$ the potentials at which the current started to flow was greater than for the bare $LiCoO_2$. The powder coated $LiCoO_2$ had a larger overpotential (a) than electrode coated $LiCoO_2$ (b). The difference in the overpotentials between the powder coated $LiCoO_2$ and the electrode coated $LiCoO_2$ may be from the lack of an interparticle and particle-current-collector conduction pathway due to the conformality of the

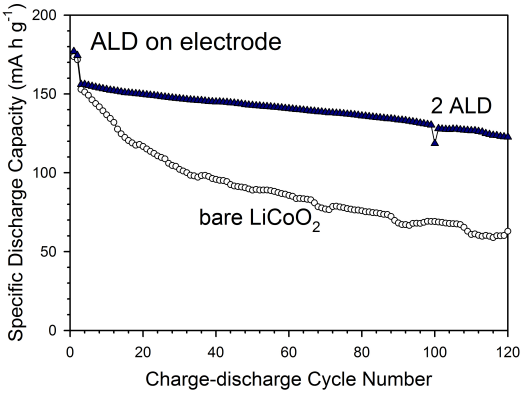

Figure 5.17: Discharge capacity as a function of the number of charge-discharge cycles for electrodes fabricated from bare $LiCoO_2$. One electrode was left bare the second electrode was coated with 2 cycles of Al_2O_3 ALD prior to cell cycling.

Al_2O_3 ALD film on the $LiCoO_2$. The Al_2O_3 ALD film on the $LiCoO_2$ electrode may preserve electron conduction pathways. A schematic of the possible conduction pathways is shown in Table 5.4.

5.4.4 Discussion

Both Al_2O_3 [44, 39] and ZnO [67], grown with wet chemical techniques, have been demonstrated to enhance the capacity retention of $LiCoO_2$. It is surprising that thick Al_2O_3 films grown with wet chemical techniques [44, 39] could be successfully scaled down with ALD, and ZnO films [67] could not. It is possible the mechanisms by which the films enhance $LiCoO_2$ may be different. ZnO may be consumed as an HF scavenger during charge-discharge cycling and as such more ZnO may be required to enhance the LIB performance, while Al_2O_3 may serve as a protective barrier blocking interactions between the $LiCoO_2$ and the electrolyte.

5.4.4.1 The Importance of Thin Films

Currently the majority of the mass in LIBs designed for automobiles is in the packaging [195]. This is an important consideration when adding a new component, a protective coating, to LIBs. Protective coatings add mass at the cost of the specific energy density. Thin films of Al_2O_3 clearly enhance the capacity retention of $LiCoO_2$. To achieve similar results as those presented here, films deposited with wet chemical techniques are much thicker and less conformal [44]. Thick protective films will become a large component of the mass as LIB active materials are scaled from micron size particles to nanoparticles [167].

The mass fraction (MF) of a protective Al_2O_3 film is given by Equation 5.8, where t is the Al_2O_3 thickness, ρ_f is the Al_2O_3 ALD density, r is the $LiCoO_2$ particle radius, and ρ_p is the $LiCoO_2$ density. The density of Al_2O_3 ALD is ~79% of bulk Al_2O_3 [18]. The density of bulk Al_2O_3 is 3.98 g cm^{-3} [202]. The density of $LiCoO_2$ is ~4.9 g cm^{-3} [192].

$$MF = \frac{t\left(3r^2 + 3rt + t^2\right)\rho_f}{t\left(3r^2 + 3rt + t^2\right)\rho_f + r^3\rho_p} \tag{5.8}$$

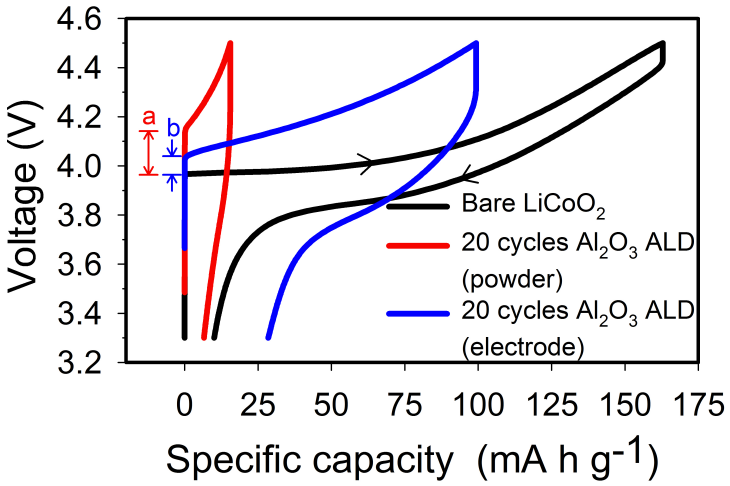

Figure 5.18: Charge-discharge voltage profile for bare $LiCoO_2$, $LiCoO_2$ that was coated with 20 cycles of Al_2O_3 ALD prior to electrode fabrication (powder coated), and a $LiCoO_2$ electrode that was coated with 20 cycles of Al_2O_3 ALD (electrode coated).

Table 5.5 shows the mass fraction for various sizes of $LiCoO_2$ particles with varying thickness of Al_2O_3 films. For a large particle (10 μm) a "thick" (100 nm) Al_2O_3 film contributes 1.9% of the composite mass. This is a significant contribution considering that the active materials are the only portion of the LIB that stores energy and they are already only a fraction of the total mass of the LIB. More importantly, on a 100 nm $LiCoO_2$ particle a "thick" (100 nm) Al_2O_3 film contributes 81.8% of the composite mass. It is impractical to have the majority of the mass of the active material be a protective coating as this dramatically reduces the specific energy density of the active material. In contrast a 0.2 nm Al_2O_3 ALD film on a 100 nm $LiCoO_2$ particle contributes only 0.4% of the composite mass. By keeping the mass fraction of the protective Al_2O_3 lower it will be possible to make lighter, higher energy density LIBs.

5.4.4.2 Advantages of ALD

ALD provides a solvent free method to coat LIB active materials. The efficiency of an ALD process can be tuned to ensure that very little precursor is wasted. The lack of a solvent and the efficiency of ALD processes may make them more environmentally benign than wet chemical techniques.

ALD offers a wealth of chemistries. Many of the chemistries demonstrated by wet chemical techniques to enhance LIB such as ZrO_2 [131], SiO_2 [13] and TiO_2 [132] can also be grown by ALD: ZrO_2 [118], SiO_2 [31] and TiO_2 [71]. It should be possible to follow the wet chemistry LIB literature employing and developing ALD processes to further enhance LIBs.

By employing multiple ALD chemistries it is possible to grow composites or nanolaminates (superlattices) these materials may have applications as protective films for LIBs. ALD chemistries can be combined to tune specific properties. For example the conductivity of ZnO can be tuned by alternating ALD cycles of Al_2O_3 [63]. It may be similarly possible to tune the stability a ZnO film in an electrochemical cell by the introduction of Al_2O_3.

Molecular layer deposition (MLD) is analogous to ALD in that it is a self-limiting, gas phase thin film growth technique that relies on sequential gas-surface reactions [80]. However, instead

of depositing a monolayer of atoms, a bifunctional monolayer of molecules is deposited. MLD can be employed to grow organic and hybrid organic-inorganic thin films [80]. MLD films may be grown to form solid state electrolytes with structures similar to polyethylene oxide [52] using TMA and ethylene glycol [55]. MLD films allow for the tuning of the mechanical properties of a hybrid organic-inorganic [143]. Compliant, i.e. low Young's modulus, films may aid in protecting high volume expansion active materials [160].

It is not possible to coat assembled electrodes with wet chemical techniques. ALD has the advantage of being able to conformally coat tortuous high aspect ratio structures of almost any shape [64, 26, 109]. This attribute makes it well suited for coating composite electrodes. It has be demonstrated that Al_2O_3 ALD on MoO_3 electrodes can assist in maintaining electrical contact between the MoO_3 particles and the conductive additive [160]. This effect was not observed when the MoO_3 particles were coated prior to electrode fabrication [160].

5.5 Conclusions

Al_2O_3 ALD films were grown on $LiCoO_2$ powders and on fabricated electrodes comprised of $LiCoO_2$. In both cases the Al_2O_3 ALD films enhanced the capacity retention of the $LiCoO_2$. With respect to the third charge-discharge cycle, $LiCoO_2$ coated with 2 cycles of Al_2O_3 ALD had a capacity retention of 89% after the 120 charge-discharge cycles, while the coated electrode had a capacity retention of 78% after the 120 charge-discharge cycles. The stability of the coated $LiCoO_2$ is remarkable because the cells were cycled beyond 4.2 V, the upper limit for suppressing Co dissolution. Bare $LiCoO_2$ powders only maintained 45% of the initial capacity after the 120 charge-discharge cycles. Thin films of ZnO ALD did not exhibit any improvements. Though XPS confirmed the presence of ZnO prior to charge-discharge cycling, the ZnO was present only in trace amounts after 10 charge-discharge cycles. The fact that thick films of ZnO deposited with wet chemical techniques improve the performance of $LiCoO_2$, while thin films do not improve the performance, is crucial to elucidating the mechanisms for the enhancement. The mechanisms for the enhancements observed from Al_2O_3 ALD films on $LiCoO_2$ may include acting as a physical

barrier to block interactions between the $LiCoO_2$ and the electrolyte, altering the $LiCoO_2$ surface chemistry to change the interactions between the $LiCoO_2$ and the electrolyte, acting as an HF scrubber, and preventing Co dissolution.

5.5.1 A Note on Significance

The material used in this study was commercial grade $LiCoO_2$. It must be emphasized that the cycling the cells beyond 4.2 V dramatically reduces the cell lifetime. In order to realize the performance enhancement offered by the ALD films it was necessary to employ these harsh condition to accelerate cell testing. It is believed that the enhancements in LIB performance from the ALD films will translate to LIB cells that are cycled under normal conditions.

5.6 Acknowledgements

This work was funded by a DOE SBIR subcontract from a grant to ALD NanoSolutions, Inc. (Broomfield, CO). Mr. Andrew S. Cavanagh received additional support from the DARPA Center on NanoscaleScience and Technology for Integrated Micro/Nano-Electromechanical Transducers (iMINT). Dr. Yoon Seok Jung also acknowledges a Korea Research Foundation Grant.

Table 5.4: Electron conduction pathways for bare $LiCoO_2$, ALD on $LiCoO_2$ powder and ALD on assembled $LiCoO_2$ electrode.

	Surface Protection	Conduction Pathway	
Bare	Poor	Poor	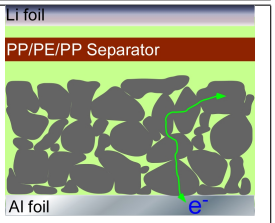
ALD on powder	**Good**	Poor	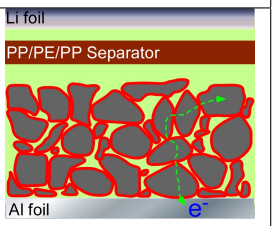
ALD on electrode	**Good**	**Good**	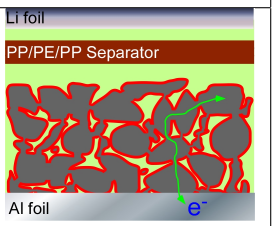

Table 5.5: Mass fraction of a protective Al_2O_3 film on $LiCoO_2$. The $LiCoO_2$ particle sizes are 10 μm, 1 μm and 100 nm. The Al_2O_3 film thicknesses are 0.2, 1, 10 and 100 nm.

Particle Size	Al_2O_3 Thickness (nm)	Mass fraction %
10 μm	0.2	trace
	1	0.02
	10	0.2
	100	1.9
1 μm	.2	.06
	1	0.2
	10	1.9
	100	17.5
100 nm	0.2	0.4
	1	1.9
	10	17.5
	100	81.8

Chapter 6

Enhanced Performance and Stability of Natural Graphite Andodes with thin films of Al_2O_3 Grown with Atomic Layer Deposition

6.1 Abstract

It has been demonstrated in the literature that metal oxide films grown with wet chemical techniques enhance the performance of LIBs. Films grown with wet chemical techniques typically have thicknesses with the range 50-1000 Å. Here we demonstrate that ultrathin films grown with atomic layer deposition (ALD) enhanced the capacity retention of natural graphite (NG) in lithium-ion battery (LIB) half cells and full cells. With respect to the third charge-discharge cycle, NG electrodes coated with 5 cycles of Al_2O_3 ALD had a capacity retention of 102% (no NO_2/TMA pretreatment) and 103% (with NO_2/TMA pretreatment) after 200 charge-discharge cycles at room temperature. At 50 ℃ the NG electrodes coated with 5 cycles of Al_2O_3 ALD had a capacity retention of 93% (no NO_2/TMA pretreatment) and 96% (with NO_2/TMA pretreatment) after 200 charge-discharge cycles. Bare NG electrodes had a capacity retention of 80% at room temperature and 26% at 50 ℃ after 200 charge-discharge cycles.

6.2 Introduction

Lithium ion batteries (LIBs) are in demand for portable electronics [11]. In order to realize LIB in high-power and high-energy density systems such as hybrid electric vehicles (HEVs), new materials must be developed that can accommodate the extreme conditions that come with high-power and high-energy density systems [2]. With its high reversible capacity (372 mA h g^{-1},

assuming a stoichiometry of LiC_2), low cost, moderate volume change, and low and flat voltage range, natural graphite (NG) is a promising anode material [217, 77, 165]. NG suffers from its incompatibility with propylene carbonate (PC) electrolyte and the instability of the solid electrolyte interphase (SEI).

Due to its low melting point (-49 ℃) PC based electrolytes are essential to operating LIBs in low temperature conditions [217]. Meeting low temperature requirement is essential to using LIBs in HEVs in cold weather environments. For comparison the melting points of EC and DMC are 35-38 ℃ and 2-4 ℃ respectively [169]. Graphite electrodes are exfoliated by PC electrolytes [217, 16]. The exfoliation exposes fresh graphite surfaces which require further electrolyte decomposition to form SEI on the freshly exposed surfaces [217, 16]. The exfoliation process also fractures the graphite particle which reduces the conductivity of the electrode due to the disconnects at the fracture sites [16]. This results in irreversible loss of capacity and a low coulombic efficiency [217]. Furthermore, a reaction byproduct of the decomposition of PC is propylene gas [57, 217]. Propylene gas can be explosive [169].

Thermal vapor deposition has been employed to coat protective carbon films onto NG to prevent interactions between the NG on the PC electrolyte [218, 217, 198]. Increasing the thickness of the protective carbon film increased the battery performance. For example, Yoshio *et al.* observed that a NG coated with an 8.6 weight % protective carbon coating had a coulombic efficiency on the first charge-discharge of 75.8% [218]. The coulombic efficiency was increased to 92.5% by essentially doubling the weight % of the protective carbon coating to 17.6% [218]. These two experiments used an electrolyte that was only 20% PC (PC:DMC, 1:4 by volume) [218]. If the concentration of the PC in the electrolyte was increased the battery performance suffered. The first cycle coulombic efficiency for a 17.6 weight % protective carbon film in an electrolyte that was 33% PC (PC:DMC, 1:2 by volume) was only 71.0% [218]. This is a dramatic reduction in the first cycle coulombic efficiency, 92.5% $\rightarrow$ 71.0%, with only a 13% increase in the concentration of the PC in the electrolyte, 20% $\rightarrow$ 33% [218]. Furthermore, the weight % of protective carbon film used in this study, and others, are a significant portion of the mass of the active material

[218, 217, 198, 197, 119].

Efforts have been made to modify the surface of NG with metal oxides to control the behavior of the SEI. Irreversible capacity loss occurs mainly due to the reductive decomposition of the organic electrolytes to form a SEI on the graphite surface [150, 151, 123, 220]. Al_2O_3 [104], ZrO_2 [117, 116] and $AlPO_4$ [123] films deposited with sol gel methods have displayed good capacity retention and high coulombic efficiency at the first cycle. Decomposition of the SEI at elevated temperatures is exothermic and can lead to catastrophic battery failure [21, 212, 59].

Sol-gel methods require large amounts of solvents and post coating heat treatments. Also, sol-gel methods can only apply films to powders as opposed to depositing a film on an assembled electrode. In this study atomic layer deposition (ALD) was used to deposit thin conformal films of Al_2O_3 on NG powders and electrodes assembled from NG. The electrodes were electrochemically characterized by charge-discharge cycling against Li metal and $LiCoO_2$. ALD does not use the large amount of solvents required for wet-chemical techniques and with ALD the amount of precursor used can be precisely controlled. In these two regards ALD can be seen as more environmentally benign then wet chemical techniques. ALD coated electrodes

6.3 Experimental

6.3.1 Al_2O_3 ALD on Powders

The natural graphite (NG) used in these experiments was obtained from Asbury Graphite Mills Inc. (Asbury, NJ), manufacture's product number HPM850. The NG particle size was $\sim$4 μm. The NG density was 2.6 g cm^{-3}. The NG conductivity was 11.4 S cm^{-1}. All specifications for the NG were as reported by the manufacturer. For the Al_2O_3 ALD trimethylaluminum (TMA, $Al(CH_3)_3$) (97%) was obtained from Sigma-Aldrich (St. Louis, MO). HPLC (high pressure liquid chromatography) grade H_2O was also from obtained from Sigma-Aldrich and was further purified by 5 cycles of freeze-pump-thaw. For the NO_2/TMA nucleation pretreatment, commercial purity grade NO_2 (99.5%) was acquired from Airgas.

ALD on particles is possible using either fluid bed reactors [201, 200] or rotary reactors [139, 140]. A schematic of the rotary reactor used in this work is shown in Figure 6.1. In order to perform ALD on powders, the powders were placed in a porous stainless steel cylinder (A). The porous stainless steel cylinder was placed in the chamber onto a magnetically coupled axel via an O-ring sealed door (B). A motor rotated the axel and porous stainless steel via a magnetically coupled rotary feed through (Transfer Engineering and Manufacturing, Inc., Fremont, CA)(C). This served to agitate the $LiCoO_2$ during the ALD process. A dual range, 0-10 and 0-100 Torr, Baratron capacitance manometer (MKS Instrument, Andover, MA)(D) was used to measure the pressure in the reaction chamber. Each reactant entered the reaction chamber through a series of pneumatic (E) and needle (F) valves that were attached to 0.25" welded ports on a custom 6.0" to 2.75" Conflat zero length reducer. In order to evacuate the chamber a gate (G) was opened to connect the reactor to an corrosion resistant dual-stage rotary vane pump (Alcatel Vacuum Technology, Annecy, France) (H). A ceramic heater (Watlow Electric Manufacturing Co., St. Louis, MO) (J) on the rotary reactor was employed to heat the reactor. The temperature was monitored with a thermocouple and was controlled via PID loop with a temperature controller (Eurotherm U.S.A., Ashburn, VA).

During the ALD process on particles the porous metal cylinder was rotated in the rotary reactor at ∼150 rpm. Given the diameter of the rotating porous cylinder, this rotational frequency is consistent with a centripetal force of ∼0.5 g. Reasonable results were obtained using rotational frequencies from 140-180 rpm. Rotational frequencies <140 rpm led to less agitation and agglomeration during ALD.

Al_2O_3 ALD was performed on gram quantities of NG in the rotary reactor. The Al_2O_3 ALD surface chemistry employs TMA and H_2O as the reactants. The sequential, self-limiting reaction sequence during Al_2O_3 ALD is [58, 84, 149]:

A
$$AlOH^* + Al(CH_3)_3 \rightarrow AlO - Al(CH_3)_2^* + CH_4 \quad (6.1)$$

B
$$AlCH_3^* + H_2O \rightarrow Al - OH^* + CH_4 \quad (6.2)$$

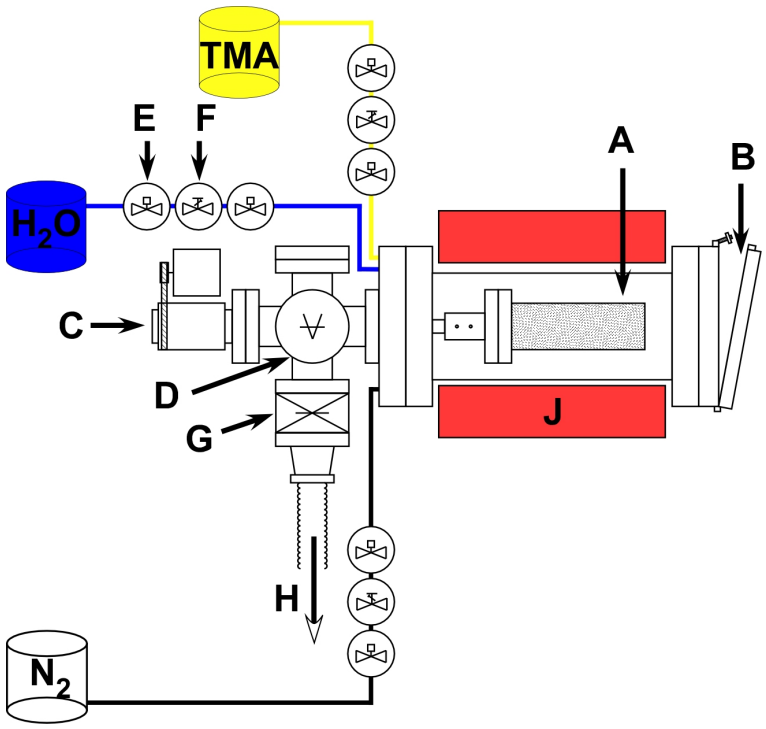

Figure 6.1: Schematic of rotary reactor used to coat gram quantities of $LiCoO_2$ powders.

where the asterisks denote surface species. The Al_2O_3 ALD reaction sequence was: (1) TMA dose to set pressure; (2) TMA reaction time; (3) evacuation of reaction products and excess TMA; (4) N_2 dose; (5) N_2 static time; (6) evacuation of N_2 and any entrained gases; (7) H_2O dose to pressure, (8) H_2O reaction time; (9) evacuation of reaction products and excess H_2O; (10) dose N_2; (11) N_2 static time; and (12) evacuation of N_2 and any entrained gases. This sequence constituted one AB cycle of Al_2O_3 ALD. This reaction was carried out at 180 ℃.

The typical growth rate for Al_2O_3 ALD is 1.1-1.2 Å per ALD cycle [84, 149]. During the water dose a hydroxyl terminated surface is generated. The hydroxyl terminated surface will interact with excess H_2O in the reactor via hydrogen bonding. Due to the large surface area of the NG powders and the large surface area of the porous stainless steel cylinder, H_2O may not be completely purged from the reactor during the evacuation step of the H_2O dose. The presence of H_2O in the reactor during the TMA half reaction may lead to increased growth per cycle. This behavior is similar to chemical vapor deposition [83, 139].

Al_2O_3 ALD relies on an initially hydroxyl terminated surface to begin nucleation. The basel planes of graphite are inert and therefore not well suited to nucleating thin film growth. It has been demonstrated that an adsorbed monolayer of NO_2/TMA can act to functionalize the surface of carbon nanotubes [69, 35]. With the functionaliztaion layer in place, conformal Al_2O_3 growth can start by reacting the TMA molecules on the surface with H_2O. During the NO_2 nucleation treatment, an adsorbed functionalization layer was initially formed on the NG surface by alternating exposures of NO_2 and TMA [69]:

A
$$\mathrm{NG}^* + \mathrm{NO_2} \leftrightarrow \mathrm{NG} - \mathrm{NO_2^*} \tag{6.3}$$

B
$$\mathrm{NG} - \mathrm{NO_2^*} + \mathrm{TMA} \leftrightarrow \mathrm{NG} - \mathrm{NO_2^*} - \mathrm{TMA}^* \tag{6.4}$$

where the asterisks indicate surface species. In this functionalization process, the nitrogen of the NO_2 is attracted to the NG surface and leaves the oxygen atoms accessible. Upon TMA exposure, the oxygen atoms coordinate to the aluminum of the TMA molecule leaving a methyl-terminated surface [69]. The methyl-terminated surface does not interact with subsequent NO_2 exposures.

In order to grow conformal films on the basel plane of the NG a NO_2/TMA pretreatment was employed prior to Al_2O_3 ALD. The NO_2/TMA pretreatment reaction sequence was (1) NO_2 dose to a set pressure; (2) NO_2 absorption time; (3) evacuation of excess NO2; (1) TMA dose to a set pressure; (2) TMA absorption time; (3) evacuation of excess TMA. This sequence defines one AB cycle of the NO_2/TMA pretreatment to functionalize the NG surface.

6.3.2 Al_2O_3 ALD on Electrodes

Al_2O_3 ALD was also grown on assembled electrodes. The reaction conditions were similar to those described in Section 6.3.1. ALD has been grown on a variety of porous substrates including aerogels [26], photonic crystals [109] and high aspect ratio trench structures [64]. A composite LIB electrode consists of an assembly of particles held together with a polymer binder on metal foil. The space in between the NG particle provides a path for the ALD precursors and reaction byproducts to diffuse in and out of the electrode. Given sufficient time the ALD precursors will be able to diffuse through the tortuous paths in between the particles and uniformly coat the NG particles. NG electrodes were secured to an Al sample holder prior to being placed in the ALD reactor.

6.3.3 Electrical Conductivity

The electrical conductivity was measured by pressing a cylindrical pellet of NG into a custom plastic mold equipped with four electrical contacts arranged in a cross around the cap of the cylinder. The measurement was carried out while the pellet inside the plastic mold was pressed to a pressure of 120 MPa. A current in the range of 0.5-5 μA was sourced between two adjacent electrical contacts and the potential was measured across the two remaining electrical contacts. The resistance was obtained from the slope of a five point voltage vs. current curve. The geometric factor was extracted by measuring the samples with different configuration. This technique for determining resistivity was pioneered by van der Pauw [193].

6.3.4 Scanning Electron Microscopy and Energy Dispersive X-ray Spectroscopy

Al_2O_3 ALD coated NG electrodes were prepared for scanning electron microscopy (SEM) and energy dispersive X-ray spectroscopy (EDS) in two ways. Cross sections of Al_2O_3 ALD coated NG electrodes were cut for SEM imaging and EDS mapping. Because it is possible to back scatter the material being milled, a hole was drilled through the Cu foil on the electrode to reveal an unperturbed NG/Cu interface. The cross section and the hole were fabricated using focused ion beam (FIB) gallium milling with a NOVA 600i dual beam FIB instrument (FEI, Hillsboro, OR).

A JEOL JSM-6480LV SEM (Peabody, MA) equipped with a Thermo Scientific (West Palm Beach, FL) Noran System Six Microanalysis System X-ray detector was used to image the cross section of the Al_2O_3 ALD coated NG electrode and map the Al concentration throughout the cross section. EDS was also used to observe the Al concentration at the NG/Cu interface though the hole that had been milled through the Cu. The SEM was run at a pressure of $\sim 10^{-6}$ Torr. Images were collected at an acceleration voltage of 15 kV. EDS spectra and mapping were analyzed using Thermo Scientific's NSS 2.2 X-ray micro analysis software.

6.3.5 Electrochemical Characterization

N-methyl pyrrolidinone from Sigma-Aldrich (St. Louis, MO) was used as the solvent to prepare the electrode material. Poly(vinylidine fluoride)(PVDF) from Alfa Aesar (Ward Hill, MA) was used as a polymer binder. A slurry of NG and PVDF in N-methyl pyrrolidinone was spread on Cu foil to fabricate the NG electrodes. The NG to PVDF weight ratio was 90:10. The electrolyte, 1.0 M $LiPF_6$ dissolved in a solution ethylene carbonate (EC):dimethylcarbonate (DMC) (1:1 by volume), was obtained from Novolyte (Cleveland, OH). In order to test the stability of propylene carbonate (EC) with ALD coated NG electrodes, some experiments used 1 M $LiPF_6$ in PC.

Lithium metal from Alfa Aesar (Ward Hill, MA) was employed as the counter electrode. The electrode diameters were 0.5". A glass fiber sheet was used as a separator between the Li metal and the NG electrode. Cells were fabricated using 2032-type coin cell (diameter 20 mm, thickness 3.2

mm) in a glove box under an Ar environment (Vacuum Atmosphere's Inc., Amesbury, MA). The H_2O and O_2 concentrations in the glove box were typically under 0.1 and 0.5 ppm respectively.

Galvanostatic charge-discharge cycling was performed in the range of 0.005-1.5 V versus Li/Li^+ using a galvanostat (Arbin Instrument, College Station, TX). The current density during the first to charge-discharge cycles was 0.1 C-rate (37 mA g^{-1}. For subsequent cycles the current density was 0.5 C-rate (185 mA g^{-1}. Charge-discharge cycling was carried out at room temperature and at 50 ℃.

Full cells were assembled from NG anodes and $LiCoO_2$ cathodes. The preparation of the $LiCoO_2$ cathodes is described in Section 5.3.3. The full cells had a porous 20 μm thick polypropylene/polyethylene/polypropylene trilayer separator between the two electrodes. The weight ratio of $LiCoO_2$ to NG was ∼1.4. The full cells were cycled in the range of 3.304.45 V. The current density during the first to charge-discharge cycles was 0.1 C-rate (14 mA g^{-1} of $LiCoO_2$). For subsequent cycles the current density was 1 C-rate.

6.3.6 Differential Scanning Calorimetry

Differential scanning calorimetry (DSC) experiments were conducted using a thermal analysis tool from Perkin-Elmer (Waltham, MA). DSC experiments were conducted on bare NG electrodes and electrodes coated with 5 cycles of Al_2O_3 ALD after having undergone the NO_2/TMA pretreatment. The electrodes were examined over the temperature range 50-350 ℃. The scan rate was 10 ℃ min^{-1}.

Both the bare and the Al_2O_3 ALD coated electrode were lithiated at the time of the DSC measurement. The electrodes were lithiated by cycling the electrodes four times between 0.005 and 1.5 V against Li metal. The current density was 0.063 mA cm^{-2}. 1 M $LiPF_6$ in a solution of EC and ethyl methyl carbonate (EMC) was used as the electrolyte. The ratio of EC to EMC was 3:7 by weight. Prior to cell disassembly the electrodes were charged to 0.005 V. Lithiated electrodes were removed from the battery cells. The electrode material was scraped off of the Cu foil current collector into a sealable high pressure stainless steel crucible. All DSC sample preparation was

conducted in an inert Ar environment. An identical, empty, sealed stainless-steel crucible was used as the reference pan for the calorimeter.

6.4 Results and Discussion

Figure 6.2a shows an SEM image of the cross section of an NG electrode that had been coated with 5 cycles of Al_2O_3 ALD after electrode fabrication. From Figure 6.2a it is clear that the electrode is porous. The line that defines region 1 in Figure 6.2a traces the edge of the trench cut with FIB gallium milling and the top surface of the electrode. Regions 2-6 in Figure 6.2a are the cross section of the electrode and region 7 is the Cu foil current collector. The seven regions shown in Figure 6.2a were analyzed with EDS, the results are shown in Figure 6.2b. Figure 6.2b shows the weight % of Al ($Al/(C + Cu + Al)$) as a function of the region number . It is clear that there is Al throughout the cross section of the electrode. The concentration of Al throughout the cross section of the electrode is relatively constant until the Cu foil, at which point the Al concentration decreases. The relatively constant Al concentration is indicative of a uniform Al_2O_3 throughout the cross section of the electrode. The decrease of the Al signal on the Cu foil indicates that the uniformity of the Al is not an artifact of the ion milling process uniformly redistributing the Al. In order to verify that Al_2O_3 ALD was able to coat the full cross section of the electrode, a hole through the Cu foil was milled to exposes the Cu/NG interface. By approaching the Cu/NG interface from the back side it was not possible to inadvertently redistribute Al_2O_3 from the electrode surface. EDS confirmed the presence of Al at the Cu/NG interface when approached from the Cu side of the electrode. This conclusively demonstrates that the ALD precursors are able to diffuse through the tortuous paths of the NG electrode.

The conformality of the Al_2O_3 ALD film on the assembled electrode was not confirmed by the SEM/EDS analysis. Measurement of the conductivity of bare NG, Al_2O_3 ALD coated NG, and Al_2O_3 ALD coated NG with the NO_2/TMA pretreatment revealed the importance of the NO_2/TMA pretreatment. The results of the conductivity measurement are shown in Figure 6.3. The bare NG exhibited the highest conductivity at 668.8 S·cm^{-1}. The addition of 5 and 10 cycles

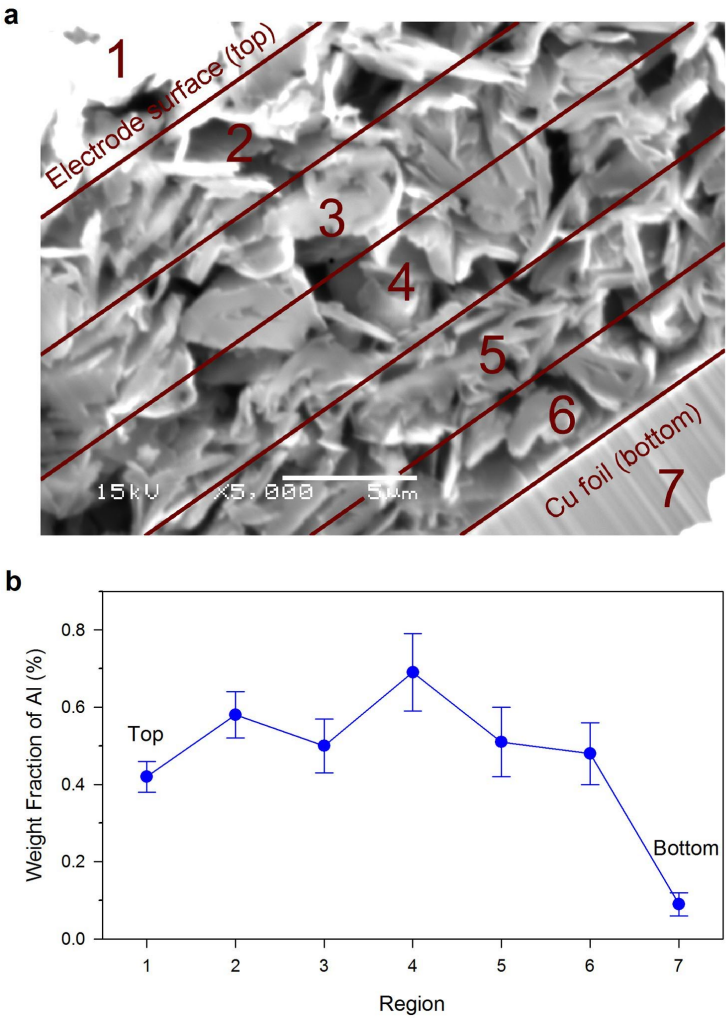

Figure 6.2: a) SEM image of the cross section of an NG electrode that had been coated with 5 cycles of Al_2O_3 ALD after electrode fabrication. Numbers indicate regions in which Al was analyzed with EDS. b) Weight fraction of Al as a function of region number on the SEM.

of Al_2O_3 ALD, without the NO_2/TMA pretreatment, reduced the conductivity to 304.3 and 199.7 $S{\cdot}cm^{-1}$ respectively. The reduction of the conductivity by the addition of an insulating Al_2O_3 ALD film was to be expected. The further reduction of the conductivity by the same number of cycles of Al_2O_3 ALD with the NO_2/TMA pretreatment indicates that with the NO_2/TMA pretreatment the Al_2O_3 ALD is more conformal. NG particles with 5 and 10 cycles of Al_2O_3 ALD, with the NO_2/TMA pretreatment, had conductivity of 59.8 and 44.9 $S{\cdot}cm^{-1}$ respectively. The same enhancement to the conformality of the Al_2O_3 ALD film from the NO_2/TMA pretreatment on NG particles should translate to Al_2O_3 ALD on assembled NG electrodes.

Electrodes assembled from bare NG and Al_2O_3 ALD on NG powder and electrodes that were coated with Al_2O_3 ALD after assembly were subjected to charge-discharge cycling at 50 ℃. Increasing the temperature should accelerate detrimental side reactions on the electrode [21] which allows for more rapid testing of the cells. The discharge capacity as a function of the number of charge-discharge cycles is shown in Figure 6.4. The bare NG rapidly lost its capacity with increasing charge-discharge cycles. The loss of capacity on the bare NG is attributed to the formation of SEI due to the decomposition of the electrolyte [220].

Electrodes assembled from NG particles that were coated with 5 cycles of Al_2O_3 ALD exhibited a dramatically decreased capacity retention as compared to the bare NG. This effect is shown in Figure 6.4. The insulating nature of the Al_2O_3 film was believed to be the cause of the decreased capacity. The Al_2O_3 film may block conduction pathways between both adjacent NG particles and NG particles and the Cu current collector. Table 6.1 shows schematics of the conduction pathways for bare NG, ALD on NG powder and ALD on assembled NG electrode.

As compared to bare NG, electrodes that were assembled prior to coating with 5 cycles of Al_2O_3 ALD displayed a dramatically enhanced capacity retention with respect to the number of charge-discharge cycles. This effect is shown in Figure 6.4. The NO_2/TMA pretreatment did not play a significant role in the capacity enhancement for ALD grown directly on the electrode. The chargedischarge capacity retention for the electrode with the NO_2/TMA pretreatment and 5 cycles Al_2O_3 ALD was 96% after 200 chargedischarge cycles, with respect to the capacity at the third

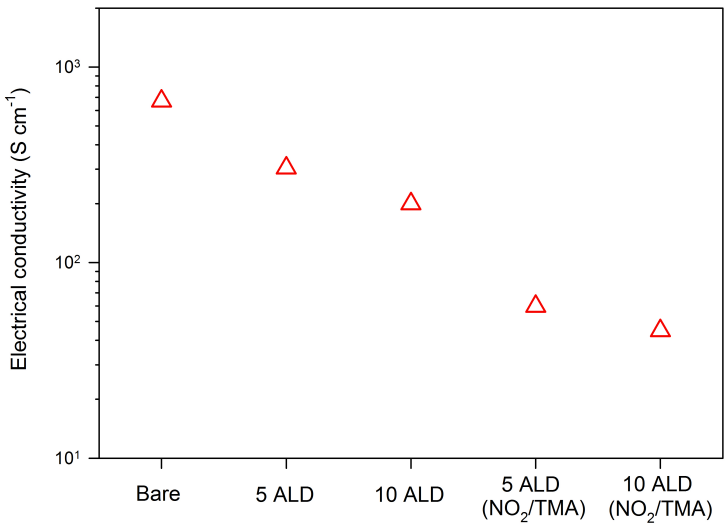

Figure 6.3: Electrical conductivity of bare and Al_2O_3 ALD coated NG powders.

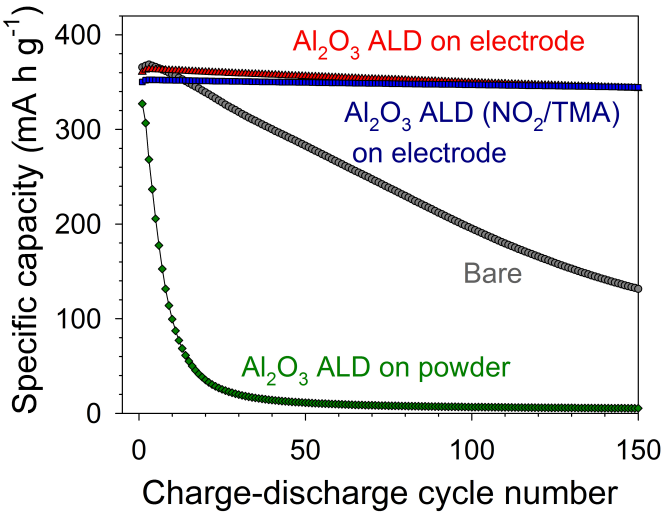

Figure 6.4: The discharge capacity as a function of the number of charge-discharge cycles for bare NG and Al_2O_3 ALD on NG powder, and electrodes that were coated with Al_2O_3 ALD after assembly. All charge-discharge cycles were carried out at 50 ℃

chargedischarge cycle. For a similar electrode without the NO_2/TMA pretreatment, the capacity retention was 93%. While the conductivity measurement shown in Figure 6.3 seem to indicate that the NO_2/TMA pretreatment does produce a less conductive and therefore more conformal film, the enhanced conformality does not appear to dramatically improve the electrode's electrochemical performance. It may be possible the NG has a sufficient number of defect and edge sites to allow the Al_2O_3 ALD without the use of NO_2/TMA pretreatment.

Table 6.1: Electron conduction pathways for bare NG, ALD on NG powder and ALD on assembled NG electrode.

	Bare NG	ALD on Powder	ALD on Electrode
Conduction Path	**Good**	Poor	**Good**
Surface Protection	Poor	**Good**	**Good**
	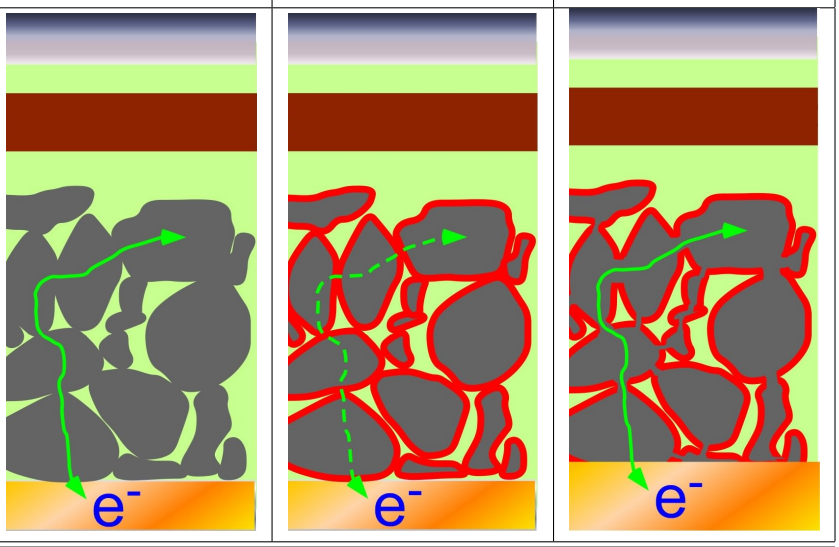		

As it is depicted in Table 6.1, it is believed the conduction pathway remains intact when an assembled electrode is coated with Al_2O_3 ALD. The presence of the protective Al_2O_3 ALD film and maintaining the conduction pathways between NG adjacent particles, and NG particles and the Cu current collector are both crucial to enhancing the electrode performance. The Al_2O_3 ALD film may serve as an "artificial" SEI that blocks the decomposition of the electrolyte on the electrode surface.

Figure 6.5 shows the capacity retention is also improved when the electrodes are subjected

to charge-discharge cycles at room temperature. The results, showing the capacity retention with respect to the third charge-discharge cycles at the 100^{th} and 200^{th} charge-discharge cycle are summarized in Table 6.2. Though it is not evident from Figures 6.4 or 6.5, Table 6.2 show that thicker, more conformal (NO_2/TMA pretreatment) films have larger capacity retention. For comparison Table 6.3 shows the capacity retention for NG coated with a variety of materials [104, 117, 123].

Table 6.2: Capacity retention of Al_2O_3 coated NG electrodes at the 100^{th} and 200^{th} charge-discharge cycle with respect to the 3^{rd} charge-discharge cycle.

Temperature	Al_2O_3 ALD	NO_2/TMA Pretreatment	Capacity Retention 100^{th} Cycle (%)	Capacity Retention 200^{th} Cycle (%)
RT	Bare		90	80
RT	2	No	100	99
RT	5	No	104	102
RT	5	Yes	104	103
50 ℃	Bare		53	26
50 ℃	2	No	96	88
50 ℃	5	No	97	93
50 ℃	5	Yes	99	96

The capacity retention is referenced to the third charge-discharge cycle due to SEI formation during the first two charge discharge cycles [150, 151, 220, 74, 16]. SEI formation irreversibly consumes Li from the cathode which reduces the capacity of the cell. The SEI is a high impedance film on the electrode surface. The increased impedance may also reduce the performance of the cell. SEI films of thicknesses varying from 4.5-980 nm have been reported in the literature [113, 214, 74, 22, 220]. Table 6.4 shows several SEI thicknesses, the material on which they were observed and the analysis technique used to determine the SEI film thickness. Controlling how the SEI forms, thickness and materials composition, is critical to determining the performance of the electrode.

Figure 6.6 shows the first charge for bare NG and NG electrodes coated with 5 cycles of Al_2O_3 ALD, with and without the NO_2/TMA pretreatment. The small plateau at around 0.7 V (versus Li/Li_+) corresponds to the reductive decomposition of the electrolyte to form the SEI

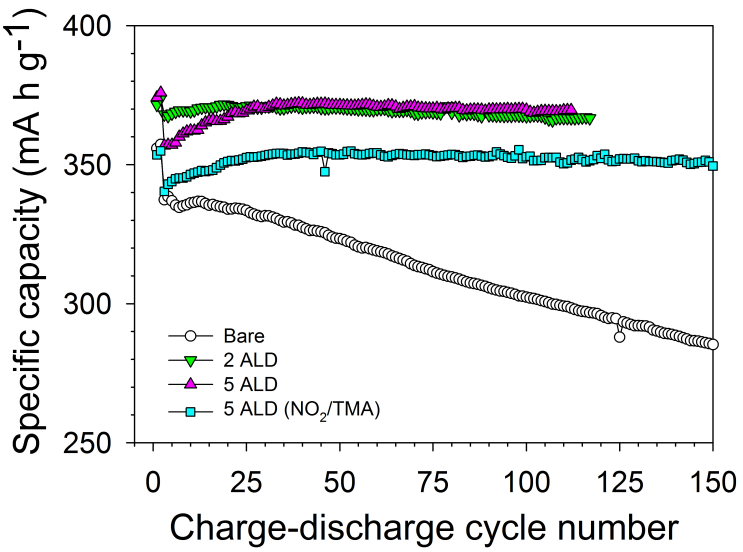

Figure 6.5: The discharge capacity as a function of the number of charge-discharge cycles for bare NG and Al_2O_3 ALD on NG powder, and electrodes that were coated with Al_2O_3 ALD after assembly. All charge-discharge cycles were carried out at room temperature.

Table 6.3: Capacity retention of coated-NG powders by wet chemical techniques [104, 117, 123]

Coating Material	Temperature	Electrode Composition	Current (mA g^{-1})	Sample	Capacity Retention
Al_2O_3	RT	80:10:10	175	Bare	76% (100^{th} cycle)
				Coated	93% (100^{th} cycle)
ZrO_2	30 ℃	80:10:10	1050	Bare	65% (100^{th} cycle)
				Coated	88% (100^{th} cycle)
$AlPO_4$	NA	96:4	350	Bare	36% (50^{th} cycle)
				Coated	79% (50^{th} cycle)

[155]. The effect is more obvious in a plot of the derivative of the specific capacity with respect to voltage (dQ/dV), this plot is shown in Figure 6.7. The magnitude of the differential charge peaks in Figure 6.7 corresponds to the amount of SEI formed on the electrode surface from the reductive decomposition of the electrolyte. The largest SEI film was observed on the bare NG electrode. With 5 cycles of Al_2O_3 ALD, the magnitude of the differential voltage profile peak was reduced. This indicates that the Al_2O_3 films act to prevent the formation of the SEI. However, with 5 cycles of Al_2O_3 ALD and the NO_2/TMA pretreatment, the magnitude of the differential voltage profile peak was even further reduced. The least SEI was formed when the Al_2O_3 film was more conformal due to the NO_2/TMA pretreatment.

The coulombic efficiency is a ratio of the discharge capacity to the charge capacity, in an ideal battery it would be unity. Due to losses incurred in the formation of the SEI the coulombic efficiency is less than unity. Figure 6.8 shows the coulombic efficiency for the first charge-discharge cycle of a bare NG electrode and NG electrodes coated with 2 and 5 cycles of Al_2O_3 ALD, with and without the NO_2/TMA pretreatment. The coulombic efficiency was measured at room temperature and at 50 ℃. The worst coulombic efficiency was displayed by the bare NG electrode at cycled at 50 ℃. General trends in the performance were observed. Reducing the temperature increased the coulombic efficiency, which stems from the higher rates of electrolyte decomposition at elevated temperatures [21]. Thicker and more conformal Al_2O_3 ALD films further increased the coulombic efficiency. 2 and 5 cycles of Al_2O_3 ALD showed improved coulombic efficiency as compared to the

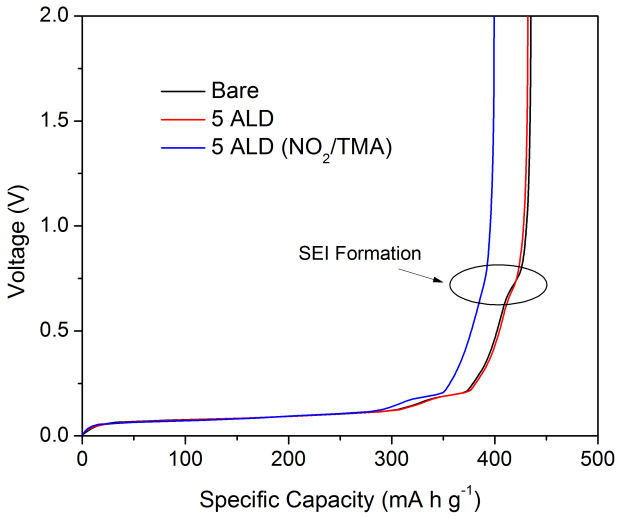

Figure 6.6: Voltage profiles for the first charge of a bare NG electrode and NG electrodes coated with 5 cycles of Al_2O_3 ALD, with and without the NO_2/TMA pretreatment.

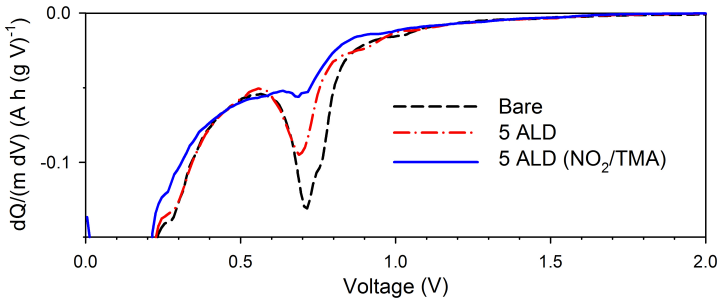

Figure 6.7: Differential voltage profiles for the first charge of a bare NG electrode and NG electrodes coated with 5 cycles of Al_2O_3 ALD, with and without the NO_2/TMA pretreatment.

Table 6.4: Thicknesses of SEI films on various graphitic surfaces.

Material	Measurement Technique	SEI Thickness
HOPG	Spectroscopic ellipsometry	36 nm [113]
Graphite fiber	SEM	200 nm [214]
Petroleum coke	Calculated	4.5 nm [74]
HOPG Edge	XPS Depth Profiling	35 nm [22]
HOPG basal plane	XPS Depth Profiling	7 nm [22]
NG	FIB and EDS	450-980 nm [220]

bare NG electrode. This result was improved upon by doing the NO_2/TMA pretreatment followed by 2 and 5 cycles of Al_2O_3 ALD. These results concur with the intensities of the differential charge peaks (Figure 6.7) to indicate that the Al_2O_3 ALD films suppress the formation of an SEI film during the first charge-discharge cycle.

Previous studies have revealed that SEI formation on highly ordered pyrolytic graphite (HOPG) occurs at different rates on the basal planes and at the graphite edges [22]. This is shown in Table 6.4. The varying degree of improvement from the Al_2O_3 ALD with and without the NO_2/TMA pretreatment may result from the ALD chemistry nucleates on the NG surface. Without the NO_2/TMA pretreatment the Al_2O_3 ALD may only nucleate on the edges or defects of the graphite, while with the NO_2/TMA pretreatment the Al_2O_3 ALD may be able to nucleate on all surfaces of the graphite. The more conformal film may better serve to protect the NG and help explain the improved performance with the NO_2/TMA pretreatment.

Figure 6.9 shows the differential scanning calorimetry plots for a lithiated bare NG electrode (6.9a) and an NG electrode that was coated with 5 cycles of Al_2O_3 ALD after the NO_2/TMA pretreatment (6.9b). At temperatures below 150 ℃ the ALD coated NG electrode did not generate as much heat as the bare NG electrode. The generation of heat by the bare NG electrode was attributed to the exothermic decay of an unstable SEI and further decomposition of the electrolyte. The reduced amount of heat generation below 150 ℃ by the NG electrode with an Al_2O_3 film was attributed to the enhanced stability and reduced amount of the SEI film generated in the presence

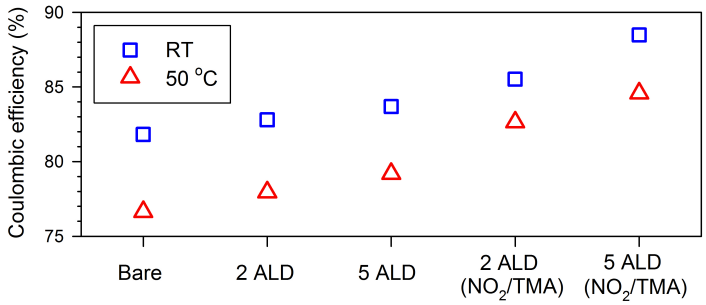

Figure 6.8: Coulombic efficiency for the first charge-discharge cycles of a bare NG electrode and NG electrodes coated with 2 and 5 cycles of Al_2O_3 ALD, with and without the NO_2/TMA pretreatment.

of the Al_2O_3 film. These results are consistent with the results shown in Figures 6.7 and 6.8.

6.4.1 Propylene Carbonate Electrolyte

Figure 6.10 shows the charge-discharge voltage profile of bare NG and an NG electrode coated with 5 cycles of Al_2O_3 ALD after the NO_2/TMA pretreatment. The electrolyte for this experiment was 1 M $LiPF_6$ in PC. This experiment was conducted at room temperature. Voltage plateaus in the range of 0.6-0.9 have been observed for the electrochemical decomposition of PC and the exfoliation of graphite [57, 9, 74, 218]. Figure 6.10 shows a similar plateau, at 0.8 V, for the bare NG electrode. In contrast, for NG electrode coated with 5 cycles of Al_2O_3 ALD after the NO_2/TMA pretreatment Figure 6.10 shows reversible Li ion insertion and extraction with no sign of the plateau at 0.8 V associated with the electrochemical decomposition of PC and the exfoliation of graphite. Figure 6.11 show the charge and discharge capacity for an NG electrode coated with 5 cycles of Al_2O_3 ALD after the NO_2/TMA pretreatment as a function of the number of charge-discharge cycles. The capacity is of Al_2O_3 ALD coated electrode is very stable, even in a PC based electrolyte. The near overlap of the charge and discharge capacity indicates the coulombic efficiency is near unity and very stable. It should be noted that the weight % of a 5 Å Al_2O_3 on a 4 μm NG particle is 0.05% as compared to 5-20 weight % used for a protective carbon film.

6.4.2 Full Cells

In most of the LIB literature electrochemical tests are performed on half cells (*i.e.* anode/Li or cathode/Li). Li metal is not a practical electrode outside of the laboratory due to reasons of safety. During charging-discharge cycling with a Li metal electrode dendrite formation on the Li electrode can eventually lead to an electrical short across the two electrodes [81, 194]. In the presence of a short circuit and the flammable organic electrolyte solvents currently in use, there is a risk of heat generation and fire [21, 213]. Using Li metal as the counter electrode simplifies electrochemical experiments because it does not introduce more complex cross reactions from an electrochemically more complex counter electrode. A Li metal counter electrode is the simplest

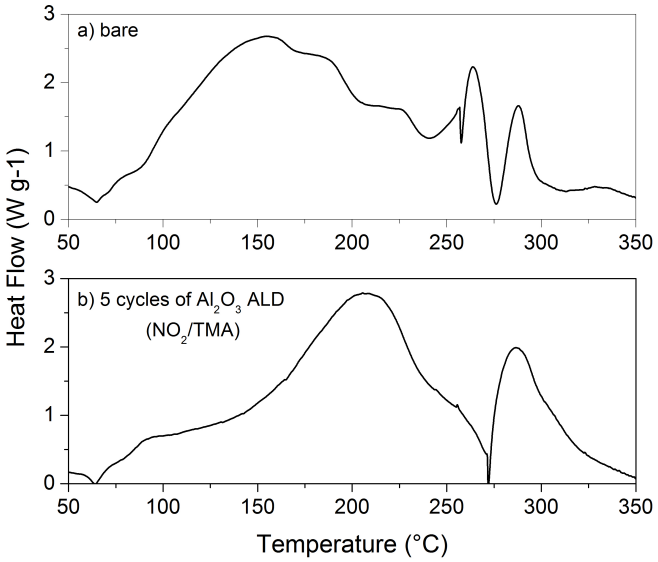

Figure 6.9: DSC plots of a) a bare NG electrode and b) an NG electrode that was coated with 5 cycles of Al_2O_3 ALD after the NO_2/TMA pretreatment.

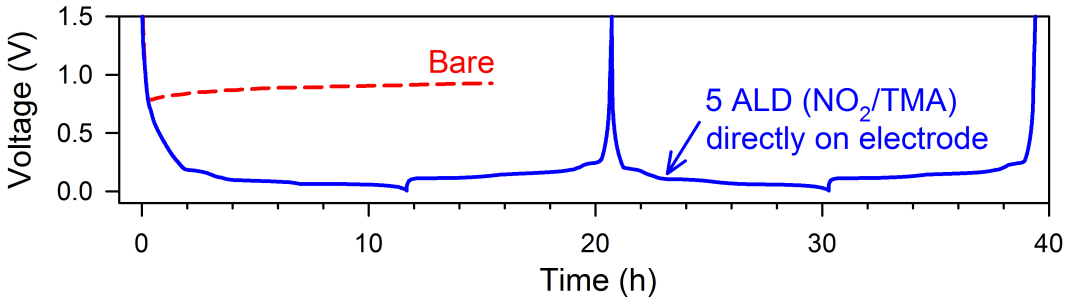

Figure 6.10: Voltage profiles of bare NG and an NG electrode coated with 5 cycles of Al_2O_3 ALD after the NO_2/TMA pretreatment.

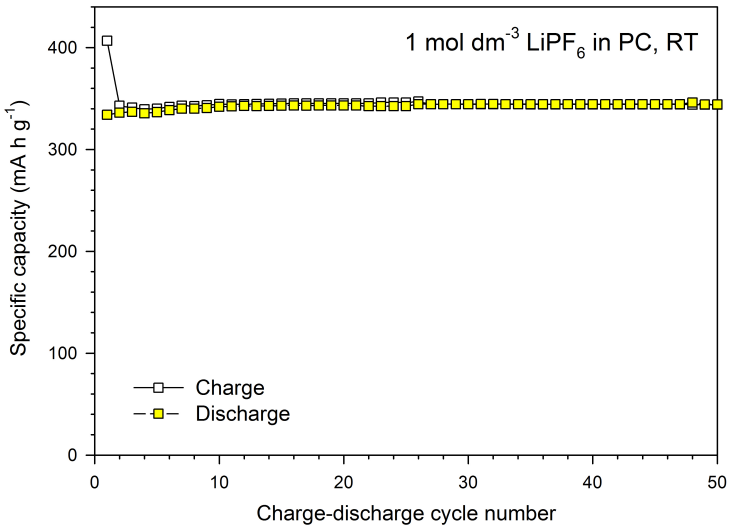

Figure 6.11: The charge and discharge capacity as a function of the number of charge-discharge cycles for an NG electrode that was coated with 5 cycles of Al_2O_3 ALD after an NO_2/TMA pretreatment. All charge-discharge cycles were carried out at room temperature. the electrolyte was 1 M $LiPF_6$ in PC.

configuration to effectively evaluate the performance of a new LIB material.

Once a material has been proven in a half cell it is necessary to evaluate it in a full cell. Unexpected complications can arise when Li metal is no longer used as the counter electrode. Amatucci *et al.* successfully demonstrated that $LiMn_2O_4$/Li and graphite/Li work well [6]. When the two half cells were combined to make a full cell ($LiMn_2O_4$/graphite) the battery performance suffered [6]. It is well known that $LiMn_2O_4$ can undergo Mn^{2+} dissolution in an electrochemical cell [6, 112, 41]. In a full cell dissolved Mn^{2+} can destabilize the SEI on the graphite surface and/or become a detrimental constituent of the SEI, leading to capacity loss [6, 112, 41].

The voltage profiles for bare $LiCoO_2$/NG full cells and $LiCoO_2$/NG full cells with 2 cycles of Al_2O_3 ALD are shown in Figure 6.12. The Al_2O_3 ALD was done on the $LiCoO_2$ powder prior to electrode assembly and on the NG electrode after electrode assembly. Voltage profiles are shown at the 3^{rd}, 50^{th}, 100^{th} and 200^{th} charge-discharge cycle. For the bare $LiCoO_2$/NG full cell, as the number of charge-discharge cycles increased the potential at which current began to flow during charging also increased. Similarly, during discharge, the more the cell had been charge-discharge cycled the greater the potential drop. These overpotentials may be attributed to the decomposition of the electrolyte on the either the $LiCoO_2$ or the NG. Or the overpotentials may be from electrochemical reactions between the $LiCoO_2$ or the NG and the electrolyte. From the voltage profile it is evident the capacity of the bare $LiCoO_2$/NG full cell fades with the increasing number of charge-discharge cycles. In contrast to this behavior, the $LiCoO_2$/NG full cell with 2 cycles of Al_2O_3 ALD appears comparatively stable with respect both to the development of an overpotential and capacity retention.

The discharge capacity retention as function of the number of charge-discharge cycles is shown in Figure 6.13. During the first two cycles the current density was 0.1 C-rate. After the first two cycles the current density was raised to 1 C-rate. The initial discharge capacity of the bare $LiCoO_2$/NG full cell was similar to that of the $LiCoO_2$/NG full cell with 2 cycles of Al_2O_3 ALD. After 200 charge-discharge cycles the bare $LiCoO_2$/NG full cell had retained only 13.6% of its initial capacity. In sharp contrast the $LiCoO_2$/NG full cell with 2 cycles of Al_2O_3 ALD had

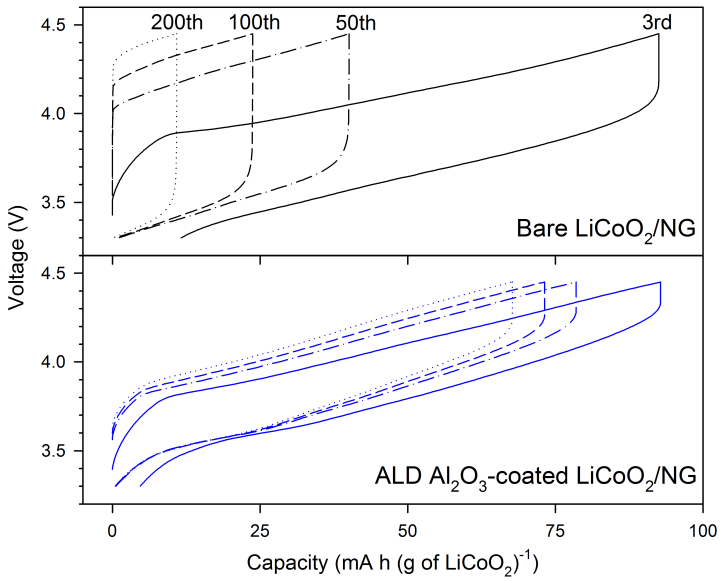

Figure 6.12: Voltage profiles for 3^{rd}, 50^{th}, 100^{th} and 200^{th} charge-discharge cycle of a bare NG/$LiCoO_2$ full cell and a Al_2O_3 ALD coated NG/$LiCoO_2$ full cell.

retained 76.5% of its initial capacity.

6.5 Conclusions

Al_2O_3 ALD films were grown on NG powders and on fabricated electrodes comprised of NG. The ability of the ALD precursors to penetrate a fabricated electrode was demonstrated with an EDS of a FIB cross section of the electrode and the superior performance of the coated electrode in PC electrolyte. The Al_2O_3 ALD on the NG particles dramatically reduced the discharge capacity, this may arise from the Al_2O_3 ALD film insulating the interparticle conduction pathways. ALD deposited directly onto fabricated NG electrodes protects the NG particle surfaces from undesirable interactions with the electrolyte while maintaining an electronically conductive pathway between both adjacent particles, and particles and the current collector. With respect to the third charge-discharge cycle, NG electrodes coated with 5 cycles of Al_2O_3 ALD had a capacity retention of 102% (no NO_2/TMA pretreatment) and 103% (with NO_2/TMA pretreatment) after 200 charge-discharge cycles at room temperature. At 50 ℃ the NG electrodes coated with 5 cycles of Al_2O_3 ALD had a capacity retention of 93% (no NO_2/TMA pretreatment) and 96% (with NO_2/TMA pretreatment) after 200 charge-discharge cycles. Bare NG electrodes had a capacity retention of 80% at room temperature and 26% at 50 ℃ after 200 charge-discharge cycles. As evidenced by the electrical conductivity, the first cycle differential charge profile, and the first cycle coulombic efficiency the NO_2/TMA pretreatment provides for a more conformal Al_2O_3 film. DSC measurement and the excellent charge-discharge capacity retention at 50 ℃ indicated the ALD coated NG electrodes were safer. The ability to use PC as the electrolyte is a promising result for the possibility to use NG in LIBs for HEVs.

6.5.1 A Note on Significance

Commercial battery grade graphite shows good charge-discharge cycle performance even at 50 ℃. In order to demonstrate the enhancement that an ALD film can provide a low grade graphite was employed in this study to accelerate LIB cell testing. It is believed that these enhancement

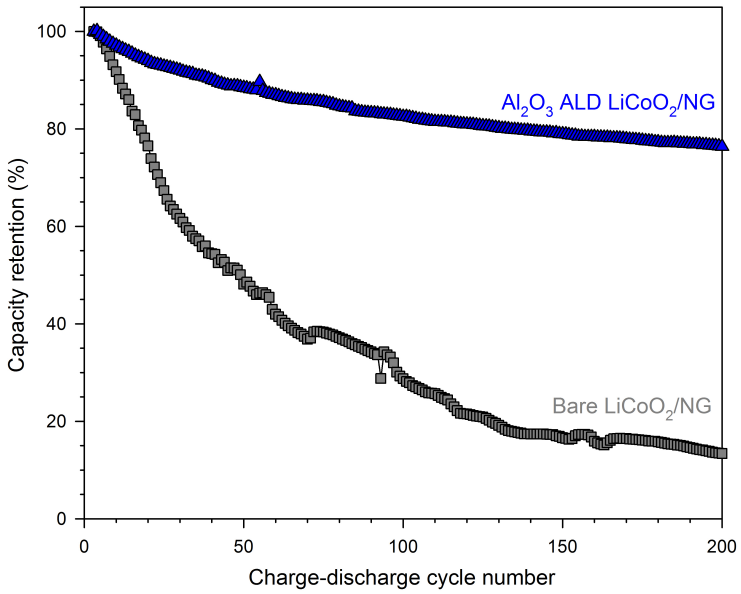

Figure 6.13: Capacity retention as a function of charge-discharge cycles of a bare NG/$LiCoO_2$ full cell and a Al_2O_3 ALD coated NG/$LiCoO_2$ full cell.

provided by the ALD film will translate to battery grade graphite.

6.6 Acknowledgements

This work was funded by a subcontract from a DOE SBIR grant to ALD Nanosolutions. A.S.C. received additional support from the iMINT DARPA Center at the University of Colorado. Y.S.J. acknowledges the Korea Research Foundation Grant funded by [KRF-2008-357-D00066]. A.C.D. is grateful for support from the U.S. Department of Energy under subcontract number DE-AC36-08GO28308 through: DOE Office of Energy Efficiency and Renewable Energy Office of the Vehicle Technologies Program. S.-H.K. gratefully acknowledges support from the Office of FreedomCar and Vehicle Technologies of the U.S. Department of Energy.

Chapter 7

Atomic Layer Deposition on Gram Quantities of Multiwalled Carbon Nanotubes

7.1 Abstract

Atomic layer deposition (ALD) was employed to grow coaxial thin films of Al_2O_3 and Al_2O_3/W bilayers on multiwalled carbon nanotubes (MWCNTs). Although the MWCNTs have an extremely high surface area, a rotary ALD reactor was successfully employed to perform ALD on gram quantities of MWCNTs. The uncoated and ALD-coated MWCNTs were characterized with transmission electron microscopy and x-ray photoelectron spectroscopy. Al_2O_3 ALD on untreated MWCNTs was characterized by nucleation difficulties that resulted in the growth of isolated Al_2O_3 nanospheres on the MWCNT surface. The formation of a physisorbed NO_2 monolayer provided an adhesion layer for the nucleation and growth of Al_2O_3 ALD films. The NO_2 monolayer facilitated the growth of extremely conformal coaxial Al_2O_3 ALD coatings on the MWCNTs. Cracks were also observed in the coaxial Al_2O_3 ALD films on the MWCNTs. After cracking, the coaxial Al2O ALD films were observed to slide on the surface of the MWCNTs and expose regions of bare MWCNTs. The Al_2O_3 ALD film also served as a seed layer for the growth of W ALD on the MWCNTs. The W ALD films can significantly reduce the resistance of the W/Al_2O_3/MWCNT wire. The results demonstrate the potential for ALD films to tune the properties of gram quantities of very high surface area MWCNTs.

7.2 Introduction

Carbon nanotubes (CNTs) have exceptional properties including low electrical resistance [75, 184], high mechanical strength [190, 210] and high thermal conductivity [25, 104]. CNTs can be used as building blocks for the fabrication of nanodevices including chemical sensors [114] and field effect transistors [137]. CNTs can also be employed for many purposes such as field-emission electron sources [56] and nanoprobes for scanning probe microscopy [54]. There are many other emerging applications for both individual CNTs and dispersions of CNTs in composite materials [23, 189]. Many of these applications require thin films deposited on the CNTs to insulate, protect or functionalize the CNTs.

CNTs may also serve as a mechanically robust, electronically conductive scaffolding. Lithium ion battery (LIB) active materials such as TiO_2 or MoO_3 could be deposited onto CNTs. The insulating nature of TiO_2 and MoO_3 make the interface with between the active material and the LIB conductive additive crucial to maintaining a good electronic conduction pathway [160]. The intimate contact between a thin film of the active material and the CNT may provide for enhanced electrical conductivity and superior LIB performance. Metal oxide anodes undergo a large volume expansion when they are in the charged (lithiated) state [124]. The volume expansion can lead to fracturing of individual particles and a loss of electronic conductivity [160, 124]. By keeping the films of the active materials thin and by growing them on CNTs with high mechanical strength it may be possible avoid fracturing if the CNTs are flexible enough to be compliant with the expansion of the anode material.

Atomic layer deposition (ALD) methods are preferred to obtain film deposition that is conformal and controlled film deposition at the atomic level. ALD is based on sequential, self limiting surface reactions [79, 181] and has been reported for many materials [156, 161]. ALD can be applied to CNTs because ALD has been demonstrated on very high aspect ratio structures [64] and nanoparticles [70]. Al_2O_3 ALD growth has been reported on individual single-walled carbon nanotubes (SWCNTs) [68, 69] and multiwalled carbon nanotubes (MWCNTs) [90, 122]. The nucle-

ation of Al_2O_3 ALD was identified as a significant problem for ALD on SWCNT surfaces [68, 69]. Fortunately, a functionalization procedure based on the adsorption of NO_2 and trimethylaluminum (TMA) has been shown to yield an adhesion layer on SWCNTs [69]. This adhesion layer facilitates the nucleation of Al_2O_3 ALD and produces very conformal Al_2O_3 ALD films using TMA and H_2O as the reactants [69]. ALD on CNTs has been developed for CNT nanotube transistors and logic gates [95]. ZrO_2 ALD has been employed to deposit high dielectric constant insulating layers on CNTs to fabricate field-effect transistors [95]. HfO_2 ALD on SWNTs has also been achieved to fabricate high performance thin-film transistors [32]. Nucleation difficulties for ZnO ALD on MWCNTs has been shown to lead to bead-shaped crystalline particles on the surface of the MWCNT that enhance electron field-emission [82]. In contrast, coaxial ZnO/Al_2O_3 heterostructures were fabricated on CNTs after depositing an Al_2O_3 adhesion layer on CNTs [106]. Vanadium oxide ALD has also been employed to fabricate gas sensors from CNTs [205]. Most of the previous applications for ALD on CNTs have been demonstrated using single CNTs. Single individual CNTs avoid the many difficulties that are encountered when attempting ALD on large quantities of CNTs. Gram quantities of CNTs have an extremely high surface area of 200-300 m^2/g and can be entangled to form CNT aggregates. ALD on large quantities of CNTs has the same problems as ALD on particles in particle beds. The CNTs must be agitated to enhance gas conductance of the ALD reactants to the individual CNTs. Likewise, the CNTs must be displaced relative to each other during ALD to prevent the CNTs from being glued together by the ALD film. Enhanced gas conductance and constant CNT motion in the bed of CNTs can be accomplished using fluidized bed reactors [201, 200] or rotary reactors [139, 140]. ALD on large quantities of CNTs would be useful for preparing CNTs for CNT/polymer composites. CNT/polymer composites should have high mechanical strength, high thermal conductivity and high electrical conductivity. Possible applications for these CNT/polymer composites include transparent conductive coatings, electromagnetic interference shielding and flexible electrostatic dissipation films. There are many previously reported examples of CNT/polymer composites [157, 189, 49, 121, 28]. However, dispersion of CNTs in the polymer composite is a difficulty and may limit the properties of the CNT/polymer com-

posite. ALD on the CNTs may help to improve the dispersion and coupling of CNTs in polymers. The inertness of the surface of the CNT is the cause for the insolubility of CNTs in water and organic solvents [187] and the lack of dispersion of CNTs in polymers. Covalent functionalization can enhance CNT solubility [187] and provide coupling between CNTs and polymers [28]. Unfortunately, covalent functionalization of the CNT surface damages the inherent properties of the CNT [19]. Surfactants can also noncovalently functionalize the surface of CNTs without perturbing the underlying CNT properties [85, 130]. However, covalent and noncovalent functionalization of CNTs both require wet chemical treatment. ALD can deposit ultrathin coatings on CNTs using gas phase procedures that will facilitate CNT dispersion without requiring a solution process. In this paper, ALD on large quantities of high surface area MWCNTs is demonstrated using a rotary ALD reactor. The nucleation of Al_2O_3 ALD on gram quantities of MWCNTs is achieved using NO_2 and TMA to form an adhesion layer. Without the NO_2 nucleation procedure, the Al_2O_3 ALD grew nanospheres on the MWCNT surface. With the NO_2 nucleation procedure, the Al_2O_3 ALD grew very conformally on the MWCNTs. The ALD-coated MWCNTs were examined using transmission electron microscopy (TEM) and x-ray photoelectron spectroscopy (XPS) versus the number of Al_2O_3 ALD reaction cycles. The Al_2O_3 ALD coating was also used as a foundation for the subsequent growth of W ALD films on the MWCNTs.

7.3 Experimental

7.3.1 MWCNTs and Rotary Reactor

The MWCNTs used in these experiments were 7000 series MWCNTs from Nanocyl (Sambreville, Belgium). For the Al_2O_3 ALD and W ALD, trimethylaluminum (97%) and WF_6 were obtained from Sigma-Aldrich (St. Louis, MO). HPLC grade H_2O was also from Sigma-Aldrich and was further purified by 5 cycles of freeze-pump-thaw. For the NO_2 nucleation treatment, commercial purity grade NO_2 (99.5%) was acquired from Airgas (Radnor, PA). The Si_2H_6 used for W ALD was from Voltaix Inc. (Branchburg, NJ). The specific surface areas of MWCNTs are on the order

of hundreds of m^2/g [89, 215, 162]. From Brunauer, Emmett and Teller (BET) measurements, the manufacturer reports a specific surface area of 250-300 m^2/g for the 7000 series MWCNTs. This surface area is approximately an order of magnitude larger than the nanopowders previously coated with ALD [139]. For equivalent masses of material, larger reactant exposures and purge times are required for the MWCNTs compared with typical nanopowders. BET measurements may also probe the inner surfaces of the MWCNT if the MWCNTs have open ends. ALD on particles is possible using either fluid bed reactors [201, 200] or rotary reactors [139, 140]. Rotary reactors have an advantage when performing ALD on nanoparticles because the rotary reactors can provide for static reactant exposures [139]. These static reactant exposures can minimize the amount of reactant that is lost to the vacuum pump. Recent work has demonstrated the feasibility of ALD on gram quantities of nanopowders in a rotary reactor [139]. The rotary reactor employed in this study was similar to the rotary reactor employed in the previous work [139, 140]. A schematic of the rotary reactor is shown in figure 7.1. Each reactant entered the reaction chamber (A) through a needle and pneumatic valve (B) that were attached to 0.25" welded ports on a custom 6.0" Conflat cap (C). During the reaction, the MWCNTs were mechanically agitated in a rotating porous cylinder (D). The rotation was achieved via a magnetically coupled rotary feedthrough (E). The pressure was monitored with 10 and 1000 Torr capacitance manometers (F). A gate valve (G) was opened to exhaust product gases and any excess precursor to the pump (H). Before coating the MWCNTs in the rotary reactor, MWCNTs quantities from 20 mg to 2 g were placed in the porous stainless steel cylinder with pore size of 10 μm. The porous metal cylinder was then attached to the magnetically-coupled rotary feedthrough (E). This feedthrough with the porous metal cylinder was then enclosed in the vacuum chamber of the rotary reactor and left to outgas under vacuum for 24 hours. Vacuum was obtained using a dual-stage rotary vane pump. Pressure was monitored with a Baratron capacitance manometer (MKS, Andover, MA). For the larger quantities of MWCNTs, the reactant exposures were scaled linearly according to the sample mass. For 1-2 g samples of MWCNTs, multiple doses of precursors were required to achieve the desired reactant exposure [140].

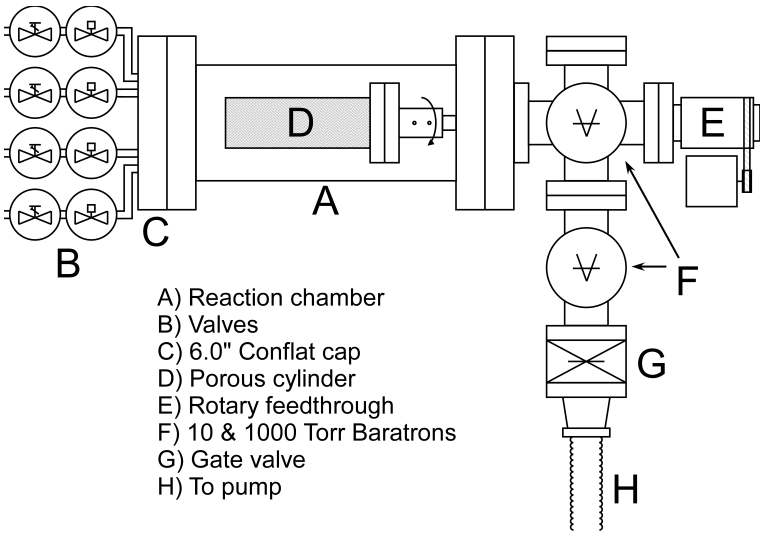

Figure 7.1: Schematic of rotary reactor used to coat gram quantities of MWCNTs.

A ceramic heater (Watlow Electric Manufacturing Co., St. Louis, MO) on the rotary reactor was employed for reactions performed at elevated temperatures. The temperature was monitored with a thermocouple and was manually controlled by applying a constant voltage to the resistive heating element. During the NO_2 functionalization treatment and ALD processing, the porous metal cylinder was rotated in the rotary reactor at 150 rpm. Given the diameter of the rotating porous cylinder, this rotational frequency is consistent with a centripetal force of 0.5g. Reasonable results were obtained using rotational frequencies from 140-180 rpm. Rotational frequencies <140 rpm led to less agitation and agglomeration during ALD. Rotational frequencies >180 rpm led to agglomeration resulting from the CNTs staying on the walls of the porous cylinder.

7.3.2 Al_2O_3 ALD and Surface Nucleation Chemistry

Al_2O_3 ALD was performed on gram quantities of MWCNTs in the rotary reactor. The Al_2O_3 ALD surface chemistry employs $Al(CH_3)_3$ (TMA) and H_2O as the reactants. The sequential, self-limiting reaction sequence during Al_2O_3 ALD is [58, 84, 149]:

A $$AlOH^* + Al(CH_3)_3 \rightarrow AlO - Al(CH_3)_2^* + CH_4 \quad (7.1)$$

B $$AlCH_3^* + H_2O \rightarrow Al - OH^* + CH_4 \quad (7.2)$$

where the asterisks denote surface species. The Al_2O_3 ALD reaction sequence was: (1) TMA dose to set pressure; (2) TMA reaction time; (3) evacuation of reaction products and excess TMA; (4) N_2 dose; (5) N_2 static time; (6) evacuation of N_2 and any entrained gases; (7) H_2O dose to pressure, (8) H_2O reaction time; (9) evacuation of reaction products and excess H_2O; (10) dose N_2; (11) N_2 static time; and (12) evacuation of N_2 and any entrained gases. This sequence constituted one AB cycle of Al_2O_3 ALD.

During the NO_2 nucleation treatment, an adsorbed functionalization layer was initially formed on the MWCNTs by alternating exposures of NO_2 and TMA [69]:

A $$MWCNT^* + NO_2 \leftrightarrow MWCNT - NO_2^* \quad (7.3)$$

B $$\text{MWCNT} - \text{NO}_2^* + \text{TMA} \leftrightarrow \text{MWCNT} - \text{NO}_2^* - \text{TMA}^* \quad (7.4)$$

where the asterisks indicate surface species. In this functionalization process, the nitrogen of the NO_2 is attracted to the CNT surface and leaves the oxygen atoms accessible. Upon TMA exposure, the oxygen atoms coordinate to the aluminum of the TMA molecule leaving a methyl-terminated surface [69]. The methyl-terminated surface does not interact with subsequent NO_2 exposures. Following the previous nucleation procedure [69], 50 cycles of NO_2/TMA were used to functionalize the MWCNTs at room temperature. This NO_2 treatment was performed with the following sequence: (1) exposure to NO_2 to set pressure; (2) NO_2 static reaction time; (3) evacuation of excess NO_2; (4) exposure to TMA to set pressure; (5) TMA static reaction time; and (6) evacuation of excess TMA. This sequence defines one AB cycle of the NO_2/TMA functionalization layer. For 20 mg of MWCNTs, the dose pressures were 300 mTorr for both NO_2 and TMA. The static reaction times for NO_2 and TMA were 10 s. The NO_2 and TMA purge times were 7 s and 30 s, respectively. The NO_2/TMA functionalization layer will desorb at elevated temperatures. Consequently, the adsorbed NO_2/TMA layer was stabilized with 5 AB cycles of Al_2O_3 ALD at room temperature. Al_2O_3 ALD growth could then be continued at higher reaction temperatures. For the Al_2O_3 ALD on the untreated MWCNTS and on the NO_2/TMA functionalized MWCNTs, the Al_2O_3 ALD reaction sequence was employed at 180 ℃. For 20 mg of MWCNTs, the dose pressures were 1.0 Torr for TMA and H_2O and 20 Torr for N_2. The reaction times for the TMA and H_2O were both 60 s. The N_2 static time was 5 s. All purge times were 60 s. Figure 7.2 displays the ALD reactor pressure versus time for one AB cycle of Al_2O_3 ALD for (a) untreated MWCNTs and (b) NO_2/TMA functionalized MWCNTs.

For both the untreated MWCNTs and the NO_2/TMA functionalized MWCNTs, the pressure responses during the TMA doses shown in figures 7.2a and 7.2b are similar. The pressure responses during the H_2O doses were different for the untreated MWCNTs and NO_2/TMA functionalized MWCNTs. For the untreated MWCNTs, figure 7.2a reveals that the pressure dropped following the H_2O dose of 1 Torr. For the NO_2/TMA functionalized MWCNTs, figure 7.2b shows that the

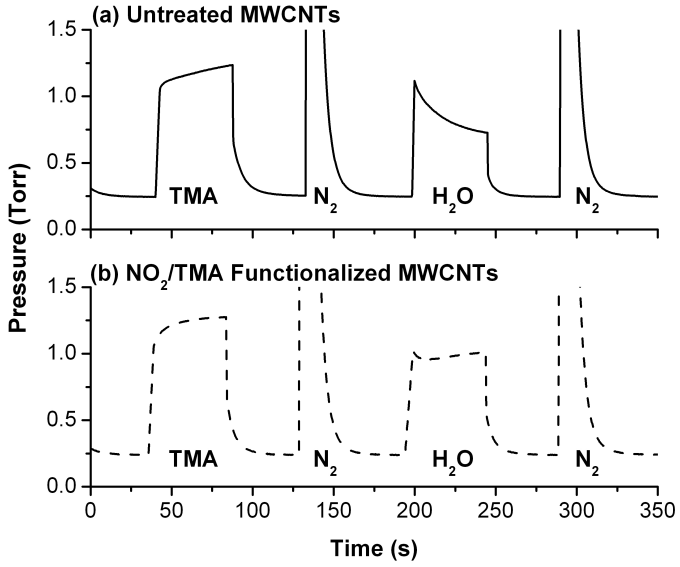

Figure 7.2: Reactor pressure versus time for one AB cycle during Al_2O_3 ALD for (a) untreated MWCNTs and (b) NO_2/TMA functionalized MWCNTs.

pressure dipped briefly and then returned to 1 Torr.

The difference in behavior for H_2O on the untreated MWCNTs and the NO_2/TMA functionalized MWCNTS is accounted for by the difference in reactive surface areas. The conformally coated MWCNTs have a larger Al_2O_3 surface area. The H_2O reacts nearly completely on this surface area and little extra H_2O is available for reabsorption. The pressure stays close to 1 Torr because H_2O is converted to CH4 reaction product. For the untreated MWCNTs and an equivalent H_2O exposure, the growth of Al_2O_3 nanospheres only consumes a fraction of the H_2O. The excess H_2O molecules then slowly adsorb on the Al_2O_3 surface.

After depositing an Al_2O_3 ALD layer on the MWCNTs, other ALD coatings can be applied such as W ALD. W ALD was accomplished using WF_6 and Si_2H_6 as the reactants. The sequential, self-limiting reaction sequence for W ALD is [110, 87]:

A $$WF_3^* + Si_2H_6 \rightarrow W - SiH^* + SiHF_3 + 2H_2 \tag{7.5}$$

B $$WSiH^* + WF_6 \rightarrow W - WF_3^* + SiHF_3 \tag{7.6}$$

The W ALD chemistry is not a truly self-limiting process. W ALD is dependent on the Si_2H_6 exposure and the substrate temperature [61]. A typical growth rate for W ALD is 5 Å/cycle [65].

For W ALD on the MWCNTs, the W ALD reaction sequence was: (1) dose Si_2H_6 to set pressure; (2) Si_2H_6 reaction time; (3) evacuation of reaction products and excess Si_2H_6; (4) N_2 dose; (5) N_2 static time; (6) evacuation of N_2 and any entrained gases; (7) dose WF_6 to set pressure; (8) WF_6 reaction time; (9) evacuation of reaction products and excess WF_6; (10) dose N_2; (11) N_2 static time; and (12) evacuation of N_2 and any entrained gases. This sequence constituted one AB cycle of W ALD. The W ALD reaction sequence was employed at 180 ℃. For 20 mg of MWCNTs, the dose pressures were 1.0 Torr for the Si_2H_6 and WF_6 and 20 Torr for the N_2. The reaction times for the Si_2H_6 and WF_6 were 200 s and the purge times were both 50 s. The N_2 static time was 20 s and the purge time was 200 s.

7.3.3 TEM and XPS Analysis

Transmission electron microscopy (TEM) images of the MWNCTs and ALD-coated MWCNTs were collected on a Philips CM10 electron microscope (Mahwah, NJ). A Gatan digital camera (Gatan, Pleasanton, CA) was used to record the images. Measurements of the micrographs were made in Deneba Canvas 9 (ACD Systems, Victoria, British Columbia, Canada). These measurements were used to determine the film thickness.

A PHI 5600 X-ray photoelectron spectrometer was used to obtain X-ray photoelectron spectra (XPS) of the ALD-coated MWCNTs. The powder samples were pressed into pellets with a thickness of 0.7 mm and a diameter of 5.5 mm and affixed to the sample puck with carbon tape. Monochromatic Al Kα x-rays (1486.6 eV) were used for the XPS analysis. The pass energy was 58.7-93.9 eV and the step size was 0.250-0.400 eV. An electron beam neutralizer was employed at 17.8 mA. Data was collected with Auger Scan (RBD Enterprises, Inc., Bend, OR). XPS data was analyzed in CASA XPS (Casa Software Ltd., U.K.). Peak fits for the W-4f peaks were obtained using a linear background and a 70:30 Gaussian: Lorentzian peak.

7.4 Results and Discussion

7.4.1 Entangled MWCNT Clusters

Transmission electron microscopy (TEM) images were used to characterize the MWCNTs and the ALD film growth on the MWCNTs. The uncoated MWCNTs were a fine powder. These uncoated MWCNTs displayed a range of tube diameters as observed by TEM. The manufacturer reported an average tube diameter of 10 nm. The nanotubes were also agglomerated in entangled clusters prior to the ALD coating. A TEM image of these uncoated entangled clusters of MWCNTs is displayed in figure 7.3. The diameter of these entangled clusters was $\sim$2-3 μm.

TEM images of the coated MWCNTs were typically imaged on the edge of a μm-scale entangled cluster. Further agglomeration of the MWCNTs during ALD was prevented by performing the ALD in the rotary reactor under agitation by rotation [139]. There were still μm-scale agglomerates

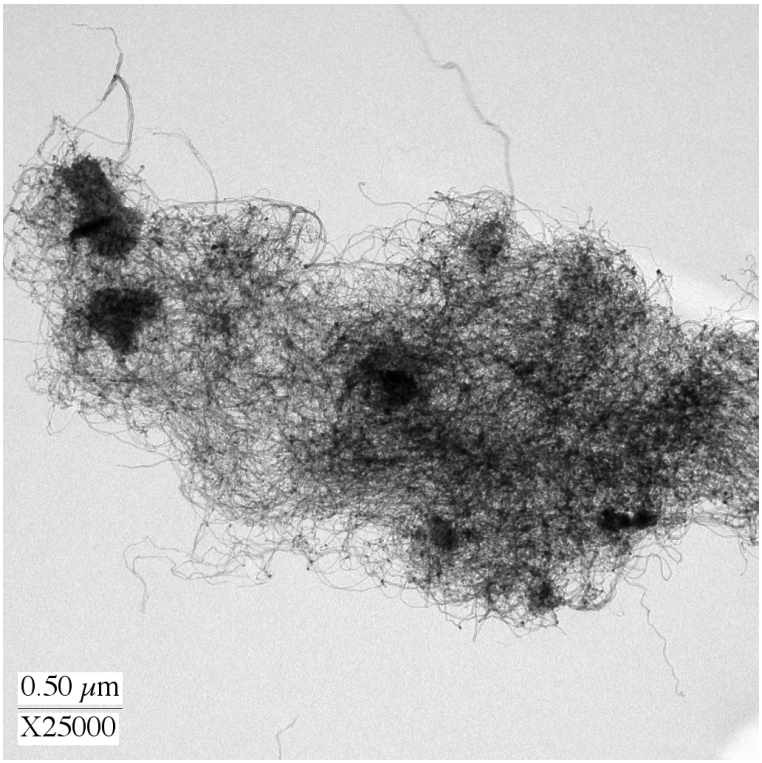

Figure 7.3: TEM image of an uncoated entangled cluster of MWCNTs.

of MWCNTs after ALD processing. Some of these agglomerates were mechanically crushed prior to TEM analysis to obtain MWCNTs from the center of the entangled clusters. MWCNTs from the edge and center of the entangled clusters were all found to be coated with Al_2O_3 ALD.

7.4.2 Al_2O_3 ALD Nanospheres on Untreated MWCNTs

ALD Al_2O_3 on untreated MWCNTs resulted in the growth of Al_2O_3 nanospheres. A TEM micrograph of these nanospheres after 50 AB cycles is shown in figure 7.4. The nanospheres are fairly spherical and monodisperse. The radii of the nanospheres are in the range of 11-13 nm. The TEM images suggest that Al_2O_3 ALD growth nucleates at specific sites on the MWCNT surface during the initial Al_2O_3 ALD cycles. The nanospheres then grow isotropically versus the number of AB cycles to yield fairly monodisperse sphere diameters. Very similar Al_2O_3 nanospheres were observed earlier after Al_2O_3 ALD on individual SWCNTs [68].

Figure 7.5 shows TEM images of the Al_2O_3 nanospheres after 100 AB cycles. There is an increase in the nanosphere diameter and the number of nanospheres after 100 AB cycles. However, the nanospheres are not as monodisperse compared with the nanospheres after 50 ALD cycles. The radii of the nanospheres range from 11-20 nm. This finite range indicates that the Al_2O_3 ALD nanospheres do not all nucleate at the same time. Sites that nucleate later should experience fewer Al_2O_3 ALD cycles and produce nanospheres with smaller radii. For adjacent nanospheres, the spheres eventually begin to coalesce to form a rough, pseudo-continuous Al_2O_3 film. Previous studies of Al_2O_3 ALD on individual MWCNTs have observed conformal growth on nanotube surfaces that were not intentionally functionalized [90, 122]. In contrast, figures 7.4 and 7.5 reveal that the Al_2O_3 ALD growth was not conformal in this study. Distinct nanospheres are observed that are similar to the Al_2O_3 nanospheres observed after Al_2O_3 ALD on unfunctionalized SWCNTs [68]. A possible explanation for this difference in growth involves the presence of defects or inadvertent chemical functionalization on the earlier MWCNT surfaces.

The density of defects and chemical functional groups on the MWCNT surface may be related to the method of MWCNT synthesis and subsequent cleaning and purification methods [4]. The

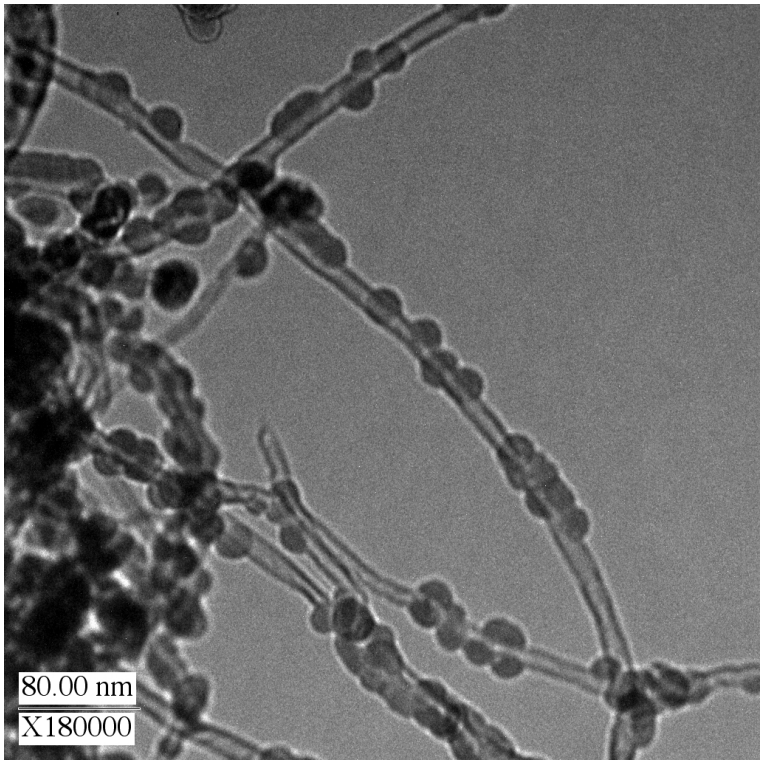

Figure 7.4: TEM image of untreated MWCNTs after 50 AB cycles of Al_2O_3 ALD.

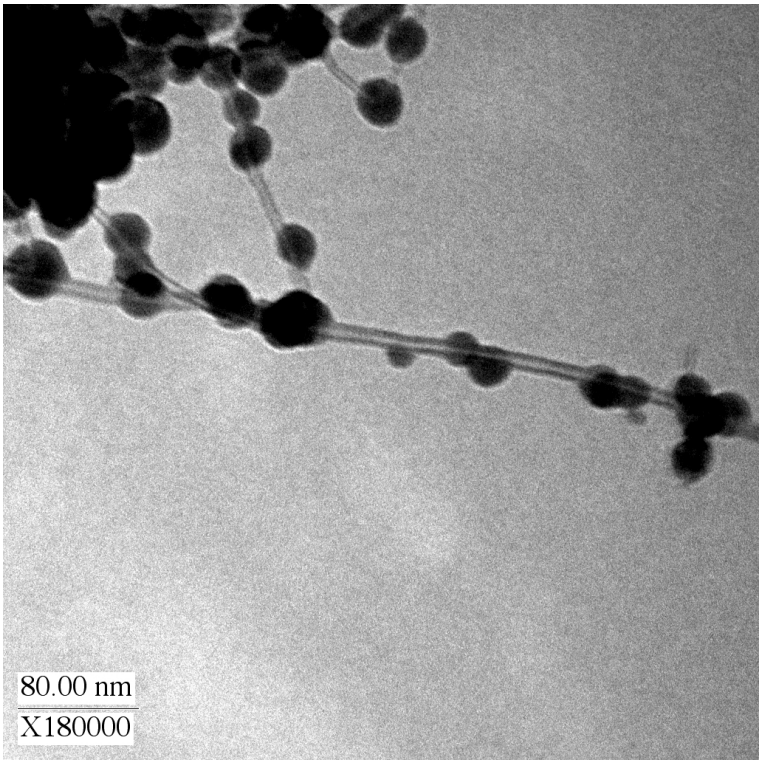

Figure 7.5: TEM image of untreated MWCNTs after 100 AB cycles of Al_2O_3 ALD.

growth of nanospheres may be expected for a low density of defects or active chemical species on the MWCNT surface. If the density of defects or active chemical species is much higher, the larger density could lead to a conformal Al_2O_3 ALD film. The defect density may have been significantly lower for the MWCNTs utilized in this study compared with MWCNTs used in previous studies [90, 122].

7.4.3 Conformal Al_2O_3 ALD Growth on NO_2/TMA Functionalized MWCNTs

To grow conformal Al_2O_3 ALD coatings on gram quantities of MWCNTs, a functionalization layer of adsorbed NO_2 and TMA was initially formed at room temperature. This adsorbed layer is not stable at the elevated temperatures typically used to grow Al_2O_3 ALD. However, this adsorbed layer can be stabilized with an Al_2O_3 passivation layer consisting of 5 AB cycles of Al_2O_3 ALD at room temperature. The Al_2O_3 ALD chemistry readily nucleated and grew conformally on this adsorbed layer.

Additional Al_2O_3 ALD cycles were performed at 180 ℃ to achieve the desired Al_2O_3 ALD film thickness. Figure 7.6 displays a TEM image after 50 AB cycles of Al_2O_3 ALD on the NO_2/TMA functionalized MWCNTs. In contrast to the nanospheres observed in figure 7.4 after 50 AB cycles, the Al_2O_3 films are smooth and conformal after 50 AB cycles on the NO_2/TMA functionalized MWCNTs. A second TEM image showing a larger portion of the entangled MWCNT cluster at a reduced magnification is presented in figure 7.7. A conformal Al_2O_3 ALD coating is observed on all the MWCNTs.

Figure 7.8 shows an enlargement of a coated MWCNT after 40 AB cycles. The Al_2O_3 ALD film is extremely conformal on the MWCNT. TEM images were performed after 25, 40, 50 and 60 AB cycles. TEM analysis of the film thickness was consistent with Al_2O_3 ALD growth that was linear with number of AB cycles. The Al_2O_3 ALD growth per cycle was 1.7 Å/cycle. This Al_2O_3 ALD growth per cycle is slightly larger than the growth per cycle of 1.1-1.2 Å/cycle reported for Al_2O_3 ALD on flat substrates [84, 149]. However, this Al_2O_3 ALD growth rate is in agreement with the growth rates reported for Al_2O_3 ALD on nanopowders of 1.8-2.0 Å/cycle [70, 139]. The larger

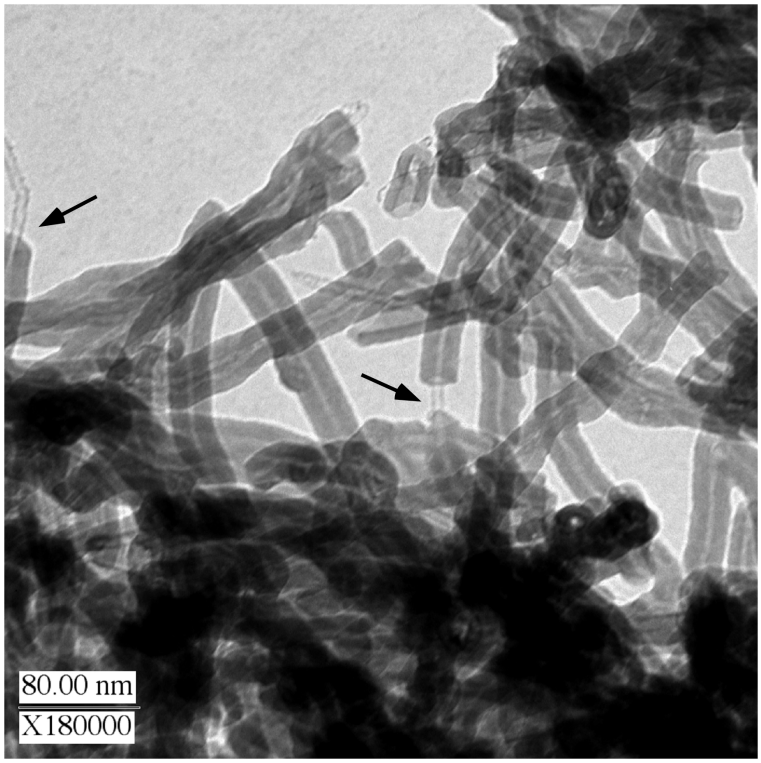

Figure 7.6: TEM image of NO_2/TMA functionalized MWCNTs after 50 AB cycles of Al_2O_3 ALD.

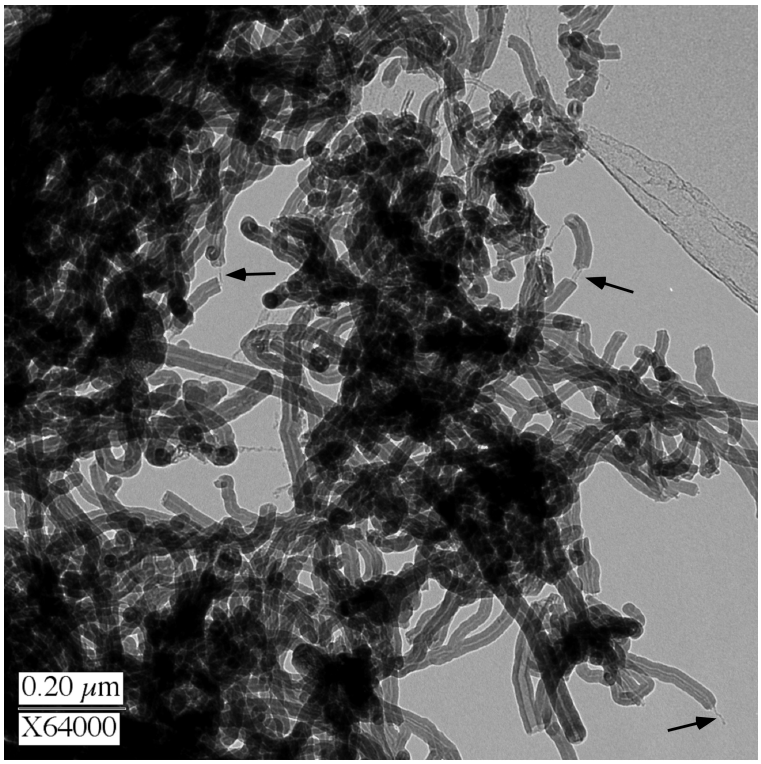

Figure 7.7: TEM image of NO_2/TMA functionalized MWCNTs after 50 AB cycles of Al_2O_3 ALD at lower magnification.

growths per cycle may result from the inability to purge H_2O completely from very high surface area samples.

7.4.4 "Macaroni" on MWCNT String

According to the proposed NO_2 nucleation mechanism, the Al_2O_3 ALD films are grown on an adsorbed layer of NO_2/TMA on the CNTs [69]. This adsorbed layer is not covalently attached to the surface of the CNT. Consequently, the coaxial Al_2O_3 ALD film on the CNT should be free to slide along the CNT. TEM images reveal this "sliding" behavior. Locations where the Al_2O_3 ALD film has broken on the MWCNT show evidence for the sliding of the Al_2O_3 ALD film along the MWCNT. Broken Al_2O_3 ALD films that have moved to reveal bare MWCNTs are indicated by the arrows in figures 7.6 and 7.7.

These broken sections of coaxial Al_2O_3 ALD film on the MWCNT are like "macaroni" on a MWCNT string. A TEM image that captures a segment of an Al_2O_3 ALD film on the MWCNT is displayed in figure 7.9. This Al_2O_3 ALD film was deposited using 60 AB cycles. The mechanical tumbling of the entangled clusters of MWCNTs may facilitate the breaking of the Al_2O_3 ALD films at the ends of MWCNTs. These Al_2O_3 ALD segments may then slide off the MWCNTs to reveal bare MWCNTs at the edge of an entangled cluster. Figure 7.10 shows a TEM image that reveals a number of bare MWCNTs dangling at the perimeter of an entangled MWCNT cluster.

7.4.5 Bilayers of W ALD/Al_2O_3 ALD on MWCNT

The conformal coaxial Al_2O_3 ALD coating on MWCNTs can serve as a substrate for the subsequent growth of another ALD material. W ALD was performed on the Al_2O_3 ALD coating to deposit a W/Al_2O_3 bilayer on the MWCNTs. The initial Al_2O_3 ALD film was prepared using the NO_2/TMA nucleation procedure and then 50 cycles of Al_2O_3 ALD. Subsequently, W ALD was grown on the Al_2O_3 ALD surface. Figure 7.11 displays a TEM image after 60 cycles of W ALD using WF_6 and Si_2H_6. The W ALD leads to an increase in diameter of the coated MWCNTs. Bare MWCNTs where the W/Al_2O_3 bilayer has slipped off the ends of MWCNTs are also indicated by

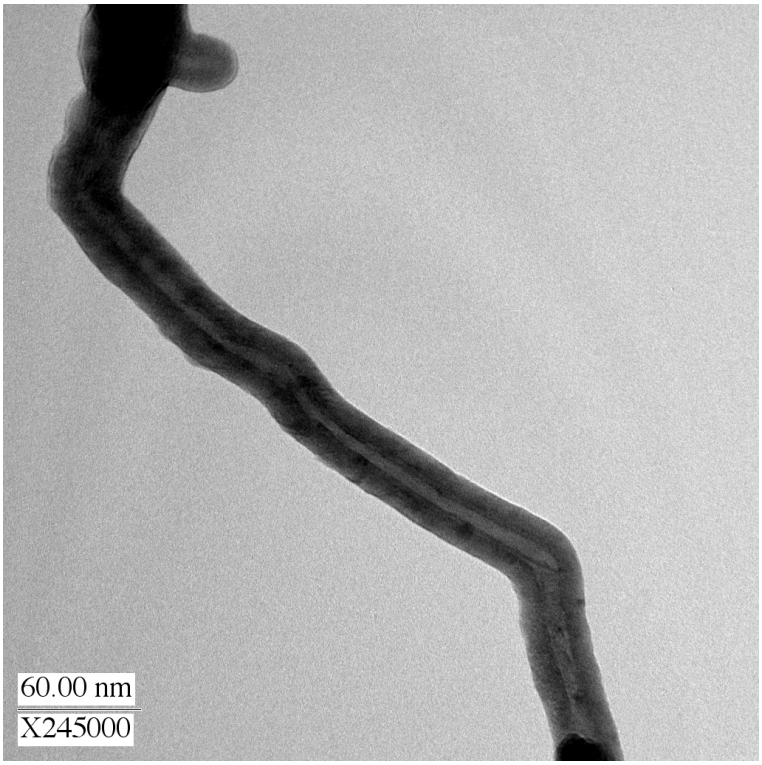

Figure 7.8: TEM image of NO_2/TMA functionalized MWCNT after 40 AB cycles of Al_2O_3 ALD at higher magnification.

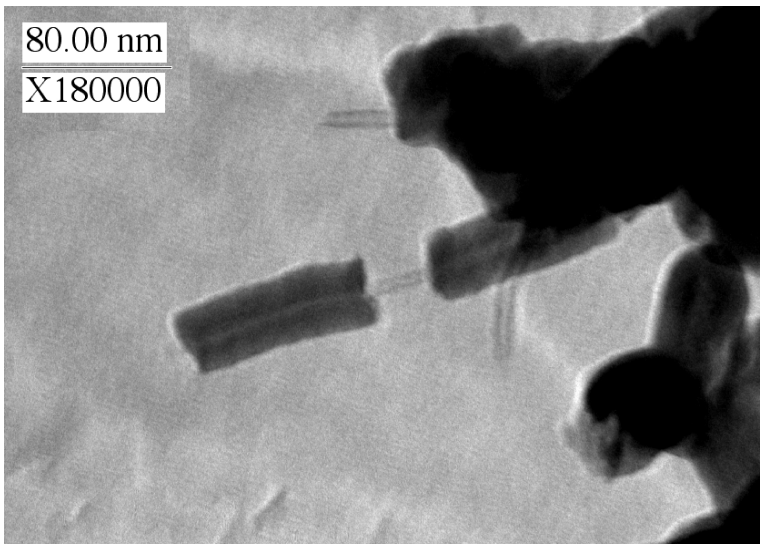

Figure 7.9: TEM image of NO_2/TMA functionalized MWCNTs after 60 AB cycles of Al_2O_3 ALD showing evidence for Al_2O_3 ALD film cracking and sliding on MWCNT.

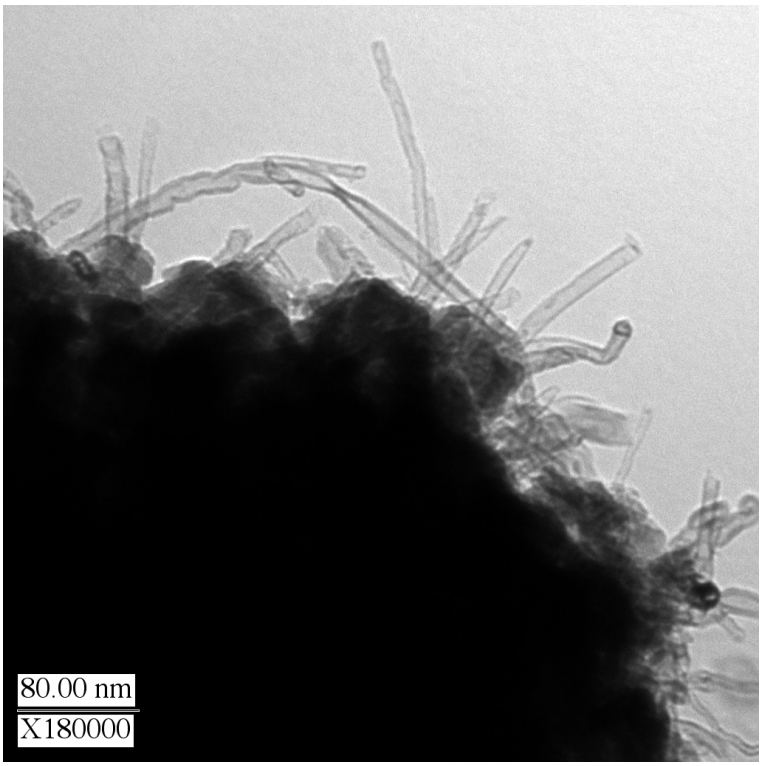

Figure 7.10: TEM image of NO_2/TMA functionalized MWCNTs after 60 AB cycles of Al_2O_3 ALD showing bare MWCNTs at the perimeter of entangled MWCNTs. These bare MWCNTs result from the Al_2O_3 ALD film cracking and sliding off the MWCNTs.

the arrows.

The surface of the W/Al_2O_3 bilayer film is rougher and more granular than the Al_2O_3 ALD film on MWCNTs. The surface roughness may be caused by the polycrystal W ALD film or difficulties for the W ALD nucleating on the Al_2O_3 ALD surface [86, 168, 208]. Both of these factors are believed to affect the roughness of W ALD layers in W/ Al_2O_3 nanolaminates [168, 66]. In spite of the increased roughness, the W/Al_2O_3 bilayer film is still conformal to the MWCNTs. TEM measurements of the W ALD film thickness were difficult because of the lack of a distinct boundary between the Al_2O_3 ALD film and the W ALD film. While the density disparity between Al_2O_3 ALD and W ALD should be evident, the geometry of the two coaxial nested cylinders prevented this distinction.

X-ray photoelectron spectroscopy (XPS) was used to analyze: (a) the uncoated MWCNTs; (b) the Al_2O_3 ALD on the untreated MWCNTs; (c) the Al_2O_3 ALD on the NO_2/TMA functionalized MWCNTs; and (d) the W ALD on the Al_2O_3 ALD on the NO_2/TMA functionalized MWCNTs. The XPS spectrum of uncoated MWCNTs shown in figure 7.12a displayed a distinct C-1s peak with a full width half maximum (FWHM) of 1.5 eV. The XPS spectrum of Al_2O_3 ALD on untreated MWCNTs shown in figure 7.12b also displayed peaks for Al, C, and O. All of these peaks had a broader FWHM of ∼2.6 eV. This slight broadening may result from charging effects attributed to the presence of Al_2O_3 on the MWCNTs. The typical ratio for Al:O was 2:2.6 determined from the Al 2p and O 1s XPS signals. The XPS spectrum of Al_2O_3 ALD on the NO_2/TMA functionalized MWCNTs is displayed in figure 7.12c. The Al, C, and O peaks had an average FWHM of ∼2.5 eV. The typical ratio of Al:O was 2:2.7. The presence of C in the XPS spectrum exceeded the level of expected adventitious C on the surface of the Al_2O_3 film. The extra C content may result from locations where the Al_2O_3 ALD film had cracked on the MWCNTs during sample preparation.

The XPS analysis of the NO_2/TMA functionalized MWCNTs did not detect N. No N was observed for samples before or after argon sputtering. For a monolayer of NO_2 on the MWCNT surface, the expected N signal should be approximately at the XPS detection limit. However, the

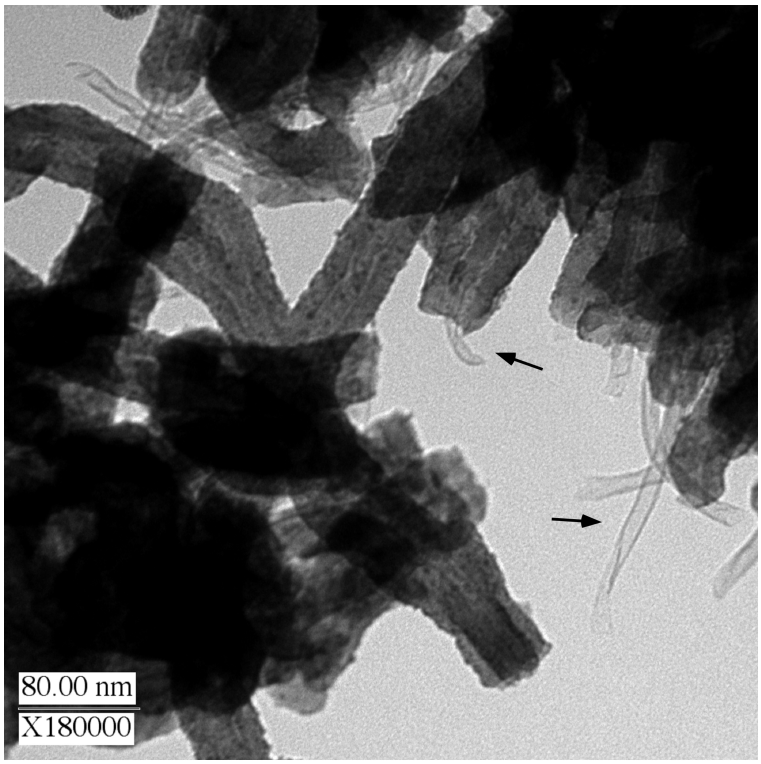

Figure 7.11: TEM image after 60 cycles of W ALD on Al_2O_3 surface prepared by NO_2/TMA functionalization and 50 AB cycles of Al_2O_3 ALD on MWCNTs.

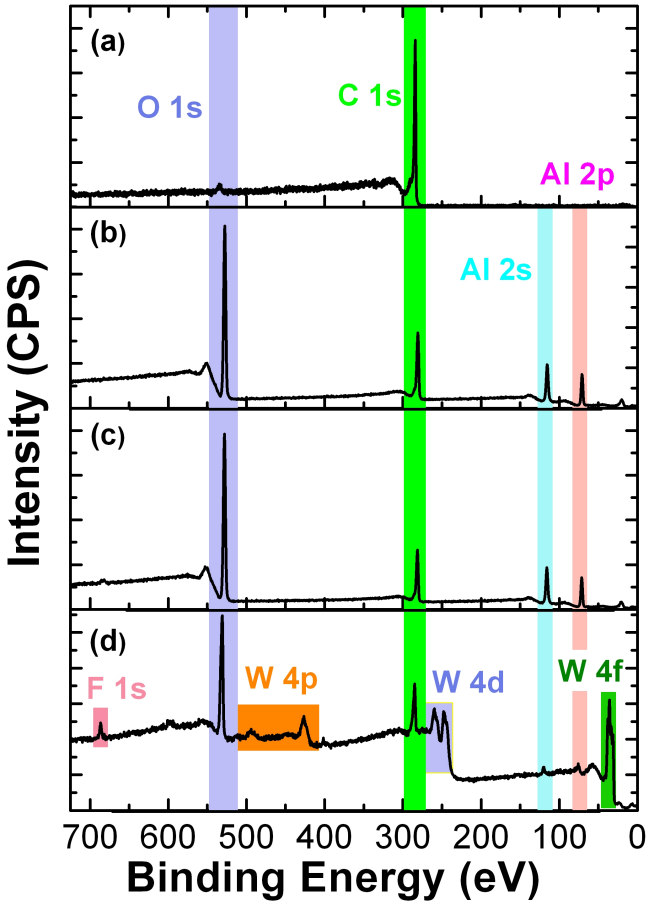

Figure 7.12: XPS scans of: (a) untreated MWCNTs; (b) Untreated MWCNT after 100 AB cycles of Al_2O_3 ALD; (c) MWCNTs after NO_2/TMA functionalization and 100 AB cycles of Al_2O_3 ALD; and (d) MWCNTs after NO_2/TMA functionalization and 50 AB cycles of Al_2O_3 ALD and 60 AB cycles of W ALD.

NO_2 molecules may also desorb from the surface of the MWCNTs. This NO_2 desorption may occur after the Al_2O_3 ALD films crack on the MWCNTs during mechanical agitation in the rotary reactor at 180 ℃.

The XPS spectrum of the W/Al_2O_3 bilayers on the MWCNTs is shown in figure 7.12d. This spectrum reveals Al, C, O and W and trace quantities of F and Si. F was present at less than 2 at.% and Si was observed in trace amounts at the noise limit. The W $4f_{5/2}$ and W $4f_{7/2}$ XPS signals were also examined in more detail at 30-40 eV as displayed in figure 7.13. The presence of a quadruplet instead of a doublet for W $4f_{5/2}$ and W $4f_{7/2}$ indicates the existence of a WO_x film in combination with metallic W.

The WO_x layer on the W ALD film occurs because tungsten metal is not stable in air. When the W/Al_2O_3/MWCNT samples were removed from the rotary reactor and exposed to atmosphere, a tungsten oxide layer forms on the surface of the W ALD film. After accounting for O bonded to Al, the W:O ratio of 1:3.1 was determined from the WO_3 4f and O 1s XPS signals. This ratio is consistent with tungsten oxidizing to WO_3. An Al_2O_3 ALD coating on top of the W ALD could serve to passivate the W ALD film and prevent the W film oxidation in atmosphere.

Models for determining film thickness from XPS analysis rely on smooth, flat samples for accurate measurements [53]. The entangled cluster agglomerates of coated MWCNTs are more like a powder sample. Models can be employed that were developed for analyzing the XPS signals from powder samples. Based on these models [53], the thickness of the WO_3 from XPS measurements is estimated to be ~10-25 Å. This thickness is close to previously reported values for the thickness of WO_3 on W ALD surfaces [207, 206].

A schematic of a W/Al_2O_3 bilayer on a CNT is shown in figure 7.14. An additional insulating Al_2O_3 ALD film on this W/Al_2O_3 bilayer would produce a nanocoaxial cable [90]. The CNT is the center conductor, the Al_2O_3 ALD layers are insulators and the W ALD layer is the metallic shield. These nanocoaxial cables may be useful as electrical nanoprobes. Similar nanocoaxial cables have been fabricated by sputtering Al_2O_3 and Cr on vertically-aligned MWCNTs and then coating with spin-on glass [164]. The W ALD film thickness in the W/Al_2O_3 bilayer can also be increased to

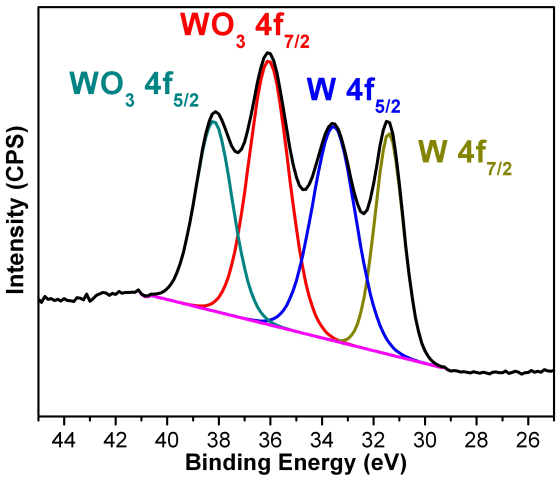

Figure 7.13: XPS scan of the W 4f peak after 60 AB cycles of W ALD on NO_2/TMA functionalized MWCNTs with 50 AB cycles of Al_2O_3 ALD.

decrease the resistance of a W/Al_2O_3/CNT wire. The W ALD thickness can tune the resistance of the CNT over a wide range.

Using a four point probe technique, the resistivity of individual single-walled CNTs (SWCNT) was $< 10^{-4}$ Ω·cm for nanotubes with a diameter of 13.8 ± 2 Å [188]. From these measurements, the resistance per unit length is R/L < 167 Ω·nm^{-1}. In comparison, W metal has a resistivity of 5.44×10^{-6} Ω·cm [202]. Assuming a SWCNT with a diameter of 13.8 Å and R/L = 167 Ω·nm^{-1}, figure 7.15 compares the resistance per unit length for a bare SWCNT and a SWCNT coated with various W thicknesses. For the W-coated SWCNT, the resistance per unit length is progressively reduced versus W thickness. The resistance per unit length is reduced by almost two orders of magnitude with a W thickness of only ∼10 Å. Note that the calculations did not account for W oxidation or electron scattering at the surface or grain-boundaries [163, 222]. Figure 7.15 serves to illustrate the ability of thin metal films to reduce significantly the resistance of CNTs.

7.5 Conclusions

Atomic layer deposition (ALD) was performed on quantities of multiwalled carbon nanotubes (MWCNTs) in a rotary reactor. The uncoated and ALD-coated MWCNTs were characterized with transmission electron microscopy and X-ray photoelectron spectroscopy. Al_2O_3 ALD grew as nanospheres on quantities of untreated MWCNTs because of nucleation difficulties. After the NO_2/TMA nucleation treatment, the Al_2O_3 ALD film grew conformally on the MWCNTs. In addition, the coaxial Al_2O_3 ALD growth on the MWCNTs was approximately linear versus the number of Al_2O_3 ALD reaction cycles.

The Al_2O_3 ALD films were observed to crack on the MWCNTs. More cracking was monitored after crushing and increased mechanical agitation. The coaxial Al_2O_3 ALD films were observed to slide on the surface of the MWCNTs and expose regions of bare MWCNTs. This ease in sliding after cracking of the Al_2O_3 ALD film is consistent with a noncovalently bonded Al_2O_3 ALD film. The Al_2O_3 ALD film also served as a foundation for coaxial W ALD film growth on the MWCNTs. XPS analysis indicated that the W/Al_2O_3 bilayer on the MWCNTs was covered with a native

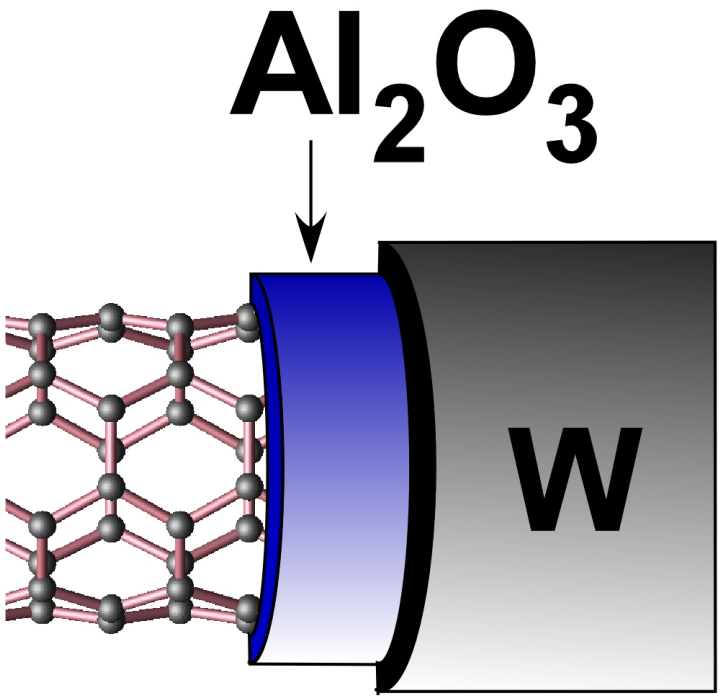

Figure 7.14: Schematic of coaxial W/Al_2O_3 bilayer on CNT.

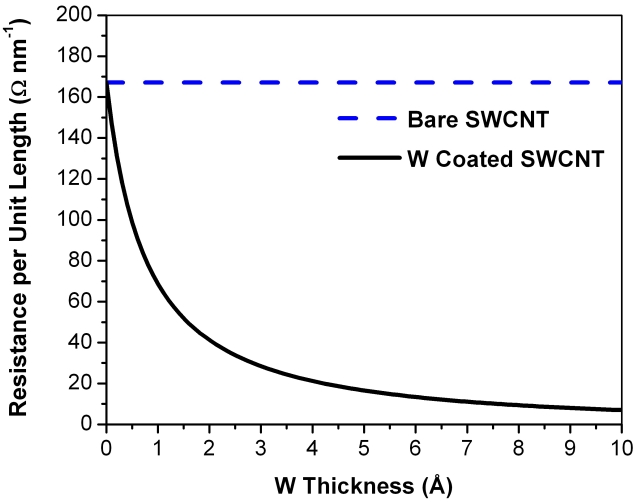

Figure 7.15: Resistance per unit length for W-coated SWCNT versus W thickness and bare SWCNT.

WO_3 layer. This WO_3 layer results from the exposure of the W ALD film to atmosphere. The coaxial W ALD film growth on the MWCNTs should significantly reduce the resistance of the W/Al_2O_3/MWCNT wire.

7.6 Acknowledgements

This research was initially supported by a subcontract from an NSF Phase I SBIR grant to ALD NanoSolutions, Inc. (Broomfield, Colorado). Subsequent support was provided by the DARPA N/MEMS S and T Fundamentals Program (Award No: HR0011-06-1-0048) at the University of Colorado. The authors thank Dr. Tom Giddings for his assistance with the TEM. The authors also thank Dr. Jarod A. McCormick and Dr. Arrelaine A. Dameron for helpful discussions.

Bibliography

[1] HSC Chemistry, 5.11 edition; Outokumpu Research Oy: Pori, Finland. Values are given at 273 K.

[2] Idaho national laboratory website, battery test manual for plug-in hybrid electric vehicle. page http://www.inl.gov.

[3] Key world energy statistics. Technical report, International Energy Agency, 2010.

[4] C.H. Ahn, B. Anczykowski, M.Z. Atashbar, W. Bacsa, W.S. Bainbridge, A. Baldi, P.D. Barnes, J. Batteas, R. Bennewitz, and B Bhushan. Springer Handbook of Nanotechnology. Springer, New York, 2nd edition, 2007.

[5] V. B. Aleskovskii. Chemistry and technology of solids. Journal of Applied Chemistry of the Ussr, 47(10):2207–2217, 1974.

[6] G. Amatucci, A. Du Pasquier, A. Blyr, T. Zheng, and J. M. Tarascon. The elevated temperature performance of the $LiMn_2O_2$/C system: Failure and solutions. Electrochimica Acta, 45(1-2):255–271, 1999.

[7] A. S. Andersson, B. Kalska, L. Haggstrom, and J. O. Thomas. Lithium extraction/insertion in $LiFePO_4$: An X-ray diffraction and mossbauer spectroscopy study. Solid State Ionics, 130(1-2):41–52, 2000.

[8] A. T. Appapillai, A. N. Mansour, J. Cho, and Y. Shao-Horn. Microstructure of $LiCoO_2$ with and without $AlPO_4$ nanoparticle coating: Combined STEM and XPS studies. Chemistry of Materials, 19(23):5748–5757, 2007.

[9] M. Arakawa and J. I. Yamaki. The cathodic decomposition of propylene carbonate in lithium batteries. Journal of Electroanalytical Chemistry, 219(1-2):273–280, 1987.

[10] C. Argile and G. E. Rhead. Adsorbed layer and thin-film growth modes monitored by Auger-electron spectroscopy. Surface Science Reports, 10(6-7):277–356, 1989.

[11] M. Armand and J. M. Tarascon. Building better batteries. Nature, 451(7179):652–657, 2008.

[12] A. R. Armstrong, M. Holzapfel, P. Novak, C. S. Johnson, S. H. Kang, M. M. Thackeray, and P. G. Bruce. Demonstrating oxygen loss and associated structural reorganization in the lithium battery cathode $Li(Ni_{0.2}Li_{0.2}Mn_{0.6})O_2$. Journal of the American Chemical Society, 128(26):8694–8698, 2006.

[13] D. Arumugam and G. P. Kalaignan. Synthesis and electrochemical characterizations of nano-SiO_2-coated $LiMn_2O_4$ cathode materials for rechargeable lithium batteries. Journal of Electroanalytical Chemistry, 624(1-2):197–204, 2008.

[14] Scribner Associates. ZView Help Manual. Scribner Associates Inc., Southern Pines.

[15] J. M. Atebamba, J. Moskon, S. Pejovnik, and M. Gaberscek. On the interpretation of measured impedance spectra of insertion cathodes for lithium-ion batteries. Journal of the Electrochemical Society, 157(11):A1218–A1228, 2010.

[16] D. Aurbach, Y. Ein-Eli, O. Chusid, Y. Cameli, M. Babai, and Y. Yamin. The correlation between the surface chemistry and the performance of Li-carbon intercalation anodes for rechargeable rocking-chair type batteries. Journal of the Electrochemical Society, 141:603–611, 1994.

[17] D. Aurbach, Y. Eineli, B. Markovsky, A. Zaban, S. Luski, Y. Carmeli, and H. Yamin. The study of electrolyte-solutions based on ethylene and diethyl carbonates for rechargeable Li batteries. 2. Graphite-electrodes. Journal of the Electrochemical Society, 142(9):2882–2890, 1995.

[18] D. R. Baer, M. H. Engelhard, A. S. Lea, P. Nachimuthu, T. C. Droubay, J. Kim, B. Lee, C. Mathews, R. L. Opila, L. V. Saraf, W. F. Stickle, R. M. Wallace, and B. S. Wright. Comparison of the sputter rates of oxide films relative to the sputter rate of SiO_2. Journal of Vacuum Science & Technology A, 28(5):1060–1072, 2010.

[19] J. L. Bahr and J. M. Tour. Highly functionalized carbon nanotubes using in situ generated diazonium compounds. Chemistry of Materials, 13(11):3823–3824, 2001.

[20] Y. Bai, N. Liu, J. Y. Liu, Z. X. Wang, and L. Q. Chen. Coating material-induced acidic electrolyte improves $LiCoO_2$ performances. Electrochemical and Solid State Letters, 9(12):A552–A556, 2006.

[21] P. G. Balakrishnan, R. Ramesh, and T. P. Kumar. Safety mechanisms in lithium-ion batteries. Journal of Power Sources, 155(2):401–414, 2006.

[22] P.B. Balbuena and Wang Y. Lithium-Ion Batteries: Solid-Electrolyte Interphase. Imperial College Press, London, 2004.

[23] R. H. Baughman, A. A. Zakhidov, and W. A. de Heer. Carbon nanotubes - The route toward applications. Science, 297(5582):787–792, 2002.

[24] I. Belharouak, C. Johnson, and K. Amine. Synthesis and electrochemical analysis of vapor-deposited carbon-coated $LiFePO_4$. Electrochemistry Communications, 7(10):983–988, 2005.

[25] S. Berber, Y. K. Kwon, and D. Tomanek. Unusually high thermal conductivity of carbon nanotubes. Physical Review Letters, 84(20):4613–4616, 2000.

[26] J. Biener, T. F. Baumann, Y. M. Wang, E. J. Nelson, S. O. Kucheyev, A. V. Hamza, M. Kemell, M. Ritala, and M. Leskela. Ruthenium/aerogel nanocomposites via atomic layer deposition. Nanotechnology, 18(5), 2007.

[27] J. P. Bonnelle, J. Grimblot, and A. Dhuysser. Influence of polarization of bonds on ESCA spectra of cobalt oxides. Journal of Electron Spectroscopy and Related Phenomena, 7(2):151–162, 1975.

[28] O. Breuer and U. Sundararaj. Big returns from small fibers: A review of polymer/carbon nanotube composites. Polymer Composites, 25(6):630–645, 2004.

[29] M. H. Brooker and J. B. Bates. Raman and infrared spectral studies of anhydrous Li_2CO_3 and Na_2CO_3. Journal of Chemical Physics, 54(11):4788–4796, 1971.

[30] A. F. Burke. Batteries and ultracapacitors for electric, hybrid, and fuel cell vehicles. Proceedings of the IEEE, 95(4):806–820, 2007.

[31] B. B. Burton, S. W. Kang, S. W. Rhee, and S. M. George. SiO_2 atomic layer deposition using tris(dimethylamino)silane and hydrogen peroxide studied by in situ transmission FTIR spectroscopy. Journal of Physical Chemistry C, 113(19):8249–8257, 2009.

[32] Q. Cao, M. G. Xia, M. Shim, and J. A. Rogers. Bilayer organic-inorganic gate dielectrics for high-performance, low-voltage, single-walled carbon nanotube thin-film transistors, complementary logic gates, and p-n diodes on plastic substrates. Advanced Functional Materials, 16(18):2355–2362, 2006.

[33] Q. Cao, H. P. Zhang, G. J. Wang, Q. Xia, Y. P. Wu, and H. Q. Wu. A novel carbon-coated $LiCoO_2$ as cathode material for lithium ion battery. Electrochemistry Communications, 9(5):1228–1232, 2007.

[34] J. A. Carpenter, J. Gibbs, A. A. Pesaran, L. D. Marlino, and K. Kelly. Road transportation vehicles. MRS Bulletin, 33(4):439–444, 2008.

[35] A. S. Cavanagh, C. A. Wilson, A. W. Weimer, and S. M. George. Atomic layer deposition on gram quantities of multi-walled carbon nanotubes. Nanotechnology, 20(25), 2009.

[36] Andrew S. Cavanagh, Younghee Lee, Byunghoon Yoon, and Steven George. Atomic layer deposition of LiOH and Li_2CO_3 using lithium t-butoxide as the lithium source. ECS Transactions, 33(2):223–229, 2010.

[37] Z. Chen and J. R. Dahn. Improving the capacity retention of $LiCoO_2$ cycled to 4.5 V by heat-treatment. Electrochemical and Solid State Letters, 7(1):A11–A14, 2004.

[38] Z. H. Chen and J. R. Dahn. Reducing carbon in $LiFePO_4$/C composite electrodes to maximize specific energy, volumetric energy, and tap density. Journal of the Electrochemical Society, 149(9):A1184–A1189, 2002.

[39] Z. H. Chen and J. R. Dahn. Studies of $LiCoO_2$ coated with metal oxides. Electrochemical and Solid State Letters, 6(11):A221–A224, 2003.

[40] Z. H. Chen, Y. Qin, K. Amine, and Y. K. Sun. Role of surface coating on cathode materials for lithium-ion batteries. Journal of Materials Chemistry, 20(36):7606–7612, 2010.

[41] I. H. Cho, S. S. Kim, S. C. Shin, and N. S. Choi. Effect of SEI on capacity losses of spinel lithium manganese oxide/graphite batteries stored at 60 ℃. Electrochemical and Solid State Letters, 13(11):A168–A172, 2010.

[42] J. Cho. Dependence of $AlPO_4$ coating thickness on overcharge behaviour of $LiCoO_2$ cathode material at 1 and 2 C rates. Journal of Power Sources, 126(1-2):186–189, 2004.

[43] J. Cho, H. Kim, and B. Park. Comparison of overcharge behavior of $AlPO_4$-coated $LiCoO_2$ and $LiNi_{0.8}Co_{0.1}Mn_{0.1}O_2$ cathode materials in Li-ion cells. Journal of the Electrochemical Society, 151(10):A1707–A1711, 2004.

[44] J. Cho, Y. J. Kim, T. J. Kim, and B. Park. Zero-strain intercalation cathode for rechargeable Li-ion cell. Angewandte Chemie-International Edition, 40(18):3367–+, 2001.

[45] J. Cho, Y. J. Kim, and B. Park. Novel $LiCoO_2$ cathode material with Al_2O_3 coating for a Li ion cell. Chemistry of Materials, 12(12):3788–3791, 2000.

[46] J. Cho, Y. J. Kim, and B. Park. $LiCoO_2$ cathode material that does not show a phase transition from hexagonal to monoclinic phase. Journal of the Electrochemical Society, 148(10):A1110–A1115, 2001.

[47] J. Cho, Y. W. Kim, B. Kim, J. G. Lee, and B. Park. A breakthrough in the safety of lithium secondary batteries by coating the cathode material with $AlPO_4$ nanoparticles. Angewandte Chemie-International Edition, 42(14):1618–1621, 2003.

[48] K. L. Choy. Chemical vapour deposition of coatings. Progress in Materials Science, 48(2):57–170, 2003.

[49] J. N. Coleman, U. Khan, W. J. Blau, and Y. K. Gun'ko. Small but strong: A review of the mechanical properties of carbon nanotube-polymer composites. Carbon, 44(9):1624–1652, 2006.

[50] S. Contarini and J. W. Rabalais. Ion bombardment-induced decomposition of Li and Ba sulfates and carbonates studied by X-ray photoelectron-spectroscopy. Journal of Electron Spectroscopy and Related Phenomena, 35(3-4):191–201, 1985.

[51] J. P. Contour, A. Salesse, M. Froment, M. Garreau, J. Thevenin, and D. Warin. Analysis by electron-microscopy and XPS of lithium surfaces polarized in anhydrous organic electrolytes. Journal De Microscopie Et De Spectroscopie Electroniques, 4(4):483–491, 1979.

[52] F. Croce, G. B. Appetecchi, L. Persi, and B. Scrosati. Nanocomposite polymer electrolytes for lithium batteries. Nature, 394(6692):456–458, 1998.

[53] P. J. Cumpson. The thickogram: A method for easy film thickness measurement in XPS. Surface and Interface Analysis, 29(6):403–406, 2000.

[54] H. J. Dai, J. H. Hafner, A. G. Rinzler, D. T. Colbert, and R. E. Smalley. Nanotubes as nanoprobes in scanning probe microscopy. Nature, 384(6605):147–150, 1996.

[55] A. A. Dameron, D. Seghete, B. B. Burton, S. D. Davidson, A. S. Cavanagh, J. A. Bertrand, and S. M. George. Molecular layer deposition of alucone polymer films using trimethylaluminum and ethylene glycol. Chemistry of Materials, 20(10):3315–3326, 2008.

[56] W. A. Deheer, A. Chatelain, and D. Ugarte. A carbon nanotube field-emission electron source. Science, 270(5239):1179–1180, 1995.

[57] A. N. Dey and B. P. Sullivan. Electrochemical decomposition of propylene carbonate on graphite. Journal of the Electrochemical Society, 117(2):222–224, 1970.

[58] A. C. Dillon, A. W. Ott, J. D. Way, and S. M. George. Surface-chemistry of Al_2O_3 deposition using $Al(CH_3)_3$ and H_2O in a binary reaction sequence. Surface Science, 322(1-3):230–242, 1995.

[59] T. Doi, L. Zhao, M. Zhou, S. Okada, and J. Yamaki. Quantitative studies on the thermal stability of the interface between graphite electrode and electrolyte. Journal of Power Sources, 185(2):1380–1385, 2008.

[60] M. Dolle, S. Grugeon, B. Beaudoin, L. Dupont, and J. M. Tarascon. In situ TEM study of the interface carbon/electrolyte. Journal of Power Sources, 97-8:104–106, 2001.

[61] J. W. Elam and S. M. George. Growth of ZnO/Al_2O_3 alloy films using atomic layer deposition techniques. Chemistry of Materials, 15(4):1020–1028, 2003.

[62] J. W. Elam, M. D. Groner, and S. M. George. Viscous flow reactor with quartz crystal microbalance for thin film growth by atomic layer deposition. Review of Scientific Instruments, 73(8):2981–2987, 2002.

[63] J. W. Elam, D. Routkevitch, and S. M. George. Properties of ZnO/Al_2O_3 alloy films grown using atomic layer deposition techniques. Journal of the Electrochemical Society, 150(6):G339–G347, 2003.

[64] J. W. Elam, D. Routkevitch, P. P. Mardilovich, and S. M. George. Conformal coating on ultrahigh-aspect-ratio nanopores of anodic alumina by atomic layer deposition. Chemistry of Materials, 15(18):3507–3517, 2003.

[65] F. H. Fabreguette, Z. A. Sechrist, J. W. Elam, and S. M. George. Quartz crystal microbalance study of tungsten atomic layer deposition using WF_6 and Si_2H_6. Thin Solid Films, 488(1-2):103–110, 2005.

[66] F. H. Fabreguette, R. A. Wind, and S. M. George. Ultrahigh X-ray reflectivity from W/Al_2O_3 multilayers fabricated using atomic layer deposition. Applied Physics Letters, 88(1):013116, 2006.

[67] T. Fang, J. G. Duh, and S. R. Sheen. Improving the electrochemical performance of $LiCoO_2$ cathode by nanocrystalline ZnO coating. Journal of the Electrochemical Society, 152(9):A1701–A1706, 2005.

[68] D. B. Farmer and R. G. Gordon. ALD of high-kappa dielectrics on suspended functionalized SWNTs. Electrochemical and Solid State Letters, 8(4):G89–G91, 2005.

[69] D. B. Farmer and R. G. Gordon. Atomic layer deposition on suspended single-walled carbon nanotubes via gas-phase noncovalent functionalization. Nano Letters, 6(4):699–703, 2006.

[70] J. D. Ferguson, A. W. Weimer, and S. M. George. Atomic layer deposition of ultrathin and conformal Al_2O_3 films on BN particles. Thin Solid Films, 371(1-2):95–104, 2000.

[71] J. D. Ferguson, A. R. Yoder, A. W. Weimer, and S. M. George. TiO_2 atomic layer deposition on ZrO2 particles using alternating exposures of $TiCl_4$ and H_2O. Applied Surface Science, 226(4):393–404, 2004.

[72] M. Feygin and R. Satkin. The oil reserves-to-production ratio and its proper interpretation. Natural Resources Research, 13(1):57–60, 2004.

[73] S. Flandrois and B. Simon. Carbon materials for lithium-ion rechargeable batteries. Carbon, 37(2):165–180, 1999.

[74] R. Fong, U. von Sacken, and J. R. Dahn. Studies of lithium intercalation into carbons using nonaqueous electrochemical cells. Journal of the Electrochemical Society, 137(7):2009–2013, 1990.

[75] S. Frank, P. Poncharal, Z. L. Wang, and W. A. de Heer. Carbon nanotube quantum resistors. Science, 280(5370):1744–1746, 1998.

[76] L. J. Fu, H. Liu, C. Li, Y. P. Wu, E. Rahm, R. Holze, and H. Q. Wu. Surface modifications of electrode materials for lithium ion batteries. Solid State Sciences, 8(2):113–128, 2006.

[77] M. Fujimoto, Y. Shoji, Y. Kida, R. Ohshita, T. Nohma, and K. Nishio. Influence of solvent species on the charge-discharge characteristics of a natural graphite electrode. Journal of Power Sources, 72(2):226–230, 1998.

[78] S. M. George. Atomic layer deposition: An overview. Chemical Reviews, 110(1):111–131, 2010.

[79] S. M. George, A. W. Ott, and J. W. Klaus. Surface chemistry for atomic layer growth. Journal of Physical Chemistry, 100(31):13121–13131, 1996.

[80] S. M. George, B. Yoon, and A. A. Dameron. Surface chemistry for molecular layer deposition of organic and hybrid organic-inorganic polymers. Accounts of Chemical Research, 42(4):498–508, 2009.

[81] J. B. Goodenough and Y. Kim. Challenges for rechargeable Li batteries. Chemistry of Materials, 22(3):587–603, 2010.

[82] J. M. Green, L. F. Dong, T. Gutu, J. Jiao, J. F. Conley, and Y. Ono. ZnO-nanoparticle-coated carbon nanotubes demonstrating enhanced electron field-emission properties. Journal of Applied Physics., 99(9):094308, 2006.

[83] M. D. Groner, J. W. Elam, F. H. Fabreguette, and S. M. George. Electrical characterization of thin Al_2O_3 films grown by atomic layer deposition on silicon and various metal substrates. Thin Solid Films, 413(1-2):186–197, 2002.

[84] M. D. Groner, F. H. Fabreguette, J. W. Elam, and S. M. George. Low-temperature Al_2O_3 atomic layer deposition. Chemistry of Materials, 16(4):639–645, 2004.

[85] N. Grossiord, J. Loos, O. Regev, and C. E. Koning. Toolbox for dispersing carbon nanotubes into polymers to get conductive nanocomposites. Chemistry of Materials, 18(5):1089–1099, 2006.

[86] R. K. Grubbs, C. E. Nelson, N. J. Steinmetz, and S. M. George. Nucleation and growth during the atomic layer deposition of W on Al_2O_3 and Al_2O_3 on W. Thin Solid Films, 467(1-2):16–27, 2004.

[87] R. K. Grubbs, N. J. Steinmetz, and S. M. George. Gas phase reaction products during tungsten atomic layer deposition using WF_6 and Si_2H_6. Journal of Vacuum Science & Technology B, 22(4):1811–1821, 2004.

[88] U. Heider, R. Oesten, and M. Jungnitz. Challenge in manufacturing electrolyte solutions for lithium and lithium ion batteries quality control and minimizing contamination level. Journal of Power Sources, 81:119–122, 1999.

[89] K. Hernadi, A. Fonseca, J. B. Nagy, D. Bernaerts, A. Fudala, and A. A. Lucas. Catalytic synthesis of carbon nanotubes using zeolite support. Zeolites, 17(5-6):416–423, 1996.

[90] C. F. Herrmann, F. H. Fabreguette, D. S. Finch, R. Geiss, and S. M. George. Multilayer and functional coatings on carbon nanotubes using atomic layer deposition. Applied Physics Letters, 87(12):123110, 2005.

[91] J. M. Hill, D. G. Royce, C. S. Fadley, L. F. Wagner, and F. J. Grunthaner. Properties of oxidized silicon as determined by angular-dependent X-ray photoelectron-spectroscopy. Chemical Physics Letters, 44(2):225–231, 1976.

[92] R. Imhof and P. Novak. In situ investigation of the electrochemical reduction of carbonate electrolyte solutions at graphite electrodes. Journal of the Electrochemical Society, 145(4):1081–1087, 1998.

[93] Y. Iriyama, H. Kurita, I. Yamada, T. Abe, and Z. Ogumi. Efffects of surface modification by MgO on interfacial reactions of lithium cobalt oxide thin film electrode. Journal of Power Sources, 137(1):111–116, 2004.

[94] J. R. Jaunsen. Behavior and capabilities of lithium hydroxide carbon dioxide scrubbers in a deep sea environment. Technical report, 1989.

[95] A. Javey, H. Kim, M. Brink, Q. Wang, A. Ural, J. Guo, P. McIntyre, P. McEuen, M. Lundstrom, and H. J. Dai. High-kappa dielectrics for advanced carbon-nanotube transistors and logic gates. Nature Materials., 1(4):241–246, 2002.

[96] S. Jeon, S. Bang, S. Lee, S. Kwon, W. Jeong, H. Jeon, H. J. Chang, and H. H. Park. Structural and electrical properties of ZnO thin films deposited by atomic layer deposition at low temperatures. Journal of the Electrochemical Society, 155(10):H738–H743, 2008.

[97] L. H. Jones. The infrared spectra and structure of LiOH, $LiOH{\cdot}H_2O$ and the deuterium species - remark on fundamental frequency of OH. Journal of Chemical Physics, 22(2):217–219, 1954.

[98] Y. S. Jung, A. S. Cavanagh, A. C. Dillon, M. D. Groner, S. M. George, and S. H. Lee. Enhanced stability of $LiCoO_2$ cathodes in lithium-ion batteries using surface modification by atomic layer deposition. Journal of the Electrochemical Society, 157(1):A75–A81, 2010.

[99] Y. S. Jung, A. S. Cavanagh, L. A. Riley, S. H. Kang, A. C. Dillon, M. D. Groner, S. M. George, and S. H. Lee. Ultrathin direct atomic layer deposition on composite electrodes for highly durable and safe Li-ion batteries. Advanced Materials, 22(19):2172–+, 2010.

[100] T. Kawamura, S. Okada, and J. Yamaki. Decomposition reaction of $LiPF_6$-based electrolytes for lithium ion cells. Journal of Power Sources, 156(2):547–554, 2006.

[101] W. Kempton and J. Tomic. Vehicle-to-grid power implementation: From stabilizing the grid to supporting large-scale renewable energy. Journal of Power Sources, 144(1):280–294, 2005.

[102] B. Kim, C. Kim, T. G. Kim, D. Ahn, and B. Park. The effect of $AlPO_4$-coating layer on the electrochemical properties in $LiCoO_2$ thin films. Journal of the Electrochemical Society, 153(9):A1773–A1777, 2006.

[103] H. Kim. Atomic layer deposition of metal and nitride thin films: Current research efforts and applications for semiconductor device processing. Journal of Vacuum Science & Technology B, 21(6):2231–2261, 2003.

[104] S. S. Kim, Y. Kadoma, H. Ikuta, Y. Uchimoto, and M. Wakihara. Electrochemical performance of natural graphite by surface modification using aluminum. Electrochemical and Solid State Letters, 4(8):A109–A112, 2001.

[105] W. S. Kim, K. I. Chung, J. H. Cho, D. W. Park, C. Y. Kim, and Y. K. Choi. Studies of a solid electrolyte interface coated with Li_2CO_3 on the carbon electrode in Li-ion batteries. Journal of Industrial and Engineering Chemistry, 9(6):699–703, 2003.

[106] Y. J. Kim, J. P. Cho, T. J. Kim, and B. Park. Suppression of cobalt dissolution from the $LiCoO_2$ cathodes with various metal-oxide coatings. Journal of the Electrochemical Society, 150(12):A1723–A1725, 2003.

[107] Y. J. Kim, H. Kim, B. Kim, D. Ahn, J. G. Lee, T. J. Kim, D. Son, J. Cho, Y. W. Kim, and B. Park. Electrochemical stability of thin-film $LiCoO_2$ cathodes by aluminum-oxide coating. Chemistry of Materials, 15(7):1505–1511, 2003.

[108] Y. J. Kim, T. J. Kim, J. W. Shin, B. Park, and J. P. Cho. The effect of Al_2O_3 coating on the cycle life performance in thin-film $LiCoO_2$ cathodes. Journal of the Electrochemical Society, 149(10):A1337–A1341, 2002.

[109] J. S. King, D. Heineman, E. Graugnard, and C. J. Summers. Atomic layer deposition in porous structures: 3D photonic crystals. Applied Surface Science, 244(1-4):511–516, 2005.

[110] J. W. Klaus, S. J. Ferro, and S. M. George. Atomic layer deposition of tungsten using sequential surface chemistry with a sacrificial stripping reaction. Thin Solid Films, 360(1-2):145–153, 2000.

[111] M. Knez, K. Niesch, and L. Niinisto. Synthesis and surface engineering of complex nanostructures by atomic layer deposition. Advanced Materials, 19(21):3425–3438, 2007.

[112] S. Komaba, N. Kumagai, and Y. Kataoka. Influence of manganese(II), cobalt(II), and nickel(II) additives in electrolyte on performance of graphite anode for lithium-ion batteries. Electrochimica Acta, 47(8):1229–1239, 2002.

[113] F. Kong, R. Kostecki, G. Nadeau, X. Song, K. Zaghib, K. Kinoshita, and F. McLarnon. In situ studies of SEI formation. Journal of Power Sources, 97-8:58–66, 2001.

[114] J. Kong, N. R. Franklin, C. W. Zhou, M. G. Chapline, S. Peng, K. J. Cho, and H. J. Dai. Nanotube molecular wires as chemical sensors. Science, 287(5453):622–625, 2000.

[115] N. Kosova, E. Devyatkina, A. Slobodyuk, and V. Kaichev. Surface chemistry study of $LiCoO_2$ coated with alumina. Solid State Ionics, 179(27-32):1745–1749, 2008.

[116] I. R. M. Kottegoda, Y. Kadoma, H. Ikuta, Y. Uchimoto, and M. Wakihara. Enhancement of rate capability in graphite anode by surface modification with zirconia. Electrochemical and Solid State Letters, 5(12):A275–A278, 2002.

[117] I. R. M. Kottegoda, Y. Kadoma, H. Ikuta, Y. Uchimoto, and M. Wakihara. High-rate-capable lithium-ion battery based on surface-modified natural graphite anode and substituted spinel cathode for hybrid electric vehicles. Journal of the Electrochemical Society, 152(8):A1595–A1599, 2005.

[118] K. Kukli, K. Forsgren, J. Aarik, T. Uustare, A. Aidla, A. Niskanen, M. Ritala, M. Leskela, and A. Harsta. Atomic layer deposition of zirconium oxide from zirconium tetraiodide, water and hydrogen peroxide. Journal of Crystal Growth, 231(1-2):262–272, 2001.

[119] I. Kuribayashi, M. Yokoyama, and M. Yamashita. Battery characteristics with various carbonaceous materials. Journal of Power Sources, 54(1):1–5, 1995.

[120] H. J. Kweon, J. Park, J. Seo, G. Kim, B. Jung, and H. S. Lim. Effects of metal oxide coatings on the thermal stability and electrical performance of $LiCoO_2$ in a li-ion cell. Journal of Power Sources, 126(1-2):156–162, 2004.

[121] K. T. Lau, C. Gu, and D. Hui. A critical review on nanotube and nanotube/nanoclay related polymer composite materials. Composites Part B, 37(6):425–436, 2006.

[122] J. G. Lee, B. Kim, J. Cho, Y. W. Kim, and B. Park. Effect of $AlPO_4$-nanoparticle coating concentration on high-cutoff-voltage electrochemical performances in $LiCoO_2$. Journal of the Electrochemical Society, 151(6):A801–A805, 2004.

[123] S. E. Lee, E. Kim, and J. P. Cho. Improvement of electrochemical properties of natural graphite anode materials with an ovoid morphology by $AlPO_4$ coating. Electrochemical and Solid State Letters, 10(1):A1–A4, 2007.

[124] S. H. Lee, Y. H. Kim, R. Deshpande, P. A. Parilla, E. Whitney, D. T. Gillaspie, K. M. Jones, A. H. Mahan, S. B. Zhang, and A. C. Dillon. Reversible lithium-ion insertion in molybdenum oxide nanoparticles. Advanced Materials, 20(19):3627–+, 2008.

[125] M. Leskela and M. Ritala. Atomic layer deposition (ALD): From precursors to thin film structures. Thin Solid Films, 409(1):138–146, 2002.

[126] M. D. Levi and D. Aurbach. Simultaneous measurements and modeling of the electrochemical impedance and the cyclic voltammetric characteristics of graphite electrodes doped with lithium. Journal of Physical Chemistry B, 101(23):4630–4640, 1997.

[127] M. D. Levi, G. Salitra, B. Markovsky, H. Teller, D. Aurbach, U. Heider, and L. Heider. Solid-state electrochemical kinetics of Li-ion intercalation into $Li_{1-x}CoO_2$: Simultaneous application of electroanalytical techniques SSCV, PITT, and EIS. Journal of the Electrochemical Society, 146(4):1279–1289, 1999.

[128] D. H. Levy, D. Freeman, S. F. Nelson, P. J. Cowdery-Corvan, and L. M. Irving. Stable ZnO thin film transistors by fast open air atomic layer deposition. Applied Physics Letters, 92(19):192101, 2008.

[129] C. Li, H. P. Zhang, L. J. Fu, H. Liu, Y. P. Wu, E. Ram, R. Holze, and H. Q. Wu. Cathode materials modified by surface coating for lithium ion batteries. Electrochimica Acta, 51(19):3872–3883, 2006.

[130] Y. Lin, S. Taylor, H. P. Li, K. A. S. Fernando, L. W. Qu, W. Wang, L. R. Gu, B. Zhou, and Y. P. Sun. Advances toward bioapplications of carbon nanotubes. Journal of Materials Chemistry, 14(4):527–541, 2004.

[131] H. Liu, Y. P. Wu, E. Rahm, R. Holze, and H. Q. Wu. Cathode materials for lithium ion batteries prepared by sol-gel methods. Journal of Solid State Electrochemistry, 8(7):450–466, 2004.

[132] H. S. Liu, Z. R. Zhang, Z. L. Gong, and Y. Yang. A comparative study of $LiNi_{0.8}Co_{0.2}O_2$ cathode materials modified by lattice-doping and surface-coating. Solid State Ionics, 166(3-4):317–325, 2004.

[133] J. Y. Liu, N. Liu, D. T. Liu, Y. Bai, L. H. Shi, Z. X. Wang, L. Q. Chen, V. Hennige, and A. Schuch. Improving the performances of $LiCoO_2$ cathode materials by soaking nano-alumina in commercial electrolyte. Journal of the Electrochemical Society, 154(1):A55–A63, 2007.

[134] Y. C. Lu, A. N. Mansour, N. Yabuuchi, and Y. Shao-Horn. Probing the origin of enhanced stability of $AlPO_4$ nanoparticle coated $LiCoO_2$ during cycling to high voltages: Combined XRD and XPS studies. Chemistry of Materials, 21(19):4408–4424, 2009.

[135] J. R. Macdonald. Note on the parameterization of the constant-phase admittance element. Solid State Ionics, 13(2):147–149, 1984.

[136] J. R. Macdonald. Impedance spectroscopy: Models, data fitting, and analysis. Solid State Ionics, 176(25-28):1961–1969, 2005.

[137] R. Martel, T. Schmidt, H. R. Shea, T. Hertel, and P. Avouris. Single- and multi-wall carbon nanotube field-effect transistors. Applied Physics Letters, 73(17):2447–2449, 1998.

[138] T. M. Mayer, J. W. Elam, S. M. George, P. G. Kotula, and R. S. Goeke. Atomic-layer deposition of wear-resistant coatings for microelectromechanical devices. Applied Physics Letters, 82(17):2883–2885, 2003.

[139] J. A. McCormick, B. L. Cloutier, A. W. Weimer, and S. M. George. Rotary reactor for atomic layer deposition on large quantities of nanoparticles. Journal of Vacuum Science & Technology A, 25(1):67–74, 2007.

[140] J. A. McCormick, K. P. Rice, D. F. Paul, A. W. Weimer, and S. M. George. Analysis of Al_2O_3 atomic layer deposition on ZrO_2 nanoparticles in a rotary reactor. Chemical Vapor Deposition, 13(9):491–498, 2007.

[141] G. E. McGuire, Schweitz.Gk, and T. A. Carlson. Study of core electron binding-energies in some group IIIA, VB, and VIB compounds. Inorganic Chemistry, 12(10):2450–2453, 1973.

[142] S. Menkin, D. Golodnitsky, and E. Peled. Artificial solid-electrolyte interphase (SEI) for improved cycleability and safety of lithium-ion cells for EV applications. Electrochemistry Communications, 11(9):1789–1791, 2009.

[143] D. C. Miller, R. R. Foster, S. H. Jen, J. A. Bertrand, D. Seghete, B. Yoon, Y. C. Lee, S. M. George, and M. L. Dunn. Thermomechanical properties of aluminum alkoxide (alucone) films created using molecular layer deposition. Acta Materialia, 57(17):5083–5092, 2009.

[144] M. Mladenov, R. Stoyanova, E. Zhecheva, and S. Vassilev. Effect of Mg doping and MgO-surface modification on the cycling stability of $LiCoO_2$ electrodes. Electrochemistry Communications, 3(8):410–416, 2001.

[145] S. R. Narayanan, D. H. Shen, S. Surampudi, A. I. Attia, and G. Halpert. Electrochemical impedance spectroscopy of lithium-titanium disulfide rechargeable cells. Journal of the Electrochemical Society, 140(7):1854–1861, 1993.

[146] G.A. Nazri and G. Pistoia. Lithium Batteries: Science and Technology. Kluwer Academic Publishers, Boston, 2004.

[147] L. Niinisto, J. Paivasaari, J. Niinisto, M. Putkonen, and M. Nieminen. Advanced electronic and optoelectronic materials by atomic layer deposition: An overview with special emphasis on recent progress in processing of high-k dielectrics and other oxide materials. Physica Status Solidi a-Applied Research, 201(7):1443–1452, 2004.

[148] S. Oh, J. K. Lee, D. Byun, W. I. Cho, and B. W. Cho. Effect of Al_2O_3 coating on electrochemical performance of $LiCoO_2$ as cathode materials for secondary lithium batteries. Journal of Power Sources, 132(1-2):249–255, 2004.

[149] A. W. Ott, J. W. Klaus, J. M. Johnson, and S. M. George. Al_2O_3 thin film growth on Si(100) using binary reaction sequence chemistry. Thin Solid Films, 292(1-2):135–144, 1997.

[150] E. Peled. The electrochemical-behavior of alkali and alkaline-earth metals in non-aqueous battery systems - the solid electrolyte interphase model. Journal of the Electrochemical Society, 126(12):2047–2051, 1979.

[151] E. Peled, D. Golodnitsky, and G. Ardel. Advanced model for solid electrolyte interphase electrodes in liquid and polymer electrolytes. Journal of the Electrochemical Society, 144(8):L208–L210, 1997.

[152] M. J. Pellin, P. C. Stair, G. Xiong, J. W. Elam, J. Birrell, L. Curtiss, S. M. George, C. Y. Han, L. Iton, H. Kung, M. Kung, and H. H. Wang. Mesoporous catalytic membranes: Synthetic control of pore size and wall composition. Catalysis Letters, 102(3-4):127–130, 2005.

[153] S. B. Peterson, J. Apt, and J. F. Whitacre. Lithium-ion battery cell degradation resulting from realistic vehicle and vehicle-to-grid utilization. Journal of Power Sources, 195(8):2385–2392, 2010.

[154] C.J. Powell and A. Jablonski. NIST Electron-Effective-Attenuation-Length Database, NIST SRD 82, Version 1.1. National Institute of Standards and Technology, Gaithersburg, MD, 2003.

[155] I. A. Profatilova, S. S. Kim, and N. S. Choi. Enhanced thermal properties of the solid electrolyte interphase formed on graphite in an electrolyte with fluoroethylene carbonate. Electrochimica Acta, 54(19):4445–4450, 2009.

[156] R. L. Puurunen. Surface chemistry of atomic layer deposition: A case study for the trimethylaluminum/water process. Journal of Applied Physics., 97(12):52, 2005.

[157] R. Ramasubramaniam, J. Chen, and H. Y. Liu. Homogeneous carbon nanotube/polymer composites for electrical applications. Applied Physics Letters, 83(14):2928–2930, 2003.

[158] N. Ravet, Y. Chouinard, J. F. Magnan, S. Besner, M. Gauthier, and M. Armand. Electroactivity of natural and synthetic triphylite. Journal of Power Sources, 97-8:503–507, 2001.

[159] M. N. Richard and J. R. Dahn. Accelerating rate calorimetry study on the thermal stability of lithium intercalated graphite in electrolyte I. Experimental. Journal of the Electrochemical Society, 146(6):2068–2077, 1999.

[160] L. A. Riley, A. S. Cavanagh, S. M. George, Y. S. Jung, Y. F. Yan, S. H. Lee, and A. C. Dillon. Conformal surface coatings to enable high volume expansion Li-ion anode materials. Chemphyschem, 11(10):2124–2130, 2010.

[161] M. Ritala and M. Leskela. Atomic layer deposition. In H.S. Nalwa, editor, Handbook of Thin Film Materials, volume 1. Academic Press.

[162] N. M. Rodriguez. A review of catalytically grown carbon nanofibers. Journal of Materials Research, 8(12):3233–3250, 1993.

[163] S. M. Rossnagel and T. S. Kuan. Alteration of Cu conductivity in the size effect regime. Journal of Vacuum Science & Technology B, 22(1):240–247, 2004.

[164] J. Rybczynski, K. Kempa, A. Herczynski, Y. Wang, M. J. Naughton, Z. F. Ren, Z. P. Huang, D. Cai, and M. Giersig. Subwavelength waveguide for visible light. Applied Physics Letters, 90(2):021104, 2007.

[165] J. H. Ryu, J. W. Kim, Y. E. Sung, and S. M. Oh. Failure modes of silicon powder negative electrode in lithium secondary batteries. Electrochemical and Solid State Letters, 7(10):A306–A309, 2004.

[166] H. Sato, D. Takahashi, T. Nishina, and I. Uchida. Electrochemical characterization of thin-film $LiCoO_2$ electrodes in propylene carbonate solutions. Journal of Power Sources, 68(2):540–544, 1997.

[167] I. D. Scott, Y. S. Jung, A. S. Cavanagh, Y. F. An, A. C. Dillon, S. M. George, and S. H. Lee. Ultrathin coatings on nano-$LiCoO_2$ for Li-ion vehicular applications. Nano Letters, 11(2):414–418, 2011.

[168] Z. A. Sechrist, F. H. Fabreguette, O. Heintz, T. M. Phung, D. C. Johnson, and S. M. George. Optimization and structural characterization of W/Al_2O_3 nanolaminates grown using atomic layer deposition techniques. Chemistry of Materials, 17(13):3475–3485, 2005.

[169] SIGMA-ALDRICH. MSDS, 2010.

[170] D.L. Smith. Thin Film Deposition. McGraw-Hill Inc., New York, N.Y., 1995.

[171] N. R. Smyrl, E. L. Fuller, and G. L. Powell. Monitoring the heterogeneous reaction of LiH and LiOH with H_2O and CO_2 by diffuse reflectance infrared fourier-transform spectroscopy. Applied Spectroscopy, 37(1):38–44, 1983.

[172] M. Q. Snyder, S. A. Trebukhova, B. Ravdel, M. C. Wheeler, J. DiCarlo, C. P. Tripp, and W. J. DeSisto. Synthesis and characterization of atomic layer deposited titanium nitride thin films on lithium titanate spinel powder as a lithium-ion battery anode. Journal of Power Sources, 165(1):379–385, 2007.

[173] R. Spotnitz and J. Franklin. Abuse behavior of high-power, lithium-ion cells. Journal of Power Sources, 113(1):81–100, 2003.

[174] S.E. Stein. Infrared Spectra. National Institute of Standards and Technology, Gaithersburg, MD, 2011.

[175] Y. K. Sun, S. W. Cho, S. W. Lee, C. S. Yoon, and K. Amine. AlF_3-coating to improve high voltage cycling performance of $LiNi_{1/3}Co_{1/3}Mn_{1/3}O_2$ cathode materials for lithium secondary batteries. Journal of the Electrochemical Society, 154(3):A168–A172, 2007.

[176] Y. K. Sun, J. M. Han, S. T. Myung, S. W. Lee, and K. Amine. Significant improvement of high voltage cycling behavior AlF_3-coated $LiCoO_2$ cathode. Electrochemistry Communications, 8(5):821–826, 2006.

[177] Y. K. Sun, K. J. Hong, J. Prakash, and K. Amine. Electrochemical performance of nano-sized ZnO-coated $LiNi_{0.5}Mn_{1.5}O_4$ spinel as 5 V materials at elevated temperatures. Electrochemistry Communications, 4(4):344–348, 2002.

[178] Y. K. Sun, S. T. Myung, M. H. Kim, J. Prakash, and K. Amine. Synthesis and characterization of $Li[(Ni_{0.8}Co_{0.1}Mn_{0.1})_{0.8}(Ni_{0.5}Mn_{0.5})_{0.2}]O_2$ with the microscale core-shell structure as the positive electrode material for lithium batteries. Journal of the American Chemical Society, 127(38):13411–13418, 2005.

[179] Y. K. Sun, S. T. Myung, B. C. Park, J. Prakash, I. Belharouak, and K. Amine. High-energy cathode material for long-life and safe lithium batteries. Nature Materials, 8(4):320–324, 2009.

[180] T. Suntola. Atomic Layer Epitaxy, chapter 14. Elsevier, Amsterdam, 1994.

[181] T. Suntola. Atomic layer epitaxy. In D. T. J. Hurle, editor, Handbook of Crystal Growth, Part B: Growth Mechanisms and Dynamics, volume 3. Elsevier, 1994.

[182] T. Suntola and J. Antson. Methods for producing compound thin films, 1974.

[183] B. J. Tan, K. J. Klabunde, and P. M. A. Sherwood. XPS studies of solvated metal atom dispersed catalysts - evidence for layered cobalt manganese particles on alumina and silica. Journal of the American Chemical Society, 113(3):855–861, 1991.

[184] S. J. Tans, M. H. Devoret, H. J. Dai, A. Thess, R. E. Smalley, L. J. Geerligs, and C. Dekker. Individual single-wall carbon nanotubes as quantum wires. Nature, 386(6624):474–477, 1997.

[185] J. M. Tarascon and M. Armand. Issues and challenges facing rechargeable lithium batteries. Nature, 414(6861):359–367, 2001.

[186] K. Tasaki, K. Kanda, S. Nakamura, and M. Ue. Decomposition of $LiPF_6$ and stability of PF_5 in Li-ion battery electrolytes - Density functional theory and molecular dynamics studies. Journal of the Electrochemical Society, 150(12):A1628–A1636, 2003.

[187] D. Tasis, N. Tagmatarchis, A. Bianco, and M. Prato. Chemistry of carbon nanotubes. Chemical Reveiws, 106(3):1105–1136, 2006.

[188] A. Thess, R. Lee, P. Nikolaev, H. J. Dai, P. Petit, J. Robert, C. H. Xu, Y. H. Lee, S. G. Kim, A. G. Rinzler, D. T. Colbert, G. E. Scuseria, D. Tomanek, J. E. Fischer, and R. E. Smalley. Crystalline ropes of metallic carbon nanotubes. Science, 273(5274):483–487, 1996.

[189] E. T. Thostenson, Z. F. Ren, and T. W. Chou. Advances in the science and technology of carbon nanotubes and their composites: A review. Composites Science and Technology, 61(13):1899–1912, 2001.

[190] M. M. J. Treacy, T. W. Ebbesen, and J. M. Gibson. Exceptionally high Young's modulus observed for individual carbon nanotubes. Nature, 381(6584):678–680, 1996.

[191] N. H. Turner and A. M. Single. Determination of peak positions and areas from wide-scan XPS spectra. Surface and Interface Analysis, 15(3):215–222, 1990.

[192] Umicore. $LiCoO_2$ for thin film battery applications. Nashua, NH, 2009.

[193] L.J. van der Pauw. Phillips Technical Review, 20:220, 1958.

[194] J. T. Vaughey, C. Lopez, and D. Dees. Annual merit review DOE vehicle technologies program. Technical report, Argonne National Laboratory, 2009.

[195] F. T. Wagner, B. Lakshmanan, and M. F. Mathias. Electrochemistry and the future of the automobile. Journal of Physical Chemistry Letters, 1(14):2204–2219, 2010.

[196] D. Wang and G. R. Bierwagen. Sol-gel coatings on metals for corrosion protection. Progress in Organic Coatings, 64(4):327–338, 2009.

[197] H. Y. Wang and M. Yoshio. Carbon-coated natural graphite prepared by thermal vapor decomposition process, a candidate anode material for lithium-ion battery. Journal of Power Sources, 93(1-2):123–129, 2001.

[198] H. Y. Wang, M. Yoshio, T. Abe, and Z. Ogumi. Characterization of carbon-coated natural graphite as a lithium-ion battery anode material. Journal of the Electrochemical Society, 149(4):A499–A503, 2002.

[199] Z. X. Wang, C. A. Wu, L. J. Liu, F. Wu, L. Q. Chen, and X. J. Huang. Electrochemical evaluation and structural characterization of commercial $LiCoO_2$ surfaces modified with MgO for lithium-ion batteries. Journal of the Electrochemical Society, 149(4):A466–A471, 2002.

[200] J. R. Wank, S. M. George, and A. W. Weimer. Coating fine nickel particles with Al_2O_3 utilizing an atomic layer deposition-fluidized bed reactor (ALD-FBR). Journal of the American Ceramics Society, 87(4):762–765, 2004.

[201] J. R. Wank, S. M. George, and A. W. Weimer. Nanocoating individual cohesive boron nitride particles in a fluidized bed by ALD. Powder Technology, 142(1):59–69, 2004.

[202] R.C. Weast. CRC Handbook of Chemistry and Physics. CRC Press, Inc., Boca Raton, 64th edition, 1985.

[203] M. S. Whittingham. Lithium batteries and cathode materials. Chemical Reviews, 104(10):4271–4301, 2004.

[204] D. D. Williams and R. R. Miller. Effect of water vapor on LiOH-CO_2 reaction - dynamic isothermal system. Industrial & Engineering Chemistry Fundamentals, 9(3):454–457, 1970.

[205] M. G. Willinger, G. Neri, E. Rauwel, A. Bonavita, G. Micali, and N. Pinna. Vanadium oxide sensing layer grown on carbon nanotubes by a new atomic layer deposition process. Nano Letters, 8(12):4201–4204, 2008.

[206] C. A. Wilson, D. N. Goldstein, J. A. McCormick, A. W. Weimer, and S. M. George. W ALD on cobalt nanoparticles. Journal of Vacuum Science & Technology A, 26:430, 2008.

[207] C. A. Wilson, R. K. Grubbs, and S. M. George. Nucleation and growth during Al_2O_3 atomic layer deposition on polymers. Chemistry of Materials, 17(23):5625–5634, 2005.

[208] R. A. Wind and S. M. George. Quartz crystal microbalance studies of Al_2O_3 atomic layer deposition using trimethylaluminum and water at 125 degrees C. Journal of Physical Chemistry A, 114(3):1281–1289, 2010.

[209] M. Winter, J. O. Besenhard, M. E. Spahr, and P. Novak. Insertion electrode materials for rechargeable lithium batteries. Advanced Materials, 10(10):725–763, 1998.

[210] E. W. Wong, P. E. Sheehan, and C. M. Lieber. Nanobeam mechanics: Elasticity, strength, and toughness of nanorods and nanotubes. Science, 277(5334):1971–1975, 1997.

[211] A. Yamada, B. S. Sang, and M. Konagai. Atomic layer deposition of ZnO transparent conducting oxides. Applied Surface Science, 112:216–222, 1997.

[212] H. Yang, H. Bang, K. Amine, and J. Prakash. Investigations of the exothermic reactions of natural graphite anode for Li-ion batteries during thermal runaway. Journal of the Electrochemical Society, 152(1):A73–A79, 2005.

[213] Z. G. Yang, J. L. Zhang, M. C. W. Kintner-Meyer, X. C. Lu, D. W. Choi, J. P. Lemmon, and J. Liu. Electrochemical energy storage for green grid. Chemical Reviews, 111(5):3577–3613, 2011.

[214] R. Yazami. Surface chemistry and lithium storage capability of the graphite-lithium electrode. Electrochimica Acta, 45(1-2):87–97, 1999.

[215] Y. Ye, C. C. Ahn, C. Witham, B. Fultz, J. Liu, A. G. Rinzler, D. Colbert, K. A. Smith, and R. E. Smalley. Hydrogen adsorption and cohesive energy of single-walled carbon nanotubes. Applied Physics Letters, 74(16):2307–2309, 1999.

[216] B. Yoon, D. Seghete, A. S. Cavanagh, and S. M. George. Molecular layer deposition of hybrid organic-inorganic alucone polymer films using a three-step ABC reaction sequence. Chemistry of Materials, 21(22):5365–5374, 2009.

[217] M. Yoshio, H. Y. Wang, and K. Fukuda. Spherical carbon-coated natural graphite as a lithium-ion battery-anode material. Angewandte Chemie-International Edition, 42(35):4203–4206, 2003.

[218] M. Yoshio, H. Y. Wang, K. Fukuda, Y. Hara, and Y. Adachi. Effect of carbon coating on electrochemical performance of treated natural graphite as lithium-ion battery anode material. Journal of the Electrochemical Society, 147(4):1245–1250, 2000.

[219] A. Zaban, E. Zinigrad, and D. Aurbach. Impedance spectroscopy of Li electrodes. 4. A general simple model of the Li-solution interphase in polar aprotic systems. Journal of Physical Chemistry, 100(8):3089–3101, 1996.

[220] H. L. Zhang, F. Li, C. Liu, J. Tan, and H. M. Cheng. New insight into the solid electrolyte interphase with use of a focused ion beam. Journal of Physical Chemistry B, 109(47):22205–22211, 2005.

[221] J. Zhang, Y. J. Xiang, Y. Yu, S. Xie, G. S. Jiang, and C. H. Chen. Electrochemical evaluation and modification of commercial lithium cobalt oxide powders. Journal of Power Sources, 132(1-2):187–194, 2004.

[222] W. Zhang, S. H. Brongersma, O. Richard, B. Brijs, R. Palmans, L. Froyen, and K. Maex. Influence of the electron mean free path on the resistivity of thin metal films. Microelectronic Engineering, 76:146, 2004.

[223] W. J. Zhang. Structure and performance of $LiFePO_4$ cathode materials: A review. Journal of Power Sources, 196(6):2962–2970, 2011.

[224] Y. Zhang, C. S. Sun, and Z. Zhou. Sol-gel preparation and electrochemical performances of $LiFe_{1/3}Mn_{1/3}Co_{1/3}PO_4/C$ composites with core-shell nanostructure. Electrochemistry Communications, 11(6):1183–1186, 2009.

[225] Z. R. Zhang, H. S. Liu, Z. L. Gong, and Y. Yang. Comparison of electrochemical and surface properties of bare and TiO_2-coated $LiNi_{0.8}Co_{0.2}O_2$ electrodes. Journal of the Electrochemical Society, 151(4):A599–A603, 2004.

[226] Z. R. Zhang, H. S. Liu, Z. L. Gong, and Y. Yang. Electrochemical performance and spectroscopic characterization of TiO_2-coated $LiNi_{0.8}Co_{0.2}O_2$ cathode materials. Journal of Power Sources, 129(1):101–106, 2004.

[227] H. L. Zhao, G. Ling, W. H. Qiu, and X. H. Zhang. Improvement of electrochemical stability of $LiCoO_2$ cathode by a nano-crystalline coating. Journal of Power Sources, 132(1-2):195–200, 2004.

[228] J. M. Zheng, Z. R. Zhang, X. B. Wu, Z. X. Dong, Z. Zhu, and Y. Yang. The effects of AlF_3 coating on the performance of $Li[Li_{0.2}Mn_{0.54}Ni_{0.13}Co_{0.13}]O_2$ positive electrode material for lithium-ion battery. Journal of the Electrochemical Society, 155(10):A775–A782, 2008.

[229] Z. B. Zhou, M. Takeda, T. Fujii, and M. Ue. $Li[C_2F_5BF_3]$ as an electrolyte salt for 4 V class lithium-ion cells. Journal of the Electrochemical Society, 152(2):A351–A356, 2005.